University of Nottingham

Doctoral Thesis

Towards Quantum Optics Experiments with trapped atoms in a Hollow-Core Fibre

Author:

Sindhu Jammi

Supervisor:

Dr. Thomas Fernholz

A thesis submitted in fulfillment of the requirements

for the degree of Doctor of Philosophy

to the

School of Physics and Astronomy



September 2017

Abstract

Doctor of Philosophy

Towards Quantum Optics Experiments with trapped atoms in a Hollow-Core Fibre

by Sindhu Jammi

A proposal for performing quantum memory schemes with a light matter interface in Hollow Core Fibres is introduced. Various technical aspects of implementing such a scheme in the proposed interface are outlined and the different elements required to realize this scheme are discussed, primarily the detection of atomic levels and the extension of the scheme to magnetically trappable levels. A new method to dispersively measure populations and population difference of alkali atoms prepared in their two clock states is introduced, for future use in the Hollow Core Fibre interface. The method essentially detects the atom numbers based on the influence of the linear birefringence in the ensemble on the detection light beams via polarization homodyning. Sideband detection is performed after dressing the atoms with a radio-frequency field to circumvent low-frequency technical noises. The noise performance of this scheme is discussed along with design modifications aimed at reaching the atomic shot noise limit. Another technical aspect of realizing the quantum memory scheme in the proposed light-matter interface is the extension of the scheme to the trappable states of the atomic system as the atoms will be trapped in an atom chip magnetic field. We achieve this extension by showing the microwave spectroscopy of the ground state ensemble of radio-frequency dressed atoms which proves the existence of pseudo one-photon transitions between the trappable clock states. Finally, the preliminary designs and results of integrating an HCF in an atom chip experiment are discussed.

Acknowledgements

My four years at the University of Nottingham have been a very educational and inspirational experience for me, not least due to the supervision of Dr. Thomas Fernholz. I would like to thank him for always having the time to answer questions big or small and for showing us the attention to detail necessary in all aspects of research.

I thank all the people in the Cold Atoms group at Nottingham and the Marie Curie ITN QTea Project for teaching and learning along with me, for the various discussions during lunch and the fun gatherings over the course of these years. Their friendship made these years an enjoyable experience.

I thank my friends from undergraduate studies (especially The Herd$^{\text{TM}}$) for being constant sources of brilliance and quirkiness, for all the times spent together and for always cheering me up. Sharing the undergrad and postgrad journeys with them has been a huge pleasure.

I thank my parents and family for always supporting me, always encouraging me and always believing in me. Their hardwork, dedication, perseverance and ethics are qualities I try to emulate everyday.

Contents

Abstract i

Acknowledgements ii

Contents iii

List of Figures vi

List of Tables viii

Abbreviations ix

1 Introduction 1
- 1.1 Motivation . . . 1
- 1.2 Literature Review . . . 3
- 1.3 Outline . . . 8

I Detection of Atomic Clock States 9

2 Quantum Description of Atoms and Light 11
- 2.1 Atomic Spin . . . 12
- 2.2 Polarized Light - Stokes Operator Description . . . 15
- 2.3 Atom-Light Interaction . . . 19
  - 2.3.1 Atom-Light Interaction in the continuous Dipole Approximation . . . 19

3 Dispersive Detection of Linear Birefringent atoms 22
- 3.1 Linear Birefringence . . . 23
  - 3.1.1 Interaction Hamiltonian . . . 24
  - 3.1.2 Detection of atomic linear birefringence with Stokes operator $\hat{S}_z$ . . . 28
- 3.2 The cold atoms experimental setup . . . 31
  - 3.2.1 Set-up of Lasers and magnetic fields . . . 31
  - 3.2.2 MOT system . . . 37

3.3 State Preparation of ^{87}Rb atoms in their clock states . . . 39
3.3.1 Optical Pumping . . . 41
3.3.2 Efficiency of the state preparation process . . . 42
3.4 Experimental detection of ^{87}Rb clock states . . . 43
3.4.1 Detection System . . . 43
3.4.2 Two State Detection . . . 45
3.5 Detection of atomic polarizability and decay coefficients . . . 47
3.6 Detection of Rabi Cycles . . . 50

4 Radio-frequency Dressed Detection of Atomic Clock States 53
4.1 Modulation of signals by dressing atoms . . . 54
4.1.1 Adiabatic Radio-frequency Dressing . . . 55
4.1.2 Dressed linear birefringence . . . 58
4.2 Experimental setup . . . 61
4.2.1 RF Dressed Detection Scheme . . . 61
4.2.2 Experimental Sequence of RF Dressed Detection . . . 63
4.3 Experimental signals from dressed states . . . 66
4.3.1 Sideband detection . . . 66
4.3.2 Two State Dressed Detection . . . 67
4.3.3 Signal strength with Field Detuning . . . 69
4.4 Rabi Cycles with RF dressed detection . . . 73
4.5 State to Quadrature Mapping . . . 75

5 Noise Analysis 77
5.1 Standard Quantum Limit . . . 77
5.2 Performance of the system . . . 80
5.3 Analysis of noise sources . . . 83
5.3.1 State Preparation noise . . . 83
5.3.2 Light Noise . . . 85
5.3.3 50 Hz Noise and Influence of other external noise . . . 87
5.4 Noise Reduction with detection at different fields . . . 89
5.4.1 Dependence of state transfer probability with static field . . . 89
5.4.2 Detection of two states with static field shift . . . 90
5.5 Outlook - Towards detection of atoms at the quantum limit . . . 92
5.5.1 Simultaneous Detection of the two clock states . . . 92
5.5.2 Reduction of detection noise with a low-finesse cavity . . . 94

II Radio-Frequency Dressed Microwave Spectroscopy 95

6 Radio-frequency Dressed Microwave Spectroscopy 97
6.1 RF Dressing of the ground state ensemble . . . 98
6.2 Microwave Interaction . . . 101
6.3 Experimental Sequence . . . 106
6.4 Orthogonal and Parallel Settings . . . 108

6.5 Dressed Transitions from individual sub-levels at ω_{RF} detuning . . . 110
6.5.1 Preparation of individual sub-levels . . . 110
6.5.2 Data of the dressed transitions . . . 111

7 Characterization of the Dressed Clock Transitions 114
7.1 The clock transitions . . . 115
7.2 Dependence on static field magnitude . . . 117
7.2.1 Dependence of the clock transitions on the static field . . . 117
7.3 Dressed transition strengths . . . 120

III Hollow-Core Fibre based light matter interface 123

8 Hollow-Core Fibre based light matter interface 125
8.1 Introduction . . . 125
8.2 Setup Designs . . . 127
8.2.1 Fibres on Chip . . . 127
8.2.2 Vacuum Feedthrough . . . 133

9 Conclusions 135

A The Off-resonant limit 137

B Calculations for Interaction Hamiltonian 139
B.1 Calculating $C^{\pm}(\Delta, m)$ . . . 139
B.2 Calculating $b(\Delta, m)$ . . . 143

Bibliography 145

List of Figures

2.1 Light Polarization 16

3.1 Linear Birefringence 23
3.2 Interaction Hamiltonian terms 25
3.3 Lasers in experiment 32
3.4 The optical transitions in the experiment 33
3.5 Laser Locking Schematics 34
3.6 Laser Locking and Detuning Scheme for the Detection Lasers 36
3.7 The setup for required magnetic fields in the experiment 37
3.8 The MOT set-up 38
3.9 State Preparation process 40
3.10 Optical Pumping 41
3.11 Efficiency of the State Cleaning Process 42
3.12 Schematic of Detection System 43
3.13 Sample Dispersive Image of atoms in F=1 44
3.14 Two State Detection Sequence 46
3.15 Linear Birefringence with detuning 48
3.16 Rabi cycles of the clock states 50
3.17 State Transfer Probability 51

4.1 RF Coupling of hyperfine levels 54
4.2 RF Dressed Detection Scheme 61
4.3 Mode Matching Detection Beams 62
4.4 Experimental Sequence of RF Dressed Detection 64
4.5 Sideband Detection 66
4.6 RF signals in the orthogonal setting 67
4.7 Typical Experimental signals for dressed detection 68
4.8 Dependence of Signal Strength with Static field detuning 70
4.9 Experimental data showing signal strength with $\mathbf{B}_{\text{eff}}$ 71
4.10 Dressed Detection of Rabi Cycles 73
4.11 Dependence of signal phases on Light Polarization Angle 75

5.1 Projection Noise for CSS and SSS 78
5.2 Variance of state transfer probability 80
5.3 Noise Performance 81
5.4 State preparation noise 84

5.5 Calibration of Detector with Light Noise 86
5.6 Noise with static field 87
5.7 Noise Performance at static field resonance and insensitive points . . 90
5.8 Noise Performance with field shift 91
5.9 Simultaneous measurement of two states 93

6.1 Energy levels splitting with RF field 100
6.2 Bare and RF Dressed Transitions 102
6.3 RF Dressed MW spectra 104
6.4 RF Dressed MW Spectra Sequence 106
6.5 Orthogonal and Parallel Setting Spectra 108
6.6 Dressed Transitions at ω_{RF} detuning 112

7.1 The Dressed Clock transitions 115
7.2 Dependence of dressed transition frequencies on static field 118
7.3 Rabi Cycles of Clock Triplet 120
7.4 Clock Triplet Transition Strengths 121

8.1 Light Matter Interface with a Hollow Core Fibre 126
8.2 Integration of HCF into an atom chip experiment 127
8.3 Plot of design for UV mask and structures fabricated 128
8.4 Modified Structure Edges for holding the fibres 129
8.5 Modified Support Structures for compatibility to fibre diameters . . 130
8.6 Coupling of two fibres on a chip 131
8.7 Vacuum Feedthrough tests 133

List of Tables

3.1 The S_2 moments of different hyperfine levels 30

B.1 *Polarizability for F=1* 141
B.2 *Polarizability for F=2* 142

Abbreviations

AOM	Acousto Optic Modulator
CSS	Coherent Spin State
EOM	Electro Optic Modulator
FWHM	Full Width Half Maxima
GRIN	Gradient Index
HCF	Hollow-Core Fibre
LIAD	Light Induced Atomic Desorption
MOT	Magneto-Optical Trap
MW	Microwave
PCB	Printed Circcuit Board
QND	Quantum Non Demolition
QPN	Quantum Pojection Noise
RF	Radio-Frequency
SSS	Spin Squeezed State
UHV	Ultra High Vacuum
UV	Ultra-Violet

Chapter 1

Introduction

The subject of this thesis is to assemble some of the elements required for a proposed light-matter interface of magnetically trapped atoms in a Hollow-Core Fibre. It introduces a new technique for the detection of atomic clock state populations by measuring the linear birefringence of Radio-Frequency dressed atomic states, which enables low noise population detection. It then shows the possibility of Microwave spectroscopy in these Radio-Frequency dressed states. These discussions are to motivate the realization of quantum memory or atomic clock experiments in the proposed light-matter interface as given in Section 1.1. The thesis relies primarily on experimental data.

Section 1.2 gives a review of the current literature leading towards the outline of the scheme discussed in Section 1.1. It provides an overview of the Quantum memory and quantum communication fields and also includes discussions on the different light-atom interfaces achieved and atom chip trapping schemes. Section 1.3 provides an outline of this thesis and a guide to the chapters included.

1.1 Motivation

This section motivates the idea of a quantum memory scheme in a Hollow-Core Fibre based light-matter interface. The emulation of successful quantum memory

schemes in various atomic systems like room-temperature vapour cells [1] with an ultra-cold atoms setup would give the added advantages of longer measurement lifetimes and reduced collisional effects among the atoms and with fibre walls.

However, the design of such schemes must take into consideration experimental characteristics of cold atom systems for them to be successful. For example, the interaction strength between the light and atoms required for such experiments - achieved in vapour cells with a high atom number - will not be of the same order in cold atom systems as the atom number in these systems is typically $4-6$ orders of magnitude lower. The light matter interface has to achieve the increase in the coupling strength between light and atoms in another way, for example by reducing the area of interaction which results in an increase of the interaction strength linearly. This effect has been exploited to use Hollow-Core Fibre based light-atom interfaces with a typical area of $10-100$ μm^2 [2] [3] [4].

Different techniques to load atoms into the fibre are possible. Among these, passive techniques like diffusion of atoms into the fibre in vacuum [4] and actively loading atoms with a dipole trap [2] [3] have been demonstrated. The number of atoms in the fibre for repeated measurements can be controlled by Light Induced Atomic Desorption (LIAD) and dipole trap depth respectively. However, the area of the core - for successful diffusion to place, or for the fibre to allow transmission of the two regimes of optical frequencies required for the dipole trap and interaction with atoms - is usually on the higher end of the current hollow core fibres. Loading atoms into a Hollow core Photonic Crystal Fibre with an atom chip to trap and guide the atoms is proposed to allow integration of a fibre with typical area 10 μm^2 into the scheme. The number of atoms and position of the ensemble in the fibre can be tightly controlled by magnetic fields from an atoms chip.

The use of magnetically trapped alkali atoms in the system requires the extension of the scheme from the clock states to trappable levels in the atomic systems. The use of dressed atomic states to facilitate this aspect of the scheme is discussed. A detection scheme is introduced taking into consideration the technical aspects of

the scheme like the magnetic fields, to allow for sideband detection of the atomic levels.

1.2 Literature Review

The advent of technology facilitating experiments that are able to show quantum mechanical effects has opened a door to a range of studies from proving fundamental effects to coming full circle and facilitating new or improved technology for precision measurements. The experiments with laser cooled atoms [5], [6], [7] and ions [8], [9], with very high controllability as well as extreme physical parameter regimes, are examples of such ground-breaking research. Over the last few decades, these versatile systems have been used to study condensed matter systems [10]; in precision measurements [11], [12] and to build quantum communication and quantum information systems [13].

Quantum Memories

Quantum Communication, i.e. the transport of unknown quantum states is a lucrative field aiming for the secure exchange of information between two places. To account for optical losses over large distances, quantum networks [14] with repeater nodes have been proposed. This requires the storage and retrieval of quantum information at each node, which can be defined as a quantum memory. The transfer of information at each node can be defined as Quantum Teleportation [15] of states. Quantum memories can also be expressed as an entanglement between two quantum systems. Realizing efficient and long-lived Quantum Memories [16] [17], is the stepping stone to establishing quantum communication among nodes in a network [18] [14]. The nodes in a quantum network can also be used for large scale or distributed quantum computation [19] [20]. Quantum Communication between two atomic ensembles has also been demonstrated [21] [22].

Quantum memories for light have been successfully realized with atomic ensembles [23] [24] [1], solid state systems [25] [26] and single atoms [17]. The parameters important for a functional quantum network or distributed quantum computation are the retrieval efficiency and lifetime of quantum memories. These experiments need a high interaction strength between light and atoms, achieved by high atom numbers in vapour cells [1] [27] and solid state systems; increased interaction with the implementation of high finesse cavities [28]; and using a small area of interaction as in a hollow core fibre [4]. Controlling the atoms using magnetic traps can reduce collisional effects between the atoms and fibre walls.

Detection Methods

Schemes such as those described above require detection of the atomic quantum state at the quantum noise limit. Analyzing the atomic state by detecting the two states which are in a superposition would increase the measurement sensitivity. This also has the added advantage of use in atom interferometric systems that needs detection of atom number difference in two hyperfine states. This can be achieved by either detecting atoms in both the states individually and taking their difference later or directly detecting subtracted signals from the two states near zero difference. The precision of these measurements, dependent on $\Delta N/N$ where ΔN is the atom number difference and N is the total atom number, is usually limited by the Heisenberg Uncertainty Relation. This limit on the uncertainty in measurement of ΔN, commonly called the Quantum Projection Noise limit (QPN), is a fundamental barrier of measurement inherent in two state detection [29]. Currently, measurements based on fluorescence imaging [30] are used to detect small numbers of atoms at the single atom limit [31] or state selectively measure large ensembles with atom shot noise limited performance [32].

It is possible to improve the measurement sensitivity and go beyond the QPN limit by using spin squeezed atoms [33] as inputs for the schemes. Spin squeezing is essentially defined as redistributing quantum fluctuations between two non-commuting atomic spin components while still preserving the uncertainty limit

such that one observable can go beyond the standard quantum limit. It is first established by Kitagawa and Ueda in 1993 [34] and is analogous to photon squeezing [35]. Experimental realizations of spin squeezed atoms have been achieved by various methods since then, for example – one-axis twisting [36], two-axis counter twisting [37], transfer of squeezing from light to atoms [38] and non demolition measurements of one state [39]. Spin squeezing inequalities have also been shown to detect entanglement [40] in two qubit systems [41].

The methods of detecting atoms mentioned previously like fluorescence imaging and state selective measurements are not capable of generating spin squeezed atoms due to the nature of information obtained. Dispersive non demolition methods however allow the information gathered to be used in a feedback loop [42] to achieve conditional spin squeezing. These Quantum Non-Demolition techniques direct the backaction noise that arises out of measuring a variable in a quantum system to the conjugate variable. An experimental demonstration of 18 dB of conditional spin squeezing and projective measurements with real time feedback have been shown [42] and 20 dB of unconditional spin-squeezing has been achieved in an optical cavity [43].

Atom Interferometers

Atom interferometers in particular, have been used for precision measurements in various areas [44] since the first proposals by Altshuler and Frantz in 1973 [45] [46]. The phase shift garnered in interferometry experiments is directly proportional to the energy of the particles used. The ratio of phase shift in matterwave interferometers using atoms of mass m and light interferometers with light frequency ω is equal to $mc^2/\hbar\omega$. Thus, the phase shift in atom interferometer experiments is orders of magnitude larger than that in optical interferometer experiments when accumulated over the same effective interferometer area, motivating the development of this field. The first atom interferometers with two spatial trajectories were realized in four different experiments in 1991 – as a Mach Zehnder interferometer [47], a two-photon Raman transition [48], a Young's double slit experiment [49]

and a Sagnac effect measurement [50]. Successful demonstrations of inertial measurements (proposed by Clauser in 1988 [51]) [52] [53], [54] and general relativity [55]; gravity gradiometry [56]; gravity accelerometers [57]; atomic clocks [58] [59]; rotation sensing [60]; precision measurement of fine structure constant α [61] [62]; have increased the interest in atom interferometry exponentially.

Commercial ventures operating on this principle to develop inertial measurement devices for rotation sensing required in navigation or geophysical tectonic plate rotation; gravity gradiometry accelerometers (μquans [63], AOSense [64]) and Atomic clocks [63] providing a reference for time metrology applications have fuelled efforts in making these devices not only more precise but also more portable. One of the advantages of these systems over current technology like GPS is that they don't depend on external satellite signals.

Trapping and Manipulation of atoms

The manipulation of neutral atoms with magnetic fields has first been achieved in 1985 [65] by using the interaction between an inhomogeneous magnetic field and induced dipole moment in the atoms, followed by extensive studies into possible trap geometries. Proposing and realizing atom chips [66] - nanofabricated charged [67] and current carrying structures [68] has been a technological leap in this field. The control and versatility of atom chips as trapping and guiding structures for atoms prompted their use in proposals and realizations of schemes in various fields like atom interferometry [69] [70] and quantum optics [71] [72].

Radio frequency dressing potentials have proven to be a versatile and robust modulating technique for atoms to achieve various results [73]. The coupling induced between the radio frequency field and the electronic ground states of neutral atoms is magnetic and vector in nature which allows design of state dependent potentials. In the last few years, experiments have demonstrated the control and flexibility required for atomic potentials in matterwave schemes [74] [75] [76]. Experiments

conducted recently have realized RF dressed atom traps [75] [77] and evaporative cooling of atoms with RF fields in adiabatic traps [78] [79] [80], increasing the popularity of RF fields recently. In particular, ring traps for atoms with RF dressing fields [81] [82] have been successfully realized in multiple experiments [83–85] which allows guided atom interferometry [86]. These schemes have the expected advantage of increased sensitivity due to smaller interferometry areas over schemes with freely falling atoms. The experimental systems built with these schemes can also be more compact and robust compared to free space propagation devices which allows portability of the new generation of atom interferometers. As manipulation of atoms with adiabatic potentials develops, so too should detection methods that can be easily incorporated into those schemes. Detection methods that are versatile enough to be incorporated into various schemes, yet show competitive performance for higher optical densities than shown with fluorescence imaging would greatly increase commercialization of atom interferometer devices.

1.3 Outline

This thesis is divided into three parts, namely

- Detection of atomic clock states
- Radio-Frequency Dressed Microwave Spectroscopy
- Hollow-Core Fibre based light matter interface

The four chapters in Part I introduce our new method of RF dressed detection. Chapter 2 gives the quantum mechanical description of light and atoms used along with the general effective interaction Hamiltonian of the system. Chapter 3 introduces the dispersive detection of the atomic clock states using the linear birefringence of the atoms. It provides the theoretical framework for the effective interaction Hamiltonian of ^{87}Rb atoms and discusses the figure of merit for this detection scheme. It also includes sections describing the cold atoms setup used, the design and sequence of the detection scheme and the results achieved. Chapter 4 introduces RF dressed detection of the atomic clock states. It builds on the linear birefringence detection scheme described in Chapter 3 to achieve sideband detection of these signals after adiabatically dressing the atoms with an RF field. It provides sections on the theory of the adiabatic dressing and detection, the experimental sequence and setup used as well as the considerations required to implement this scheme. Chapter 5 determines the noise performance of this scheme in our experiment and gives different methods to improve it.

Part II proves the possibility of RF dressed microwave spectroscopy. Chapter 6 describes the occurrence of microwave transitions in dressed atoms and discusses the experimental configurations possible. Chapter 7 characterizes three of the dressed transitions seen to determine dependence on various experimental parameters.

Chapter 8 in Part III introduces the proposal of a new light matter interface planned by integrating a hollow core fibre in an atom chip based cold atom experiment. The design of the system and the preliminary results achieved are discussed here.

Part I

Detection of Atomic Clock States

Summary

This part introduces a new method to dispersively measure population and population difference of alkali atoms prepared in their two clock states ($m = 0$). Linear birefringence of the atomic medium allows atom number detection via polarisation homodyning, i.e. common path interferometry. In order to achieve low technical noise levels, we perform sideband detection after adiabatically transforming the atomic states via radio-frequency dressing. The balanced homodyne signal then oscillates independently of field fluctuations at twice the dressing frequency, thus allowing for robust, phase-locked detection that circumvents low-frequency noise. Using probe pulses of two optical frequencies, we can detect both atomic states simultaneously and obtain population difference as well as total atom number. Atomic state to light quadrature mapping is demonstrated. The method extends to other Zeeman sublevels and can thus be used in a range of atomic clock schemes and atom interferometric measurements.

Chapter 2

Quantum Description of Atoms and Light

This chapter lays the framework for working with atoms and light described as quantum systems. Generally, atoms are experimentally easier to keep and thus are better used for storing quantum states in the context of quantum memories and quantum information. Light (laser beams) is better suited to transport or measure the quantum information as it can hold its spatial and temporal coherence over longer distances. As a whole, an interacting system of light and atoms can therefore be used in various experiments involving the measurement of properties that lead to the study of topics ranging from quantum tomography to quantum information and quantum communication.

One of the possible ways to describe the light-atom interaction is by using the spin operators as quantum variables for the atomic state (discussed in Section 2.1) and Stokes operators (discussed in Section 2.2) for the light polarization respectively. The light-atom interaction is discussed in terms of the effect of atomic spin on light polarization to formulate a basis for a Quantum Non Demolition measurement. This kind of measurement, wherein gaining knowledge of the atomic spin state is possible without destroying the atomic state, is possible when the light used is in

the off-resonant regime of an atomic transition. The required effective interaction Hamiltonian is discussed in Section 2.3.

2.1 Atomic Spin

This section describes the atomic state in terms of its angular momentum [87] and then discusses the states of ^{87}Rb atoms in particular that will be used in the experiments given in this thesis. The ground states of Rubidium are characterized by the outermost electron in the $5S_{1/2}$ state, for which the orbital angular momentum **L** is zero. The fine structure occurs due to the coupling between the orbital angular momentum **L** of the outer electron and its spin angular momentum **S**, with the total electron angular momentum given by $\mathbf{J} = \mathbf{L} + \mathbf{S}$. For the ^{87}Rb ground state, L = 0 and S = 1/2, so J = 1/2. The hyperfine structure, a result of the coupling between the total electron angular momentum **J** and the total nuclear angular momentum **I** can be described by the total atomic angular momentum **F** given by $\mathbf{F} = \mathbf{J} + \mathbf{I}$. For the ^{87}Rb ground state, J = 1/2 and I = 3/2, so F = 1 or F = 2 with the magnetic quantum numbers m_F defining the Zeeman levels of the ground states.

We use the clock states of the ^{87}Rb atoms, i.e. the $|F, m_F\rangle : |1, 0\rangle$ and the $|F, m_F\rangle : |2, 0\rangle$ states in our experiments. The notations $|\uparrow\rangle = |2, 0\rangle$ and $|\downarrow\rangle = |1, 0\rangle$ are introduced for these two states thereby simplifying the description of the atom to an effective two level system.

We assume the ensemble of atoms in the experiments to be composed of these simplified two-level atomic systems. Thus, the ensemble can be described by a collective spin state $\hat{F}$ comprising the quasi spin-1/2 atoms as given below.

$$\hat{F} = \frac{\hbar}{2} \sum_{j=1}^{N_A} \begin{pmatrix} \hat{\sigma}_{x,j} \\ \hat{\sigma}_{y,j} \\ \hat{\sigma}_{z,j} \end{pmatrix}. \tag{2.1}$$

where the atom number in the ensemble N_A is of the order 10^8 in our system and the Pauli matrices $\hat{\sigma}_x, \hat{\sigma}_y$ and $\hat{\sigma}_z$ in this $\{|\uparrow\rangle, |\downarrow\rangle\}$-basis are given by

$$\begin{aligned} \hat{\sigma}_x &= |\downarrow\rangle\langle\uparrow| + |\uparrow\rangle\langle\downarrow|, \\ \hat{\sigma}_y &= i\,|\downarrow\rangle\langle\uparrow| - i\,|\uparrow\rangle\langle\downarrow|, \\ \hat{\sigma}_z &= |\uparrow\rangle\langle\uparrow| - |\downarrow\rangle\langle\downarrow|, \end{aligned} \tag{2.2}$$

These operators can be represented in matrix form using the basis $|\uparrow\rangle = \begin{pmatrix} 1 \\ 0 \end{pmatrix}$ and $|\downarrow\rangle = \begin{pmatrix} 0 \\ 1 \end{pmatrix}$ and are given by

$$\hat{\sigma_x} = \begin{pmatrix} 0 & 1 \\ 1 & 0 \end{pmatrix}, \quad \hat{\sigma_y} = \begin{pmatrix} 0 & -i \\ i & 0 \end{pmatrix}, \quad \hat{\sigma_z} = \begin{pmatrix} 1 & 0 \\ 0 & -1 \end{pmatrix}, \tag{2.3}$$

The variables $\hat{F}_x$, $\hat{F}_y$ and $\hat{F}_z$ defined in Equation 2.1 follow the commutation relation

$$\left[\hat{F}_x, \hat{F}_y\right] = i\hbar\hat{F}_z \tag{2.4}$$

This results in the quantum fluctuations in these spin components being bound by the Heisenberg Uncertainty Relation

$$\left\langle(\Delta\hat{F}_y)^2\right\rangle \left\langle(\Delta\hat{F}_z)^2\right\rangle \geq \frac{\hbar^2 \left\langle\hat{F}_x\right\rangle^2}{4}. \tag{2.5}$$

which sets a limit on the measurement of these variables.

In the following, we discuss the specific case where each atom is prepared in a coherent superposition of the two states $|\uparrow\rangle$ and $|\downarrow\rangle$, to look at the uncertainties of the spin components. The atoms are all polarized in what we define as the x-axis with a static magnetic field in that direction. This is defined as the coherent spin state given by

$$|\Psi\rangle = \left[\frac{|\uparrow\rangle + |\downarrow\rangle}{\sqrt{2}}\right]^{\otimes N_A}, \tag{2.6}$$

Coherent Spin States are characterized by minimum uncertainties in the measurement of the spin variables. The spin expectation values are derived as

$$\begin{aligned}\left\langle \hat{F}_x \right\rangle &= \frac{\hbar}{2} \sum_{j=1}^{N_A} \langle \Psi | \hat{\sigma}_{x,j} | \Psi \rangle = \frac{\hbar}{2} N_A, \\ \left\langle \hat{F}_y \right\rangle &= \left\langle \hat{F}_z \right\rangle = 0,\end{aligned} \tag{2.7}$$

The uncertainties of the three spin components are derived as the variances

$$\begin{aligned}\left\langle (\Delta \hat{F}_x)^2 \right\rangle &= \frac{\hbar^2}{4} \sum_{j,k=1}^{N_A} \langle \Psi | \hat{\sigma}_{x,j} \hat{\sigma}_{x,k} | \Psi \rangle - \left\langle \hat{F}_x \right\rangle^2 = 0, \\ \left\langle (\Delta \hat{F}_y)^2 \right\rangle &= \left\langle (\Delta \hat{F}_z)^2 \right\rangle = \frac{\hbar^2}{4} N_A.\end{aligned} \tag{2.8}$$

We define new variables as atomic quadratures with the Holstein-Primakoff transformation [88] and approximation for large F (i.e. a large number of atoms N_A)

$$\hat{x}_A = \frac{\hat{F}_y}{\sqrt{\hbar \left\langle \hat{F}_x \right\rangle}}, \qquad \hat{p}_A = \frac{\hat{F}_z}{\sqrt{\hbar \left\langle \hat{F}_x \right\rangle}}, \tag{2.9}$$

These variables follow the commutation relation $[\hat{x}_A, \hat{p}_A] = i\hat{F}_x / \left\langle \hat{F}_x \right\rangle \approx i$, the approximation treating $\left\langle \hat{F}_x \right\rangle$ as the classical $\hat{F}_x$ is made due to the large number of atoms N_A.

Correspondingly, the variances for these variables are given as

$$\left\langle (\Delta \hat{x}_A)^2 \right\rangle = \left\langle (\Delta \hat{p}_A)^2 \right\rangle = \frac{1}{2}. \tag{2.10}$$

2.2 Polarized Light - Stokes Operator Description

Dispersive detection of atoms involves analyzing the effect of an ensemble of atoms in a particular spin state on polarized light. The Stokes operators are used to describe the polarized states of light and the propagation equations of these states in a medium can be used to describe its interaction with atoms.

The Stokes operators require a definition of a coordinate system and are defined for light that is polarized in the x, y-plane, i.e. propagating along $\pm z$.

Starting from creation and annihilation operators for photons of horizontal (H, along x) and vertical (V, along y) polarizations, the operators for $\pm 45°$ and circular polarizations, corresponding to $\sigma^{+,-}$ are

$$\begin{aligned} \hat{a}_{\nearrow} &= \left(\hat{a}_H + \hat{a}_V\right)/\sqrt{2}, \\ \hat{a}_{\nwarrow} &= \left(-\hat{a}_H + \hat{a}_V\right)/\sqrt{2}, \\ \hat{a}_{+} &= \left(\hat{a}_H - i\hat{a}_V\right)/\sqrt{2}, \\ \hat{a}_{-} &= \left(\hat{a}_H + i\hat{a}_V^{\dagger}\right)/\sqrt{2}. \end{aligned} \tag{2.11}$$

The definitions for circular polarizations are such that σ^+ photons carry a positive z component of angular momentum.

The Stokes operators describes the collective photon spin and can be compared to Pauli operators. They are given by

$$\hat{S} = \begin{pmatrix} \hat{S}_x \\ \hat{S}_y \\ \hat{S}_z \end{pmatrix} = \frac{\hbar}{2} \begin{pmatrix} \hat{\sigma}_x \\ \hat{\sigma}_y \\ \hat{\sigma}_z \end{pmatrix}, \tag{2.12}$$

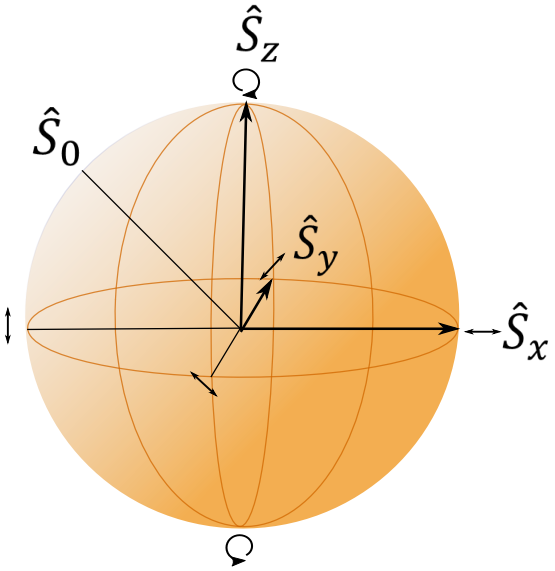


FIGURE 2.1: Poincaŕe Sphere showing the different light polarizations

with $\hat{\sigma}_x, \hat{\sigma}_y$ and $\hat{\sigma}_z$ defined [89] as

$$\begin{aligned}
\hat{\sigma}_y &= \hat{a}^\dagger_{\swarrow}\hat{a}_{\nearrow} - \hat{a}^\dagger_{\searrow}\hat{a}_{\nwarrow} = +i\hat{a}^\dagger_{-}\hat{a}_{+} - i\hat{a}^\dagger_{+}\hat{a}_{-} = \hat{a}^\dagger_{V}\hat{a}_{H} + \hat{a}^\dagger_{H}\hat{a}_{V}, \\
\hat{\sigma}_z &= -i\hat{a}^\dagger_{\nwarrow}\hat{a}_{\nearrow} + i\hat{a}^\dagger_{\swarrow}\hat{a}_{\searrow} = \hat{a}^\dagger_{+}\hat{a}_{+} - \hat{a}^\dagger_{-}\hat{a}_{-} = +i\hat{a}^\dagger_{V}\hat{a}_{H} - i\hat{a}^\dagger_{H}\hat{a}_{V}, \\
\hat{\sigma}_x &= \hat{a}^\dagger_{\nwarrow}\hat{a}_{\nearrow} + \hat{a}^\dagger_{\swarrow}\hat{a}_{\searrow} = \hat{a}^\dagger_{-}\hat{a}_{+} + \hat{a}^\dagger_{+}\hat{a}_{-} = \hat{a}^\dagger_{H}\hat{a}_{H} - \hat{a}^\dagger_{V}\hat{a}_{V}.
\end{aligned} \tag{2.13}$$

The different polarizations can be represented on a Poincaré sphere as shown in Figure 2.1. The operator $\hat{S}_0$ defines the radius of the sphere and essentially describes the number of photons $\hat{N}_P$ in the light beam. It is a scalar operator given by $\hat{S}_0 = \hat{N}_P/2$. The vector Stokes components can be defined in terms of numbers of photons of different polarizations from Equation 2.13 as

$$\begin{aligned}
\hat{\sigma}_x &= \hat{n}_H - \hat{n}_V, \\
\hat{\sigma}_y &= \hat{n}_{\nearrow} - \hat{n}_{\nwarrow}, \\
\hat{\sigma}_z &= \hat{n}_+ - \hat{n}_-.
\end{aligned} \tag{2.14}$$

where $\hat{n}_H = \hat{a}^\dagger_H \hat{a}_H$ is the number of photons polarized in the H-direction, etc. It is

evident from these definitions that the Stokes operators essentially count photons in different directions. For example, we consider a situation where almost all the photons in the light beam are polarized such that the Stokes vector is in the y-direction. The Stokes vector components obey the commutation rules of angular momentum $\left[\hat{S}_x, \hat{S}_y\right] = i\hbar\hat{S}_z$ and cyclic permutations. The quantum fluctuations in the x and z directions follow the uncertainty relation

$$\left\langle (\Delta\hat{S}_z)^2 \right\rangle \left\langle (\Delta\hat{S}_x)^2 \right\rangle \geq \frac{\hbar^2 \left\langle \hat{S}_y \right\rangle^2}{4}. \tag{2.15}$$

As for atomic spin states, the equality in the above relation is the photon shot-noise limit of polarization measurement.

Using the frame of reference given above, the particular case of +45° polarized coherent light state can be discussed as most of the experiments described in this thesis use laser beams of input polarization +45°. In this situation, the state of N_P +45°-polarized photons is given by $|N_P\rangle = \left(\hat{a}^\dagger_{\nearrow}\right)^{N_P} |0\rangle$. The expectation values of the Stokes operators in this case can be derived as

$$\begin{aligned} \left\langle \hat{S}_y \right\rangle &= \frac{\hbar}{2} \langle N_P | \hat{n}_{\nearrow} - \hat{n}_{\searrow} | N_P \rangle = \frac{\hbar}{2} N_P, \\ \left\langle \hat{S}_x \right\rangle &= \left\langle \hat{S}_z \right\rangle = 0, \end{aligned} \tag{2.16}$$

The uncertainties or variances of the Stokes operators for this case can be calculated to be

$$\begin{aligned} \left\langle (\Delta\hat{S}_y)^2 \right\rangle &= 0, \\ \left\langle (\Delta\hat{S}_z)^2 \right\rangle &= \left\langle (\Delta\hat{S}_x)^2 \right\rangle = \frac{\hbar^2}{4} N_P. \end{aligned} \tag{2.17}$$

To complete the analogy between the atomic and photon spin operators, we scale Stokes operators equivalently to spin operators and define light quadratures similar

to standard position/ momentum operators as

$$\hat{x}_L = \frac{\hat{S}_z}{\sqrt{\hbar \left\langle \hat{S}_y \right\rangle}}, \qquad \hat{p}_L = \frac{\hat{S}_x}{\sqrt{\hbar \left\langle \hat{S}_y \right\rangle}}, \tag{2.18}$$

The similarity between the spin and light operators motivate atomic state to light quadrature mapping, or in other words, the exchange of quantum information between light and atoms. The light quadratures defined above follow the commutation relation $[\hat{x}_L, \hat{p}_L] = i\hat{S}_y / \left\langle \hat{S}_y \right\rangle \approx i$, where the approximation treating $\left\langle \hat{S}_y \right\rangle$ as the classical $\hat{S}_y$ is made due to the large number of photons N_P.

Correspondingly, the variances for these variables are given as

$$\left\langle (\Delta \hat{x}_L)^2 \right\rangle = \left\langle (\Delta \hat{p}_L)^2 \right\rangle = \frac{1}{2}. \tag{2.19}$$

The atomic spin and light polarization operators are described here as general individual systems. To discuss the effect of the collective atomic spin on the light polarization operators and vice versa, we need to first describe the interaction between them which can be done qualitatively with the interaction Hamiltonian.

2.3 Atom-Light Interaction

This section considers the interaction between light and atoms and derives an interaction Hamiltonian for the dispersive effects arising from the dynamical Stark shift of atomic energy levels in the presence of light fields. The absorption effects and spontaneous emissions are negligible when the probe beam is sufficiently far detuned from the atomic transition. It is to be noted that the two states considered in our experiment, i.e. the $|F, m\rangle : |1, 0\rangle$ and the $|F, m\rangle : |2, 0\rangle$ states of the ^{87}Rb electronic ground state hyperfine ensemble, are each probed with light fields of different optical frequencies in the $^2 5S_{1/2} \rightarrow^2 5P_{1/2}$ dipole transition. The technical details of the frequencies used and the transitions involved are discussed later in Section 3.2.1, here we only derive the effective interaction Hamiltonian in the off-resonant regime for a general ground and excited state.

The light-atom interaction in this regime has been actively studied [90] and been used for Quantum Non Demolition (QND) measurements [91] [92]. The calculations given in the Section 2.3.1 looking at the dipole approximation applied to the interaction and in Appendix A in the off-resonant regime follow from these studies with the latter section in particular from the treatment shown in [89] of the interaction Hamiltonian.

2.3.1 Atom-Light Interaction in the continuous Dipole Approximation

The dipole approximation treats the atom light interaction as an electric dipole in an electromagnetic field. The interaction Hamiltonian is given by $\hat{H}_{int} = -\hat{\mathbf{d}}.\hat{\mathbf{E}}$ where $\hat{\mathbf{d}}$ is the dipole operator of the atom and $\hat{\mathbf{E}}$ is the electromagnetic field vector. To observe this interaction in an experimental system, the interaction Hamiltonian $\hat{H}_{int}$ has to be of a certain strength. This is achieved in multiple ways, categorized into three cases: applying a large electromagnetic field, having a single particle with a large dipole moment or applying an electromagnetic field to an ensemble of atoms which behaves as a single large dipole operator $\hat{\mathbf{D}} = \sum \hat{\mathbf{d}}_i$.

Having a large ensemble of atoms is technically the easiest way to achieve the coupling strength required. The continuous description of light and matter is the simplest approach to describe the interaction Hamiltonian of the system. As the absorption effects and spontaneous emissions are negligible in the off-resonant regime, the interaction Hamiltonian has to describe the dispersive effects of atoms in light fields. This interaction can be used for QND measurements as dispersive measurements leave the atomic state for further experiments with an increase in knowledge of the state.

To write down the interaction Hamiltonian, we first assume that the ensemble of atoms has a cross-sectional area $A >> \lambda^2$ where λ is the wave length of the light. A one dimensional theory is used to describe the electric field per length as given below, with the propagation axis (z-axis) as quantization axis. The area relevant for the equation would then be the cross-sectional area A.

$$E' = \sqrt{\frac{\hbar\omega_0}{2\epsilon_0 A}}\left(\hat{a}_+(z,t)\mathbf{e}_{+1} + \hat{a}_+^\dagger(z,t)\mathbf{e}_{+1}^* + \hat{a}_-(z,t)\mathbf{e}_{-1} + \hat{a}_-^\dagger(z,t)\mathbf{e}_{-1}^*\right) \tag{2.20}$$

where ω_0 is the frequency of the transition between the ground and excited states; the unit vectors are given by $\mathbf{e}_{\pm1} = (\mathbf{e}_x \pm i\mathbf{e}_y)/\sqrt{2}$ and the circular creation and annihilation operators are given by $\hat{a}_+ = -(\hat{a}_x - i\hat{a}_y)/\sqrt{2}$ and $\hat{a}_- = (\hat{a}_x + i\hat{a}_y)/\sqrt{2}$.

The dipole operator of a single atom is written as $\mathbf{d} = -e\mathbf{r}$ where $\mathbf{r} = \mathbf{e}_{+1}^* r_{+1} + \mathbf{e}_0^* r_0 + \mathbf{e}_{-1}^* r_{-1}$. The tensor components of $\mathbf{r}$ are given by

$$r_{+1} = -\frac{x+iy}{\sqrt{2}}, r_0 = z, r_{-1} = -\frac{x-iy}{\sqrt{2}}. \tag{2.21}$$

where the signs are chosen to express the dipole operator as

$$\mathbf{d} = \sum_{F,m,F',m'}\left(d^-_{F,m;F',m'}\mathbf{e}_{+1}^* + d^0_{F,m;F',m'}\mathbf{e}_0^* + d^+_{F,m;F',m'}\mathbf{e}_{-1}^*\right)\hat{\sigma}_{F,m;F',m'} + h.c. \tag{2.22}$$

where F and m represent the ground states and F' and m' represent the excited states. The dipole moment components d^-, d^0 and d^+ are given by

$$\begin{aligned} d^-_{F,m;F',m'} &= -e\left\langle F,m\right| r_{+1}\left|F',m'\right\rangle, \\ d^0_{F,m;F',m'} &= -e\left\langle F,m\right| r_0\left|F',m'\right\rangle, \\ d^+_{F,m;F',m'} &= -e\left\langle F,m\right| r_{-1}\left|F',m'\right\rangle \end{aligned} \tag{2.23}$$

The general interaction Hamiltonian in the rotating wave approximation can be written as

$$\begin{aligned} \hat{H}_{int} = \hbar \sum_{F,m;F',m'} \int_0^L \Big(& [g^+_{F,m;F',m'}\hat{a}_+(z,t) \\ & + g^-_{F,m;F',m'}\hat{a}_-(z,t)]\hat{\sigma}_{F',m';F,m}(z,t) + h.c.\Big)\rho A dz \end{aligned} \tag{2.24}$$

where $g^{\pm}_{F,m;F',m'}$ is defined as $\sqrt{\omega_0/2\hbar\epsilon_0 A}d^{\pm}_{F,m;F',m'}$; L is the length of the atomic ensemble along direction of light propagation and ρ the atomic ensemble density along the same direction. The first term represents coupling the ground state $|F,m\rangle$ and the excited state $|F',m'\rangle$ in the atom with the product of the density operator $\hat{\sigma}_{F',m';F,m}(z,t)$ and the annihilation operator $\hat{a}_+(z,t)$ for a photon at position z with polarization σ_+. The factor $g^+_{F,m;F',m'}$ in the first term is the coupling constant for this transition which is non-zero for $m' = m+1$. These values can be calculated for ^{87}Rb in particular (given in Appendix B) and the complex conjugation in the expression can be omitted henceforth as the values turn out to be real. The interaction Hamiltonian in the off-resonant limit is developed as shown in Appendix A. The Hamiltonian Equation 2.24 can then be written in the off-resonant limit as the effective interaction Hamiltonian. The particular Hamiltonian for ^{87}Rb with its different terms is discussed in Section 3.1.1.

Chapter 3

Dispersive Detection of Linear Birefringent atoms

This chapter describes the dispersive detection of the atomic linear birefringence. QND measurements of the atomic spin by detecting the circular birefringence of atoms has been shown [93] [91] [92]. The technique in [93] has been used to generate spin squeezing in an atomic ensemble [39]. We discuss the use of the dispersive detection technique to perform QND measurements of the atomic spin.

Section 3.1 introduces the concept of dispersive detection of the linear birefringence by common path interferometry of the light polarization components. The Hamiltonian describing the interaction and the propagation equations for Stokes operators describing light polarization are given here. In Section 3.2, the set-up of our experiment is outlined. Section 3.3 discusses the state cleaning process used to prepare the atomic state before detection and Section 3.4 describes the experimental setup and sequence used. We discuss the dependence of the detection scheme on the light fields used in Section 3.5. Finally, Section 3.6 shows the detection of Rabi cycles in the two clock states of ^{87}Rb with this technique.

3.1 Linear Birefringence

An ensemble of atoms prepared in a magnetic sub-level behaves as an optically anisotropic medium to off-resonant light beams, i.e. the refractive index of the medium depends on the polarization of the light. This birefringence exhibited by the atoms permits non destructive detection of the atoms through the anaysis of their effect on the polarization of light. Circular birefringence, where the two circular components of light ($\sigma+$ and $\sigma-$ polarization components) see different refractive indices as they pass through the medium, gives rise to what is called Faraday rotation, that is analogous to the Faraday effect seen in crystals in the presence of a strong magnetic field. In our system, we consider the effect of the linear birefringence (where the σ and π components see different refractive indices) of the atoms in a state on polarized off-resonant light illustrated in Figure 3.1. Analysis of the polarization components after the interaction gives an estimate of the number of atoms in the state.

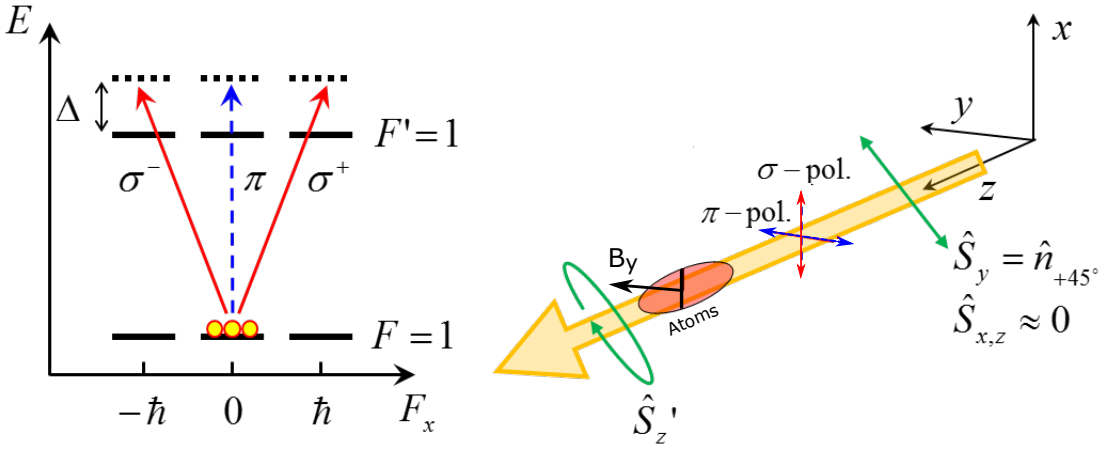


FIGURE 3.1: The figure illustrates the effect of atomic linear birefringence on off-resonant light with an example. In a), a simplified level scheme is shown for atoms in the $|F = 1, m_F = 0\rangle$ sublevel. When polarized light off-resonant from the $|F = 1\rangle \rightarrow |F' = 1\rangle$ transition is shone on the atoms, its σ components interact with the atoms, but the π component does not. In b), the conversion of linear polarization to elliptical polarization due to the interaction of the polarized light is shown with an example of atoms in a magnetic field. The typical values of the various parameters are discussed in later sections along with the optical setup in our experiment.

For example, when all the atoms are prepared in the $|F = 1, m_F = 0\rangle$ sublevel and linearly polarized light off - resonant from the $|F = 1\rangle \rightarrow |F' = 1\rangle$ transition is shone

on them, the σ components of the light interact with the atoms but the π component passes through unseen by the atoms due to the quantum selection rules forbidding the $|F = 1, m_F = 0\rangle \rightarrow |F' = 1, m_F = 0\rangle$ transition. This makes a common path interferometer measurement possible via polarization homodyning where linearly polarized light (comprising $\sigma+$ and $\sigma-$ components of equal strength) under interaction with the atoms becomes elliptically polarized due to the change in the two σ components. The ellipticity induced is proportional to the number of atoms and the Clebsch-Gordon coupling coefficients of the levels. Thus, circular analysis of the beam's polarization after interaction i.e. measuring the intensities of the two σ components gives us an estimate of the number of atoms in the $|F = 1, m_F = 0\rangle$ sub-level.

A more rigorous description of the effective interaction Hamiltonian and the propagation equations for the Stokes components is given in the following subsections.

3.1.1 Interaction Hamiltonian

In this section, we introduce the effective Hamiltonian for the interaction of ^{87}Rb atoms in the ground state hyperfine manifolds with polarized light in the off-resonant regime. We use optical frequencies in the $5^2S_{1/2} \rightarrow 5^2P_{1/2}$ transition, called the D1 line.

We start with the general Hamiltonian from Section A with new coefficients defined to give the expression

$$\begin{aligned}\hat{H}_{\text{int}}^{\text{eff}} = \int_0^L \Big\{ &\hat{a}_+^\dagger \hat{a}_+ \sum_m C^+(\Delta, m)\hat{\sigma}_{m,m} + \hat{a}_-^\dagger \hat{a}_- \sum_m C^-(\Delta, m)\hat{\sigma}_{m,m} \\ &+\hat{a}_-^\dagger \hat{a}_+ \sum_m b(\Delta, m)\hat{\sigma}_{m+1,m-1} + \hat{a}_+^\dagger \hat{a}_- \sum_m b(\Delta, m)\hat{\sigma}_{m-1,m+1} \Big\} \rho A dz \end{aligned} \tag{3.1}$$

It is to be noted that though we revert to using the $\hat{a}_+$ and the $\hat{a}_-$ notations, the terms actually represent the slow operators described in Equation A.2.

The terms containing $C^{\pm}(\Delta, m)$ describe the Stark shift of the ground state $|F, m\rangle$ caused by the coupling to the excited state $|F', m \pm 1\rangle$ as shown in Figure 3.2. The

terms containing $b(\Delta, m)$ describe the probability of changing the ground state by absorption and emission of σ photons, for example, going from the $|F, m-1\rangle$ state to the $|F, m+1\rangle$ state by absorbing a $\sigma+$ photon to an intermediate excited state $|F', m\rangle$ and emitting a $\sigma-$ photon from there as shown in Figure 3.2.

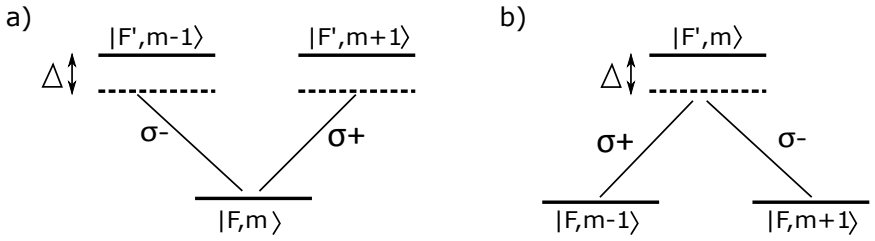


FIGURE 3.2: The figure illustrates the interactions in the Hamiltonian terms $C^{\pm}(\Delta, m)$ in a) corresponding to Equation 3.2 and $b(\Delta, m)$ in b) corresponding to Equation 3.3. More details are given in the text.

The coefficients $C^{\pm}(\Delta, m)$ and $b(\Delta, m)$ are given by

$$C^{\pm}(\Delta, m) = -2\hbar \sum_{F'} \frac{(g^{\pm}_{Fm,F'm\pm1})^2}{\Delta_{F'}} \tag{3.2}$$

$$b(\Delta, m) = -2\hbar \sum_{F'} \frac{(g^{+}_{Fm-1,F'm})(g^{-}_{Fm+1,F'm})}{\Delta_{F'}} \tag{3.3}$$

taking

$$g^{\pm}_{Fm,F'm'} = \frac{E_0 d^{\pm}_{Fm,F'm'}}{\hbar} \quad \text{with } E_0 = \sqrt{\frac{\hbar\omega_0}{2\epsilon_0 A}} \tag{3.4}$$

and

$$\begin{aligned} d^{\pm}_{Fm,F'm\pm1} =& (-1)^{J+I+m-F'-F}\sqrt{(2F+1)(2F'+1)(2J+1)} \\ &\times \begin{pmatrix} F & 1 & F' \\ m & \pm1 & -(m\pm1) \end{pmatrix} \begin{Bmatrix} F & F' & 1 \\ J' & J & I \end{Bmatrix} \langle J\|e\mathbf{r}\|J'\rangle \end{aligned} \tag{3.5}$$

The coefficients $C^{\pm}(\Delta, m)$ and $b(\Delta, m)$ are calculated in the Appendix B, in particular for the D1 line of ^{87}Rb.

The effective Hamiltonian for this interaction can then be written as

$$\begin{aligned}\hat{H}_{\text{int}}^{\text{eff}} = -\left(\frac{\hbar c\lambda^2\Gamma_{J'}}{8\pi A}\right)\int_0^L \Big\{ & 3\alpha_F^{(0)}[\hat{a}_+^\dagger\hat{a}_+ + \hat{a}_-^\dagger\hat{a}_-]\sum_m \hat{\sigma}_{m,m} \\ & + 3\alpha_F^{(+1)}[\hat{a}_+^\dagger\hat{a}_+ - \hat{a}_-^\dagger\hat{a}_-]\sum_m m\ \hat{\sigma}_{m,m} \\ & + 3\alpha_F^{(2)}\Bigg[(\hat{a}_+^\dagger\hat{a}_+ + \hat{a}_-^\dagger\hat{a}_-)\sum_m m^2\ \hat{\sigma}_{m,m} \\ & + \hat{a}_-^\dagger\hat{a}_+\sum_m\sqrt{(F+m)(F-m)(F+1+m)(F+1-m)}\hat{\sigma}_{m+1,m-1} \\ & + \hat{a}_+^\dagger\hat{a}_-\sum_m\sqrt{(F+m)(F-m)(F+1+m)(F+1-m)}\hat{\sigma}_{m-1,m+1}\Bigg]\Big\}\rho A dz \end{aligned} \quad (3.6)$$

This can be expressed as

$$\begin{aligned}\hat{H}_{\text{int}}^{\text{eff}} = -\left(\frac{\hbar c\lambda^2\Gamma_{J'}}{8\pi A}\right)\int_0^L \Big\{ & \alpha_F^{(0)}\hat{N} + 2\alpha_F^{(+1)}\hat{S}_z\hat{f}_z(z,t) \\ & + \alpha_F^{(2)}\left[\hat{N}\hat{f}_z^2(z,t) - \hat{S}_-\hat{f}_+^2(z,t) - \hat{S}_+\hat{f}_-^2(z,t)\right]\Big\}\rho A dz \end{aligned} \quad (3.7)$$

where the operators $\hat{\mathbf{f}}$ are used to describe a continuous medium of atoms, each with spin $\hat{\mathbf{F}}_\mathbf{i}$; the polarization operators $\hat{S}_\pm$ are defined as $\hat{S}_x \pm i\hat{S}_y$ and the spin operators $\hat{f}_\pm$ are given by $\hat{f}_\pm^2 = \sum_m \sqrt{(F+m)(F-m)(F+1+m)(F+1-m)}\hat{\sigma}_{m\pm1,m\mp1}$.

The different terms in Equation 3.6 represent couplings of light and atoms of different orders. The first term proportional to $\alpha_F^{(0)}$ is the zeroeth order coupling which gives a Stark shift to all the atomic states independent of internal state but proportional to total photon number $\hat{N}$. The term containing $\alpha_F^{(+1)}$ represents the first order coupling which rotates the Stokes vector $\mathbf{S}$ and the atomic spin vector $\mathbf{F}$ around the direction of light propagation. This is called Faraday rotation. The rest of the terms containing $\alpha_F^{(2)}$ represent second order coupling in the system. These terms describe the joint changes undergone by the light polarization components and the atomic spin components along the direction of light propagation, i.e. the z-axis. For example, the term $\hat{S}_-\hat{f}_+^2(z,t)$ changes the light angular momentum by $-2\hbar$ (in other words, a $\sigma+$ photon is converted to a $\sigma-$ photon) whereas the atomic angular momentum changes by $+2\hbar$ due to the raising operator $\hat{f}_+^2$. It is to be noted that the angular momentum of the total system along the z-axis

should remain unchanged as the system is axially symmetric along that direction. It is indeed evident that all the terms containing $\alpha_F^{(2)}$ conserve the total angular momentum along that direction.

We transform the Hamiltonian from the $\hat{f}_+, \hat{f}_-$ basis to the $\hat{f}_x, \hat{f}_y$ basis and from the $\hat{S}_+, \hat{S}_-$ basis to the $\hat{S}_x, \hat{S}_y$ basis with the following notations:

$$\hat{f}_x^2 - \hat{f}_y^2 = \frac{1}{2}(\hat{f}_+^2 + \hat{f}_-^2) \tag{3.8}$$
$$\hat{f}_x\hat{f}_y + \hat{f}_y\hat{f}_x = \frac{1}{2i}(\hat{f}_+^2 - \hat{f}_-^2)$$
$$\hat{S}_+ = -\hat{a}_+^\dagger \hat{a}_- = \hat{S}_x + i\hat{S}_y \tag{3.9}$$
$$\hat{S}_- = -\hat{a}_-^\dagger \hat{a}_+ = \hat{S}_x - i\hat{S}_y$$

The parameter $\hat{N}$ is written as $2\hat{S}_0$, the radius of the Poincaré sphere describing the light polarization, which is essentially proportional to the intensity of the light beam, i.e. the number of photons $\hat{N}$. Using these notations, we can transform the last two terms containing $\alpha_F^{(2)}$ in Equation 3.7 as:

$$(S_-\hat{f}_+^2 + S_+\hat{f}_-^2) = 2\hat{S}_x(\hat{f}_x^2 - \hat{f}_y^2) + 2\hat{S}_y(\hat{f}_x\hat{f}_y + \hat{f}_y\hat{f}_x) \tag{3.10}$$

These changes are made to account for the fact that experimentally, we can measure the polarization vector components in the x, y, z basis. With the above modifications, we write the final interaction Hamiltonian for Rb^{87} atoms on the D1 line transitions as:

$$\begin{aligned}\hat{H}_{\text{int}}^{\text{eff}} = &-2g\alpha_0 \int_0^L \Big\{\alpha_F^{(0)}\hat{S}_0 + \alpha_F^{(+1)}\hat{S}_z\hat{f}_z(z,t) \\ &+\alpha_F^{(2)}\left[\hat{S}_0\hat{f}_z^2(z,t) - \hat{S}_x(\hat{f}_x^2 - \hat{f}_y^2) - \hat{S}_y(\hat{f}_x\hat{f}_y + \hat{f}_y\hat{f}_x)\right]\Big\}\rho A dz\end{aligned} \tag{3.11}$$

As discussed previously, this Hamiltonian describes the coupling of the light polarization to the atomic spin with strengths of different orders magnitude and thus can be used for the interaction/detection scheme of any order dispersive effects. The dependence of the interaction on the detuning Δ is accounted for by the $\alpha_F^{(0)}$, $\alpha_F^{(1)}$ and $\alpha_F^{(2)}$ polarizability terms which vary as $1/\Delta$. The precise expressions are

calculated in Appendix.A and these coefficients are discussed in more detail in Section 3.5.

3.1.2 Detection of atomic linear birefringence with Stokes operator $\hat{S}_z$

To describe the effect of the atoms on the polarization of light, the propagation equations of the Stokes operators are derived considering the interaction between light and atoms. From the effective interaction Hamiltonian given in Equation 3.11, the Heisenberg equation for the Stokes vector $\hat{\mathbf{S}}$ can be derived as

$$(\partial_t + c\partial_z)\hat{\mathbf{S}}(z,t) = \frac{1}{i\hbar}[\hat{\mathbf{S}}(z,t), \hat{H}^{\text{eff}}] \tag{3.12}$$

The time derivative term $\partial_t\hat{\mathbf{S}}(z,t)$ can be ignored as the retardation of light propagating through short samples is negligible. This leaves the space derivative term $\partial_z\hat{\mathbf{S}}(z,t)$ which, using $[\hat{a}(z,t), \hat{a}^\dagger(z',t')] = \delta(z-z')$, can be expressed by the three following equations

$$\frac{\partial\hat{S}_x}{\partial z} = \frac{g^2A\rho(z)}{c\hbar}\left[-\alpha_F^{(1)}\hat{S}_y\hat{f}_z + \alpha_F^{(2)}\hat{S}_z(\hat{f}^2_{\nearrow} - \hat{f}^2_{\nwarrow})\right], \tag{3.13}$$

$$\frac{\partial\hat{S}_y}{\partial z} = \frac{g^2A\rho(z)}{c\hbar}\left[\alpha_F^{(1)}\hat{S}_x\hat{f}_z - \alpha_F^{(2)}\hat{S}_z(\hat{f}^2_x - \hat{f}^2_y)\right], \tag{3.14}$$

$$\frac{\partial\hat{S}_z}{\partial z} = \frac{g^2A\rho(z)}{c\hbar}\alpha_F^{(2)}\left[\hat{S}_y(\hat{f}^2_x - \hat{f}^2_y) + \hat{S}_x(\hat{f}^2_{\nearrow} - \hat{f}^2_{\nwarrow})\right] \tag{3.15}$$

where the 45° operators $\hat{f}_{\nearrow,\nwarrow}$ are given by $(\hat{f}_x \pm \hat{f}_y)/\sqrt{2}$.

From the Hamiltonian given in Equation 3.11, it can be observed that $\hat{S}_0$ terms only cause a global phase shift but do not affect the polarization of light. Thus these terms do not appear in the above equations along with the scalar polarizability $\alpha_F^{(0)}$. Furthermore, it is apparent that the optical anisotropic properties that are called circular and linear birefringence are connected to the vector and the tensor polarizability terms, i.e. the $\alpha_F^{(1)}$ and the $\alpha_F^{(2)}$ terms respectively. Linear polarisations $\hat{S}_{x,y}$ experience Faraday rotation about the z-axis, proportional to

$\alpha_F^{(1)}$ and longitudinal spin components $\hat{f}_z$. Similarly, the elliptical polarization $\hat{S}_z$ couples to $\hat{S}_{x,y}$ proportional to $\alpha_F^{(2)}$, depending on the alignment of transversal spin.

For the case of small optical phase shifts ($\ll 1$ rad), the induced rotations of the Stokes vector along the atomic ensemble will be small. If we also neglect back-action of light onto the atomic spin, we can approximate the right-hand sides of the Propagation Equations 3.13-3.15 to be constant. We consider strong classical probe light that is linearly polarized along the 45°-axes when it enters the atomic ensemble, i.e. $\hat{S}_{x,z} \approx 0$ and $\hat{S}_y \approx S_y$. In this case, Equations 3.13 and 3.15 reduce to describing circular and linear birefringence, respectively. Under these conditions and approximations, the resulting Faraday rotation of a probe beam after interaction with the atomic ensemble is given by

$$\hat{S}'_x = \hat{S}_x - \frac{\omega}{2\epsilon_0 c}\alpha_F^{(1)} S_y \int \hat{f}_z \rho(z) dz, \tag{3.16}$$

which measures atomic orientation along the z-axis. The first term in this result is the Stokes operator for the input light and is responsible for the photon shot noise in the polarimeter detection process whereas the second term measures atomic alignment with a signal strength that is proportional to photon flux S_y. Similarly, the resulting ellipticity due to linear birefringence reduces to

$$\hat{S}'_z = \hat{S}_z + \frac{\omega}{2\epsilon_0 c}\alpha_F^{(2)} S_y \int (\hat{f}_x^2 - \hat{f}_y^2)\rho(z) dz. \tag{3.17}$$

Assuming that all atoms are in the same state, or equivalently, for position independent spin, the birefringence provides a measure of atom number. Linear birefringence for atoms in an eigenstate of the individual $\hat{F}_y$-operator will be proportional to $\langle F, F_y | \hat{F}_x^2 - \hat{F}_y^2 | F, F_y \rangle = S_2(F_y)$. The moment $S_2(F_y)$ is given by the following equation

$$S_2(m) = \hbar^2 (F(F+1) - 3m^2) \tag{3.18}$$

where the angular momentum number m is in the F_y basis. The moment $S_2(m)$

is extremal for $m = \pm F$ as well as $m = 0$ for bosons (or $m = \pm 1/2$ for fermions). Intermediate Zeeman substates exhibit smaller linear birefringence. For our system of ^{87}Rb atoms, the values are given as

F \ m	−2	−1	0	+1	+2
1		−1	2	−1	
2	−6	3	6	3	−6

TABLE 3.1: The S_2 moments of different hyperfine levels

The ellipticity induced in the light polarization by atoms in a particular sub-level is proportional to the $S_2(m)$ moment of that level.

3.2 The cold atoms experimental setup

This section gives an overview of the cold atoms experimental setup used for the measurements in this thesis. It includes a brief description of the lasers used and the magnetic field sources. However, this thesis does not go into the realization and characterization of a MOT as the experiment already had a working MOT of ^{87}Rb atoms before I joined the lab; the details given in this section are for technical references.

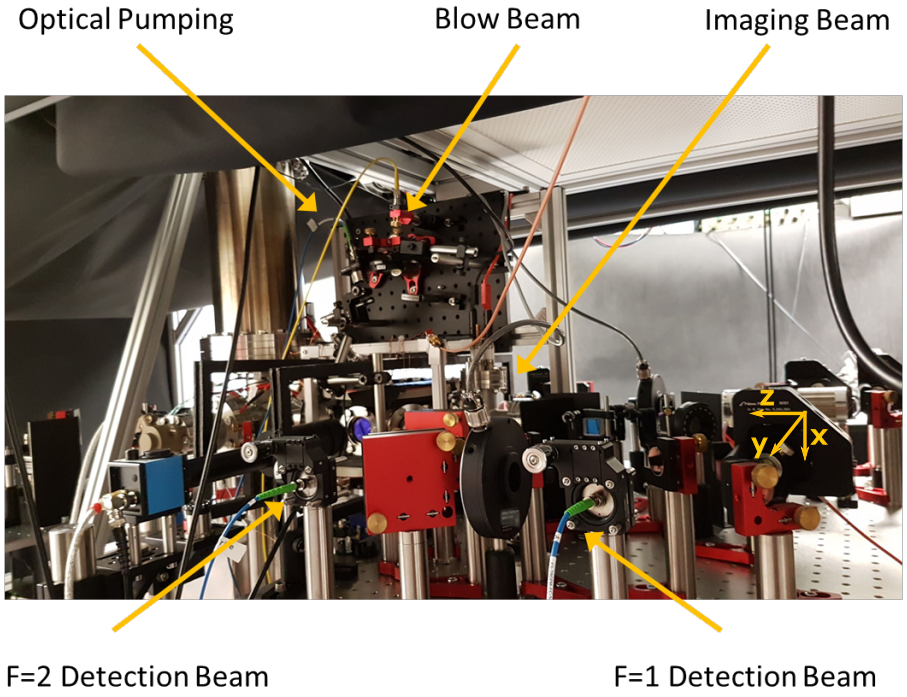
3.2.1 Set-up of Lasers and magnetic fields

This section gives a brief description of the different lasers used in the experiment with details on the transitions used and the laser locking setups. The details of the six lasers used are listed in the text below. Figure 3.3 shows the different fibre outputs in relation to the vacuum chamber and illustrates the paths of the laser beams. The transitions used for the various purposes are explained in Figure 3.4. The locking schematics for these six lasers are shown in Figure 3.5.

Repumper

A TOPTICA DL100 at 780 nm is used to provide the Repumper beam for the MOT preparation. It addresses the transition $|F = 1\rangle \rightarrow |F' = 2\rangle$ on the D2 line (the $5^2S_{1/2} \rightarrow 5^2P_{3/2}$ line). The laser is locked on the saturation absorption spectroscopy at the crossover peak between F' levels 1 and 2 by modulating the current to the laser. The beam is resonant to the transition which requires shifting the frequency by 78.5 MHz with an Acousto-Optic Modulator (AOM) before shining it on the atoms. It is aligned to co-propagate with one of the MOT beams through the bottom window of the UHV chamber shown.

Another beam is derived from this laser to a beat locking setup for the MOT Cooler laser.



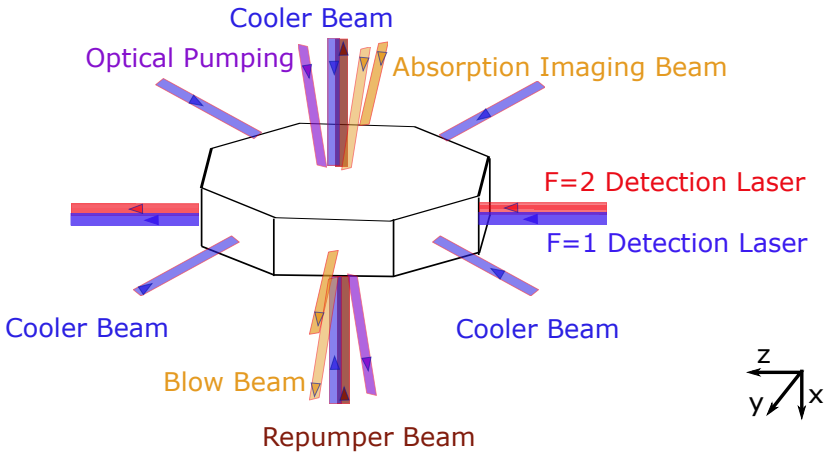


FIGURE 3.3: Lasers: The picture shows the experimental setup of the optics around the vacuum chamber for the various laser beams. The illustration shows the paths of the optical beams.

MOT Cooler Beam

A TOPTICA TA Pro at 780nm is used to provide the MOT Cooler Beams. The transition addressed is $|F = 2\rangle \rightarrow |F' = 3\rangle$ on the D2 line, red-detuned by 20MHz. The laser is locked on a beat signal between this beam and the Repumper. The beat is ≈6.8GHz and the frequency is selected by a high frequency discriminator using an an RF signal. The lock point is set by the frequency of the RF signal

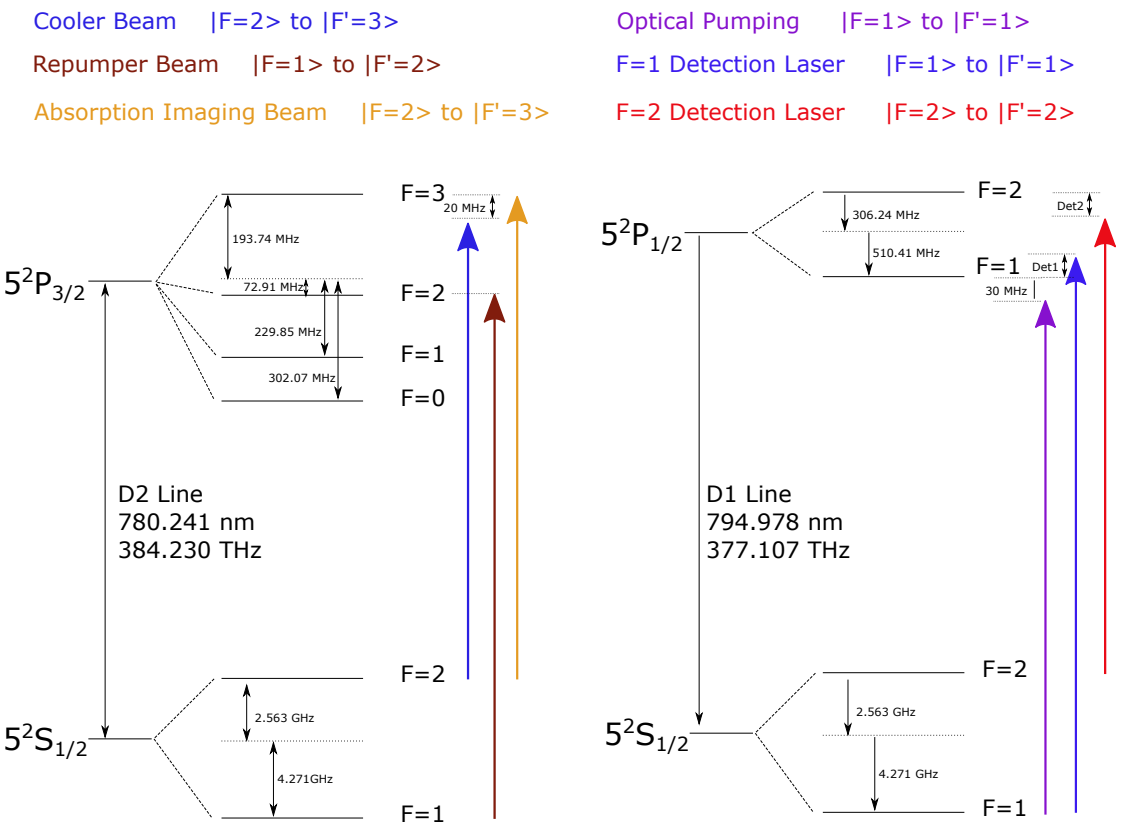


FIGURE 3.4: The figure shows the various optical transitions used in the experiment. The Cooler, Repumper and Absorption Imaging Beams are on the D2 line of ^{87}Rb at 780nm whereas the Optical Pumping, F=1 and F=2 Detection Beams are on the D1 line at 795nm. More details on the detunings of the transitions are given in the text.

input into the frequency discriminator.

The beam is σ polarized and detuned by 220MHz from the locked frequency by double passing it through an AOM (110MHz) before shining the beam on the atoms. The beam is divided into three separate beams that are retro reflected through the chamber.

Imaging

We use a homemade laser at 780nm for absorption imaging. The transition addressed is the resonant $|F = 2\rangle \rightarrow |F' = 3\rangle$ on the D2 line. The laser is locked on the saturation absorption spectroscopy at the crossover peak between F' levels 1 and 3 by modulating the current to the laser. The beam is detuned by 210MHz

to bring it to resonance with the transition (double passed through an AOM at 105MHz).

Another beam derived from this laser at the same frequency is used as a blow beam shone through another fibre at an angle from the top of the chamber. This blows away the atoms that absorb this frequency from the remaining atoms that are in a dark state.

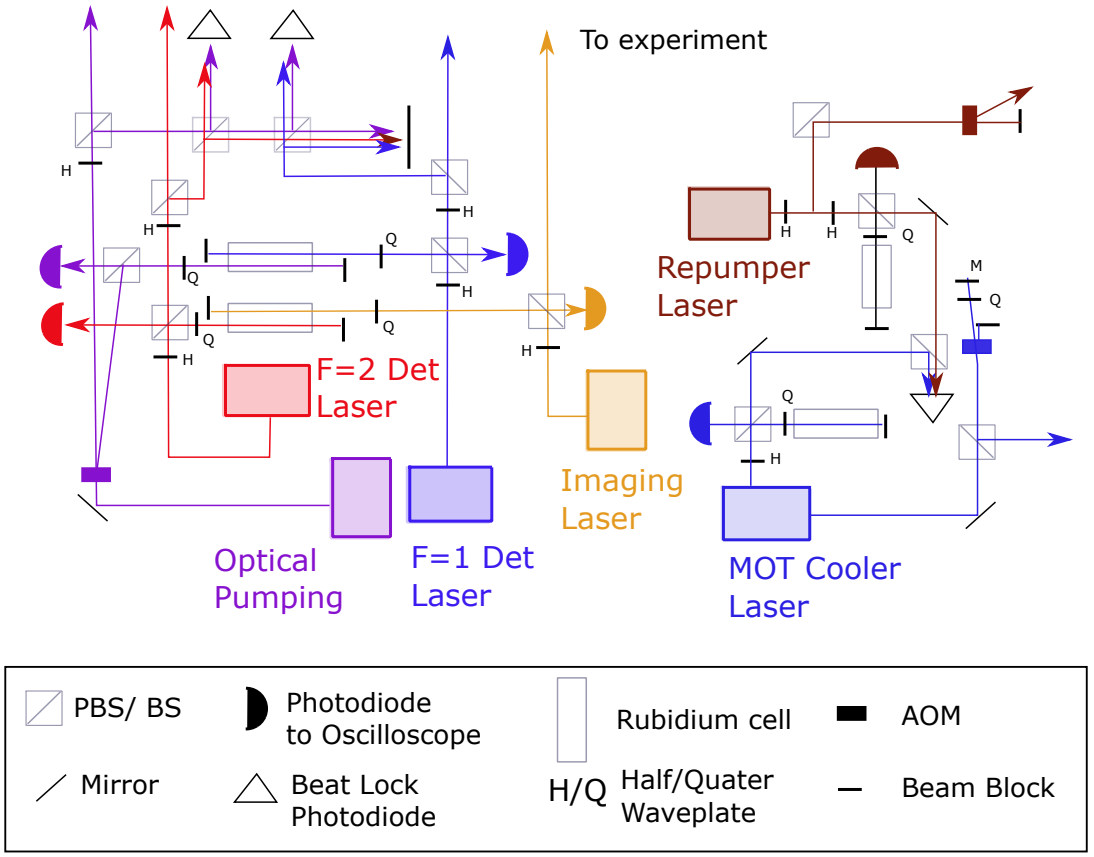


FIGURE 3.5: The figure illustrates the locking schemtaics used for the six lasers in the experiment. The Repumper, the Absorption Imaging laser and the Optical Pumping laser are locked on their spectroscopies. The MOT Cooler Laser is on a beat lock setup with the Repumper Laser, whereas the F=1 and F=2 detection lasers have a beat lock setup with the Optical Pumping laser (Hamamatsu model G4176 phhotodiodes).

Optical Pumping Laser

A homemade laser at 795 nm wavelength is used to provide a beam for optical pumping. The transition addressed is $|F = 1\rangle \rightarrow |F' = 1\rangle$ on the D1 line. The laser

is locked by modulating the saturation absorption spectroscopy signal from a Rb^{87} cell at the Lamb Dip.

This laser is also used as a reference signal in beat locking setups for the two detection lasers (for F=1 and F=2).

Detection Laser F=1

A TOPTICA DL100 laser at 795 nm is used as a detection laser for the atoms in the $|F = 1\rangle$ manifold on the $|F = 1\rangle \rightarrow |F' = 1\rangle$ D1 transition. The beam is off-resonant for dispersive detection.

Detection Laser F=2

A homemade laser at 795 nm is used as a detection laser for the atoms in the $|F = 2\rangle$ manifold on the $|F = 2\rangle \rightarrow |F' = 2\rangle$ transition. This beam is also off-resonant for dispersive detection.

Detection Lasers Locking

Figure 3.6 shows the locking and detuning schemes of the two Detection Lasers and the Optical Pumping Laser on the D1 line. The Optical Pumping Laser is locked on the spectroscopy signal detuned by 140 MHz with an AOM, at the Lamb Dip. The original beam is then detuned by 110 MHz with an AOM and used as the Optical Pumping Beam for the atoms (detuned by −30 MHz from the $|F = 1\rangle \rightarrow |F' = 1\rangle$ transition).

The Detection Laser for F=1 is locked on a fringe from the beat signal between this laser and the Optical Pump original beam as shown in Figure 3.5. The beat is < 1 GHz and the beam is detuned by −80 MHz with an AOM before coupling it into a fibre leading to the atoms. The beam can be detuned to different frequencies by locking on different fringes on the signals to give a variable detuning Det1 in

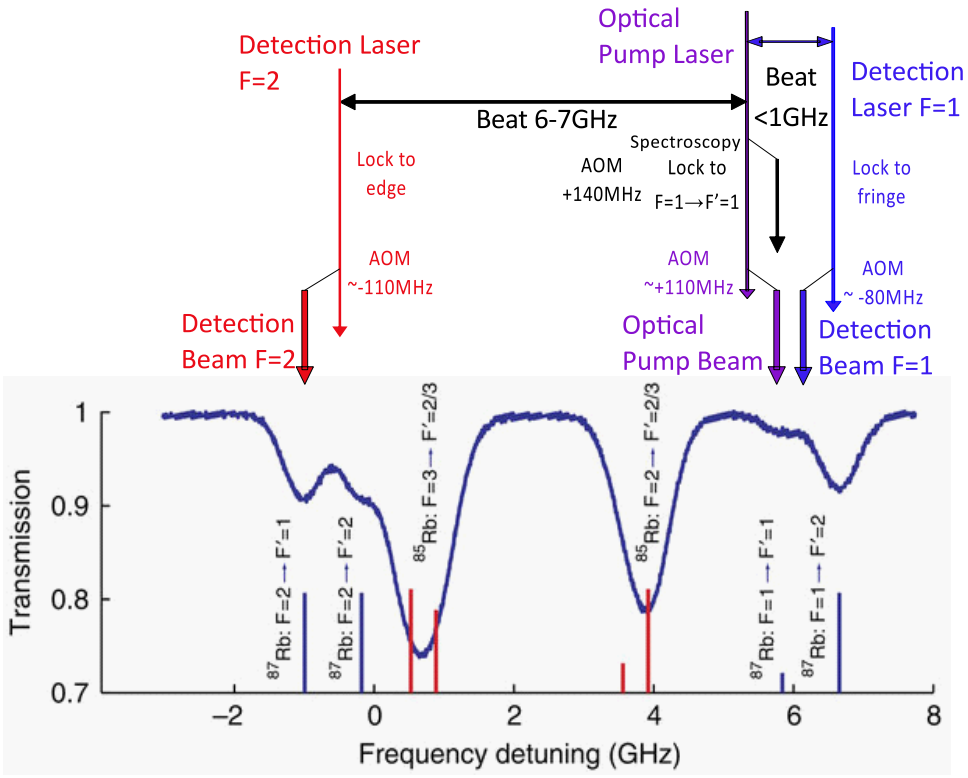


FIGURE 3.6: The figure shows the laser locking and detuning scheme for the Optical Pumping and the Detection Lasers, marking the locking frequencies and the detunings. The detunings of the two Detection Lasers can be varied, the optimal detunings are discussed in Section 3.5.

Figure 3.4. The Detection Laser for F=2 is also locked on the beat signal between this laser and the Optical Pump original beam as shown in Figure 3.5. The beat is ≈6.8 GHz and the frequency is selected by a high frequency discriminator using an an RF signal. The beam is detuned by −110 MHz before being coupled into a fibre to the atoms. The detuning Det2 can be changed by varying the RF signal that the discriminator uses to select the frequency.

Creation of magnetic fields

The Figure 3.7 shows the sources of the different magnetic fields used in the experiments in relation to the vacuum chamber.

The MOT coils create a spatially varying magnetic quadrupole field that enhances the effects of the Cooler Beams as the atoms move away from the centre of the

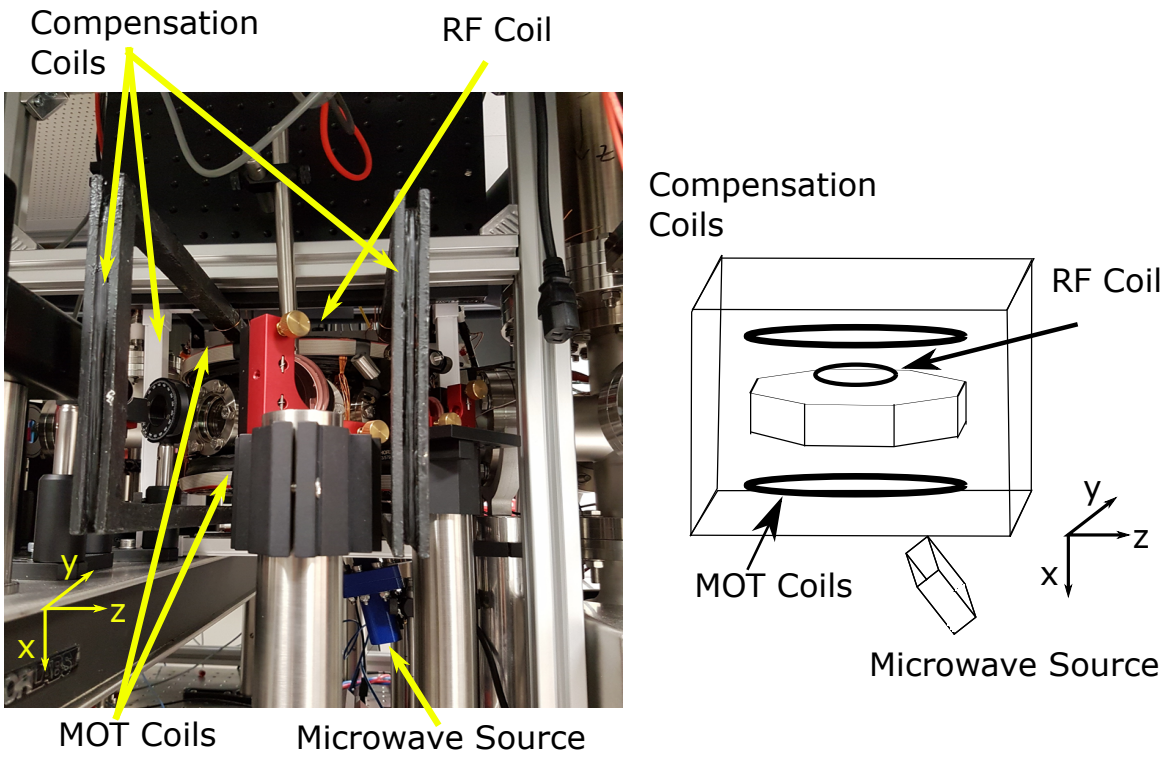


FIGURE 3.7: The figure shows the placement of the magnetic field sources involved in the experiment: the MOT coils, the static field coils for compensating external magnetic fields in the $x-, y-$ and $z-$ axes, the RF coil and the Microwave source.

trap. The compensation coils provide static magnetic fields in the three directions to eliminate the effects of external fields during the experimental runs. The Microwave field source is a waveguide directed towards the atoms connected to a vector signal generator (Rohde and Schwarz SMW200A) with the magnetic field component in the y-axis. The RF coil (that is used in experiments related in the latter half of the thesis) is placed above the vacuum chamber and generates an RF field along the x-axis.

3.2.2 MOT system

The atomic system used in our experiments is a cloud of cold ^{87}Rb atoms created in a UHV chamber with six Laser-Cooling beams (three σ polarized beams retro-reflected to form standing beams) and a weak magnetic field. The Figure 3.8 shows the vacuum chamber in our experimental setup with the optical setup for the three cooling beams and the magnetic field coils marked. A Repumper beam

is shone along one of the MOT cooling beams through the bottom window of the chamber.

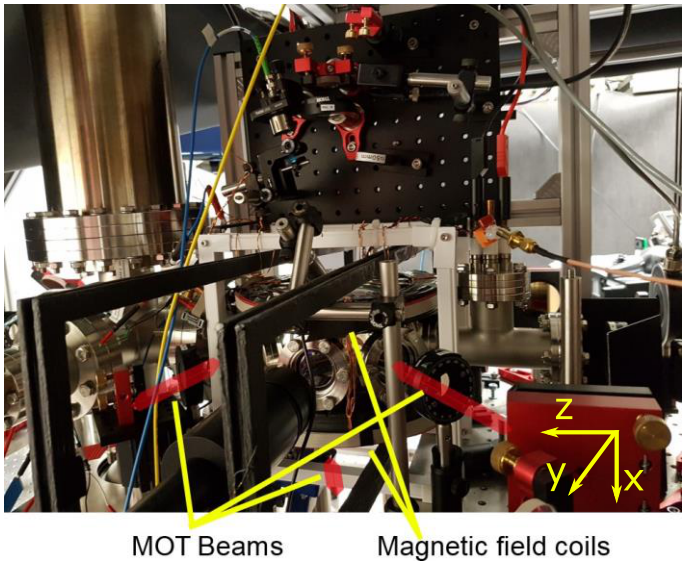


FIGURE 3.8: A close-up picture of the vacuum chamber is shown with the optical setup for the MOT beams and MOT coils marked.

The source of atoms is a dispenser connected to the chamber operated at a current typically in the range 3 – 5 A. Atoms from the background vapours are laser cooled and loaded into the MOT. A cMOT (condensed MOT) sequence is used to achieve a cloud of atoms with temperature below the 140 μK Doppler limit. Most experiments here are conducted with 1×10^8 atoms in the MOT at $\approx 80\mu$K. These laser beams and magnetic field coils are switched off and further experiments described in this thesis are performed on the freely falling atoms.

3.3 State Preparation of ^{87}Rb atoms in their clock states

This section describes the state cleaning process employed to prepare the atomic state in the $|F = 1; m_F = 0\rangle$ level. Starting from atoms prepared in a MOT, a series of optical pumping and microwave pulses are used as given in Figure 3.9a) with schematics of the hyperfine manifold shown to illustrate each step in Figures 3.9b)-f). The process is started with achieving a Dark MOT i.e. driving the atoms into the $|F = 1\rangle$ levels by leaving the Cooler beams on without the Repumper beam. This distributes the atoms among the $|F = 1\rangle$ levels nearly equally, with an imbalance in the $|m_F = \pm 1\rangle$ levels due to the asymmetric processes in the MOT. A π polarized optical pumping beam addressing the $|F = 1\rangle \rightarrow |F' = 1\rangle$ transition is shone on the atoms for a short time along with the Cooler beams. As the $|F = 1; m_F = 0\rangle \rightarrow |F' = 1; m_F = 0\rangle$ transition is forbidden by the quantum mechanical selection rules, the $|F = 1; m_F = 0\rangle$ level is left as a dark state during the optical pumping process and nearly 80% of the atoms gather in that state as shown in Figure 3.9b). The optical pumping process is discussed in more detail in Section 3.3.1.

A MW π pulse (of 24 dBm power which induces a 5.5 kHz Rabi cycle) transfers the atoms from $|F = 1; m_F = 0\rangle \rightarrow |F = 2; m_F = 0\rangle$ as shown in Figure 3.9c). This is done with the static field $B_x = 430$ mG parallel to the MW B field. This is immediately followed by a short Repumper pulse (Figure 3.9d)) which distributes the remaining atoms among the $F = 2$ levels, thereby increasing the number in the $m_F = 0$ level slightly. Another MW π pulse transfers the atoms back from $|F = 2; m_F = 0\rangle \rightarrow |F = 1; m_F = 0\rangle$ as shown in Figure 3.9e) and finally the few remaining atoms in the $|F = 2\rangle$ levels are blown away with a resonant blow beam and the beam used for absorption imaging as shown in Figure 3.9f). The efficiency of the whole state preparation process is given in Section 3.3.2. A MW pulse can be used after the State Preparation process to create a superposition of the clock states $|F = 1; m_F = 0\rangle$ and $|F = 2; m_F = 0\rangle$ that we wish to detect.

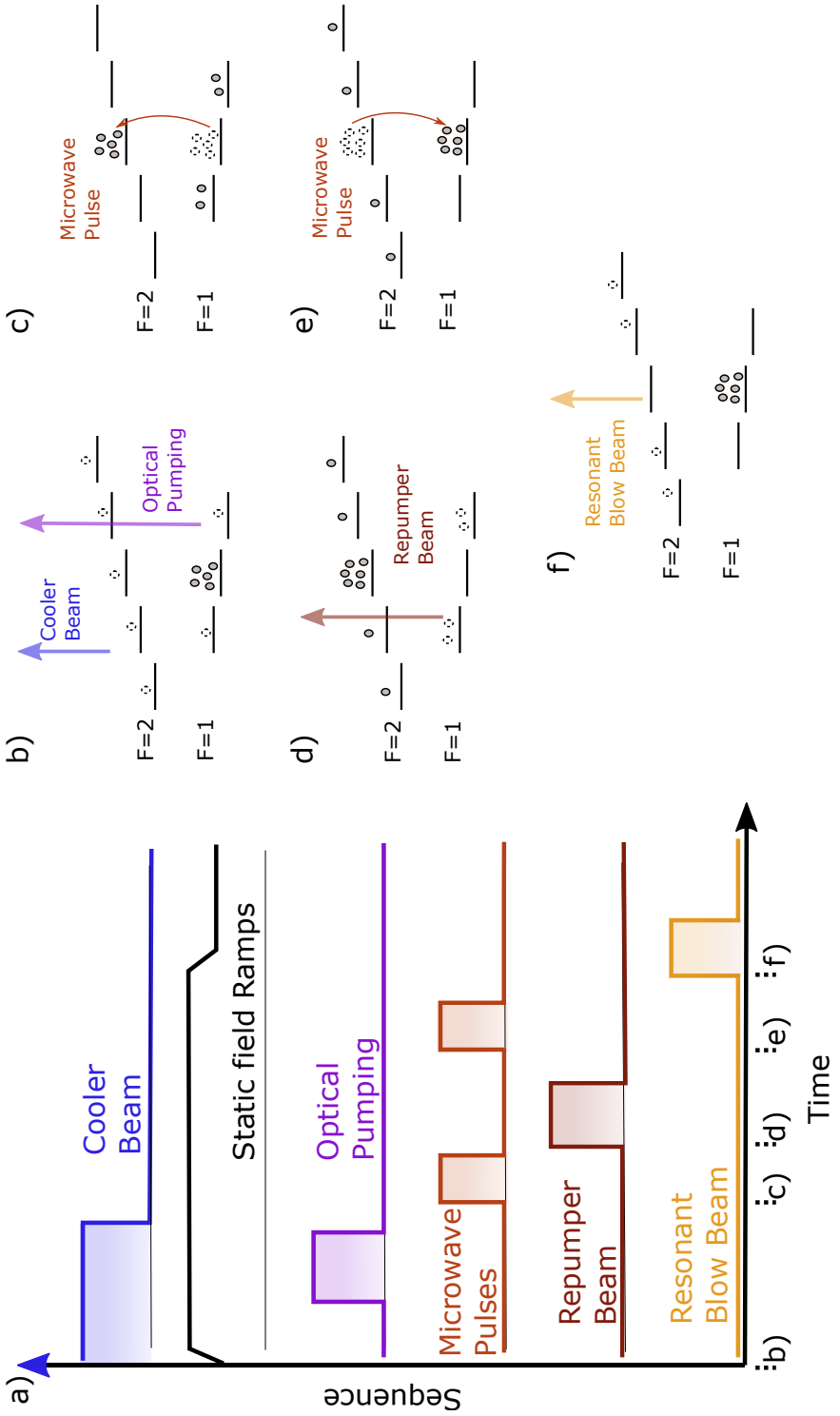


FIGURE 3.9: The figure shows the sequence and hyperfine manifold schematics of the various steps in the State Preparation Process. The Cooler Beams and Optical Pumping Beams together in panel b) collect most of the atoms in the $|F = 1, m_F = 0\rangle$ sublevel. The panel c) shows the MW pulse that excites the atoms to the $|F = 2, m_F = 0\rangle$ sublevel. The Repumper Beam in d) excites all the atoms to the $|F = 2\rangle$ levels, then another MW pulse in panel e) transfers the atoms from the $|F = 2, m_F = 0\rangle$ to the $|F = 1, m_F = 0\rangle$ level after which the remaining atoms in the $|F = 2\rangle$ levels are blown away with a Resonant Blow Beam.

3.3.1 Optical Pumping

This section gives the experimental characterization of the optical pumping used in the state preparation process. We use a laser beam red detuned by 30MHz from the $|F = 1\rangle \rightarrow |F' = 1\rangle$ transition on the D1 line to pump atoms from the $|F = 1, m_F = \pm 1\rangle$ levels with reduced re-absorption of scattered photons and let them gather in the $|F = 1, m_F = 0\rangle$ level. Absorption Imaging data from the $|F = 2\rangle$ state is shown in Figure 3.10 after the first MW pulse in the sequence Figure 3.9a).

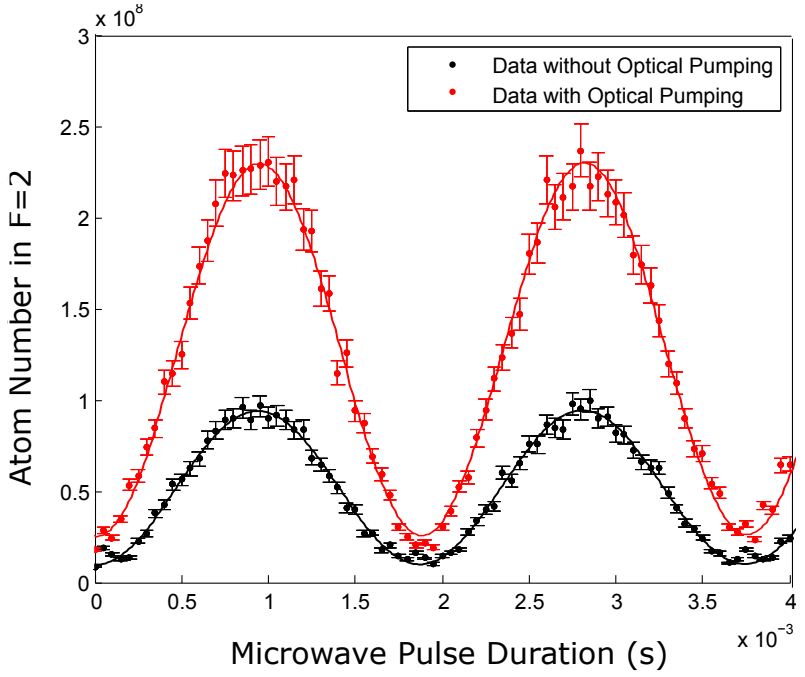


FIGURE 3.10: The figure shows the comparison between atom numbers in the $|F = 1; m_F = 0\rangle$ level with and without optical pumping in the State Preparation Process (Figure 3.9). The numbers are measured by Absorption Imaging of the $|F = 2\rangle$ level after a MW pulse trasferring atoms from the $|F = 1; m_F = 0\rangle$ to the $|F = 1; m_F = 0\rangle$ level. Starting with a MOT of 3×10^8 atoms, we find approximately 1×10^8 and 2.4×10^8 atoms in the $|F = 1, m_F = 0\rangle$ level without and with optical pumping respectively.

The data is taken with varied MW pulse durations after the optical pumping and the atom number in the $|F = 2\rangle$ state measured. A comparison of the atom number with and without Optical Pumping is shown to demonstrate its efficiency. The pumping increases the number in $|F = 1, m_F = 0\rangle$ from $\approx 33\%$ to $\approx 78\%$ in a MOT with 3×10^8 atoms. The efficiency of the pumping process is optimal with an intensity of $\approx 200 \mu W$ cm^{-2} and a pumping time of 2 ms. The intensity of the

beam is chosen to optimize the final temperature of the atoms in the cloud, which we measure with time-of-flight absorption imaging of the cloud, to be $(80 \pm 10)\mu$K.

3.3.2 Efficiency of the state preparation process

This section characterizes the efficiency of the state preparation process by comparing the atom number in the MOT and the number in the prepared state with varying MOT duration as given in Figure 3.11.

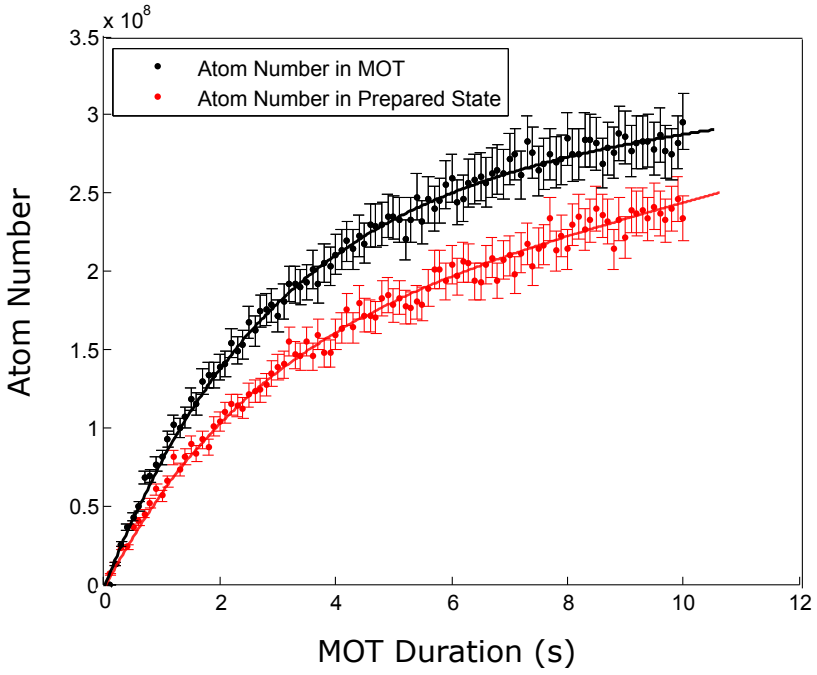


FIGURE 3.11: The figure shows the comparison of atom numbers in the MOT to the numbers in the $|F = 1, m_F = 0\rangle$ prepared state for varied MOT loading durations. The number in the prepared state is measured by Absorption Imaging of the $|F = 2\rangle$ levels after exciting the atoms to the $|F = 2, m_F = 0\rangle$ level with a MW π pulse. The model fit for the number of atoms is $N = a^* \exp(b^* x)$ where $a = (2.07 \pm 0.14) \times 10^8$, $b = 0.1 \pm 0.04$ for N in the prepared state and $a = (2.8 \pm 0.2) \times 10^8$, $b = 0.03 \pm 0.003$ for N in the MOT.

The increase in number due to optical pumping is supplemented by the increase due to the σ polarized Repumper pulse transferring some atoms from the $|F = 1, m_F \pm 1\rangle$ levels to the $|F = 2, m_F = 0\rangle$ level. The process achieves $(80 \pm 2)\%$ of the atoms in the MOT in the final prepared state. The data shows that the efficiency remains independent of the atom number over the range given.

3.4 Experimental detection of ^{87}Rb clock states

This section discusses the experimental aspects of the implementation of the atomic linear birefringence detection described in Section 3.1. The preparation of the laser beams and the setup of the detection system is described in Section 3.4.1. The experimental sequence followed to detect both the clock states in a MOT is outlined in Section 3.4.2.

3.4.1 Detection System

After preparing the atoms in their two clock states, we detect them with light beams of two different optical frequencies detuned from the $|F = 1\rangle \rightarrow |F' = 1\rangle$ and $|F = 2\rangle \rightarrow |F' = 2\rangle$ transitions of the ^{87}Rb D1 line respectively. The schematic of the detection system is given in Figure 3.12.

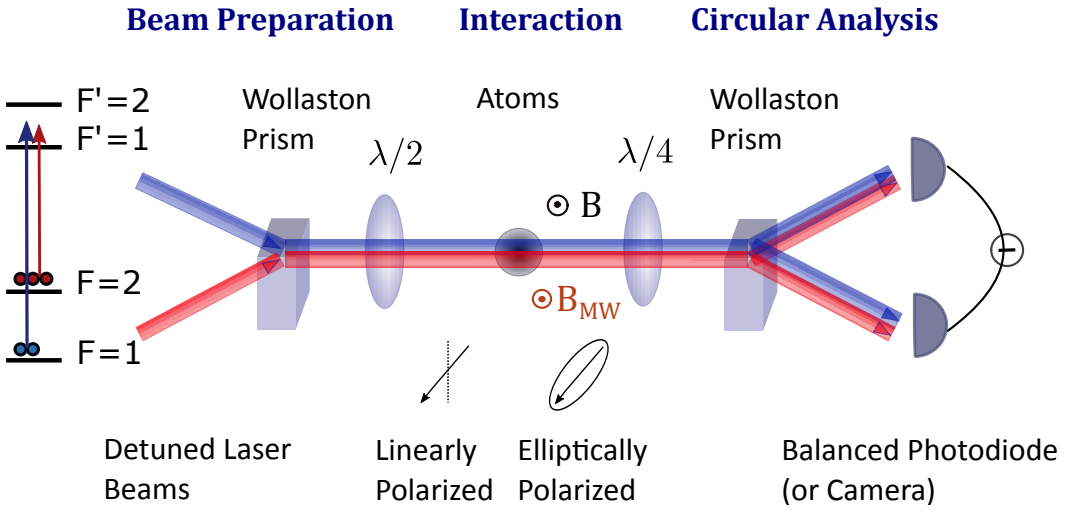


FIGURE 3.12: The figure shows the preparation of mutually orthogonal detection beams for the $|F = 1\rangle$ and $|F = 2\rangle$ states, their interaction with the atoms in a static magnetic field $\mathbf{B}$, typically ≈ 430 mG, and the circular analysis of the ellipticity induced in the beams with a balanced photodiode. A camera placed instead of the photodiode can be used for taking Dispersive images.

The two beams are prepared such that they are linearly polarized under 45° and their polarizations are mutually orthogonal. Thus, when they are shone along the two arms of a Wollaston Prism, which is a kind of polarizing beam splitter,

their paths are combined. Our Wollaston Prisms were specifically made to have an angle of 30° between their two arms. A $\lambda/2$ waveplate sets their angles of polarization to under 45° before the beams reach the atoms. A static magnetic field B along the x-axis provides a quantization axis and stabilizes the atomic spin. The detection beams traveling along the z-direction on interaction with the atoms become elliptically polarized due to the linear birefringence of the ensemble, as explained in Section 3.1.

A polarization homodyning measurement is performed by circular analysis of the ellipticity induced in the detection beams. The $\lambda/4$ waveplate converts the beams into circularly polarized beams, the components of which ($\sigma+$ and $\sigma-$) are separated by another Wollaston Prism similar to the first. A sample dispersive image of these two beams taken with a camera and referenced to an image without atoms is shown in Figure 3.13a) to illustrate the concept. The image is of atoms prepared

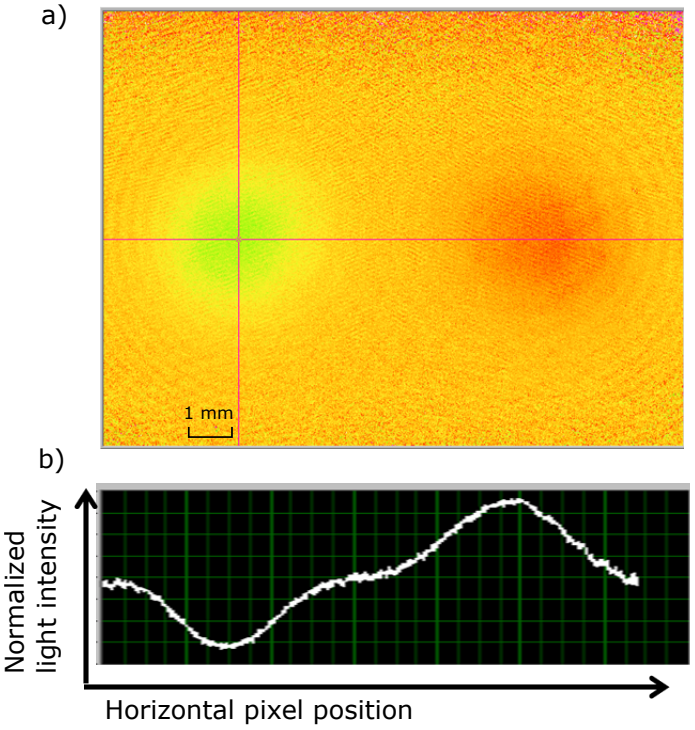


FIGURE 3.13: The figure shows a sample Dispersive Image of atoms in the $|F = 1\rangle$ taken with a camera placed instead of the photodiode in Figure 3.12. The image in a) shows the $\sigma+$ and $\sigma-$ components of the detection beam separated by a polarizing beam splitter after interaction with atoms, referenced to an image without atoms. The integrated light intensity in the vertical axis is given in b) with horizontal pixel position to show the reduction and increase in intensity of the two components.

in the $|F = 1, m_F = 0\rangle$ level taken with off-resonant light from the $|F = 1\rangle \rightarrow |F' = 1\rangle$ transition and shows the changed intensities of the two σ components of the light beam due to interaction with the atoms. A horizontal line-cut of the image Figure 3.13 b) shows that the effect on the intensities of the two circular components is equal and opposite. Therefore, when light linearly polarized under 45° is shone on the atoms, this effect makes it possible to estimate the number of atoms in the level by measuring the difference between the final intensities of the two circular components.

A Balanced Photodetector (ThorLabs model PDB210A) measures the difference in intensities of the two circular components, thereby measuring $\hat{S}_z$ discussed in Section 3.1.2 which gives us an estimate of the ellipticity induced in the detection beams and thereby the population of the respective states.

3.4.2 Two State Detection

Detection of both the clock states in a single experimental cycle is possible by shining the two detection beams consecutively. As the two manifolds have a separation of ≈ 6.8GHz, their interaction with the atomic cloud is dominated by the population in only one of the levels. The experimental sequence followed to measure the two populations is outlined in Figure 3.14.

The State Preparation process explained in Section 3.3 is performed as the atoms are in free fall after the MOT sequence to achieve a pure state i.e. $|F = 1; m_F = 0\rangle$ in Figure 3.14. A MW pulse of variable duration is used to drive the atoms and distribute them between the $|F = 1; m_F = 0\rangle$ and $|F = 2; m_F = 0\rangle$ states as shown in Figure 3.14b), the populations following a Rabi cycle with the duration of the MW pulse. The two detection beams are shone consecutively for $3 - 5$ ms and the signal from the balanced photodiode recorded in Figure 3.14c). Reference signals without atoms for both the detection beams are needed to account for the imbalance induced in the polarization components due to the different experimental conditions. Ideally, the two σ components are balanced to give a reference signal

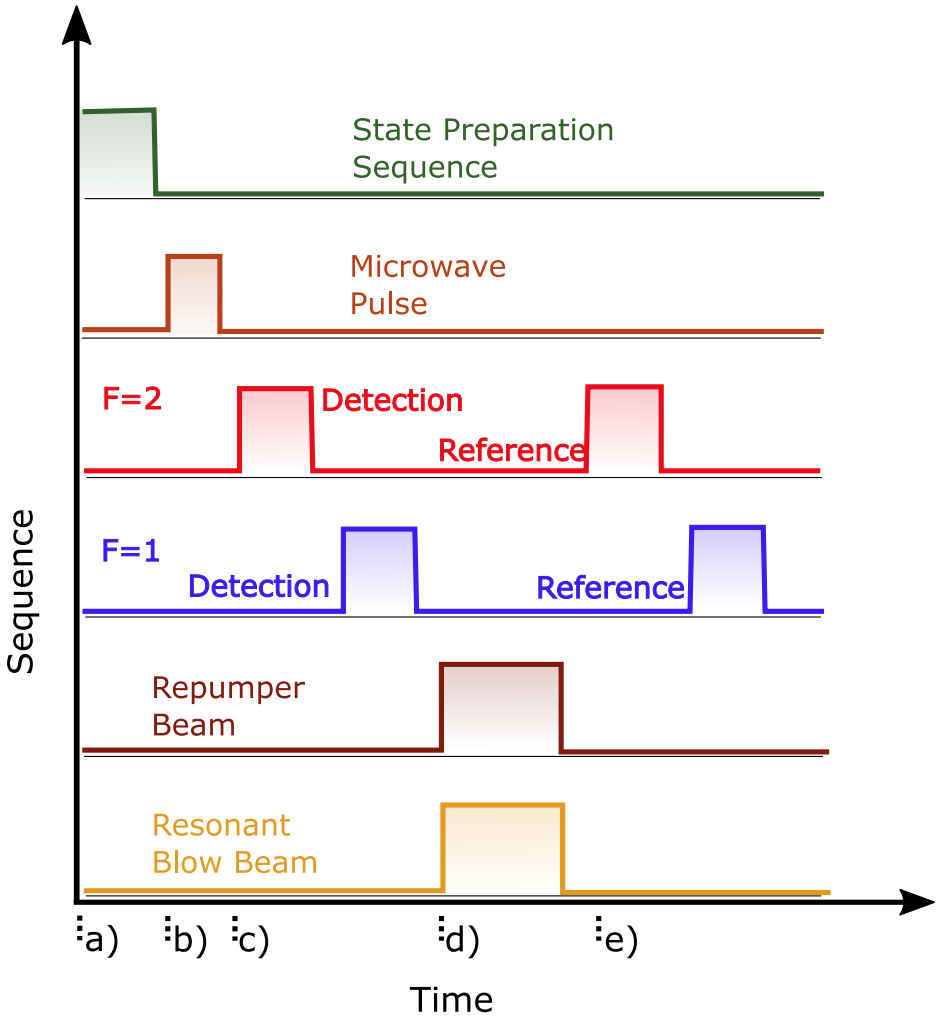


FIGURE 3.14: The figure shows the sequence of steps performed for obtaining dispersive signals from the two clock states. After the State Preparation Sequence (Figure 3.9), a MW pulse of variable duration is shone to excite the atoms in 5.5 kHz Rabi cycle between the two clock states. The Detection lasers are shone to interact with the atoms, then the Repumper and Resonant Blow Beams are used to remove the atoms before shining the Detection lasers again as reference signals.

of $0V$ when the $\lambda/2$ and $\lambda/4$ waveplates are perfectly aligned. The atoms are removed before the reference pulses by shining the resonant blow beam and the repumper beam together (Figure 3.14d)). The repumper beam transfers all the atoms from the $|F = 1; m_F = 0\rangle$ level to the $|F = 2\rangle$ levels and the blow beam resonant with the $|F = 2\rangle \rightarrow |F' = 3\rangle$ transition removes all the atoms from the ground state manifolds. This is followed by shining the two detection beams again (Figure 3.14e)) as reference pulses. Analysis of the Detection pulses with their respective Reference pulses gives an estimate of the atom numbers in the two levels.

3.5 Detection of atomic polarizability and decay coefficients

As the ellipticity induced in the light polarization in our detection scheme is proportional to the $\alpha_F^{(2)}$ coefficients, it is important to characterize these coefficients. In this section, we discuss the dependence of these coefficients with detection beam detuning and provide experimental evidence. From these experiments it is possible to arrive at a figure of merit that is best for this system.

The Hamiltonian considers off-resonant driving of atoms with total spin F to excited levels with electronic angular momentum J', which determines the scalar, vector and tensor parts $\alpha_{F,J'}^{(k)}$ of the polarizability. The polarizability terms for ^{87}Rb atoms in $F = 1, 2$ driven near the D1 lines ($J' = 1/2$) are derived in Appendix B and can explicitly be written as

$$\alpha_F^{(0)} = -\frac{\alpha_0}{3}\left[\frac{1}{\Delta_{F,1}} + \frac{3}{\Delta_{F,2}}\right] \tag{3.19}$$

$$\alpha_F^{(1)} = \frac{\alpha_0}{6}\left[\frac{2F-1}{\Delta_{F,1}} + \frac{(-1)^F 15/(2F+1)}{\Delta_{F,2}}\right] \tag{3.20}$$

$$\alpha_F^{(2)} = \frac{\alpha_0}{6}(-1)^F\left[\frac{-1}{\Delta_{F,1}} + \frac{1}{\Delta_{F,2}}\right] \tag{3.21}$$

where $\alpha_0 = 3\epsilon_0\lambda^3\Gamma/8\pi^2$ with the D1-line parameters $\Gamma = 2\pi \times 5.75$ MHz and $\lambda = 795$ nm. The detunings $\Delta_{F,F'} = \omega - \omega_{F,F'}$ are defined with respect to the optical $|F\rangle \rightarrow |F'\rangle$ transition frequencies. The ground- and excited state hyperfine splittings are $\Delta_{2,F'} - \Delta_{1,F'} \approx 2\pi \times 6834$ MHz and $\Delta_{F,2} - \Delta_{F,1} \approx 2\pi \times 817$ MHz. Due to this large difference and relatively small probe detunings used in our experiments, it is justified to treat the two $F = 1, 2$ sub-ensembles independently. The frequency dependence of the polarizability constants and expected spontaneous decay coefficients are shown together with experimental data in Figure 3.15.

The theoretical decay coefficients for the two sub-ensembles given in Figure 3.15a) are derived from the spontaneous emission rates of the levels per unit light power when using light polarized under 45° i.e equal π- and σ- components. Figure 3.15b)

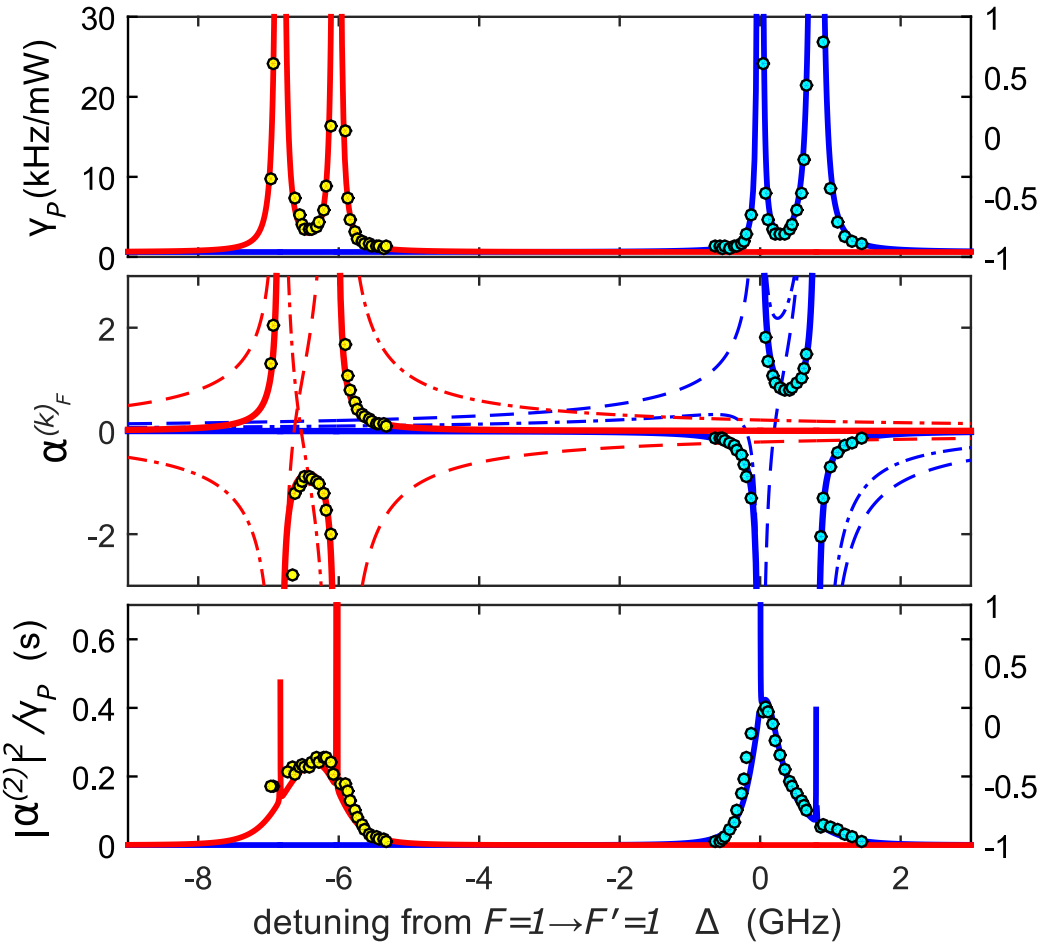


FIGURE 3.15: The figure shows the experimental data for the dependence of Linear Birefringence signals with detuning. Panel a) gives the dependence of the decay coefficients normalized to the light power γ_P. Panel b) gives the zeroth (dashed), first (dash-dotted) and second (solid) rank tensors of the D1 line polarizability with light field detuning. The experimental signal strengths (circles) match the $\alpha^{(2)}$ polarizability coefficients. The panel c) gives the figure of merit α^2/γ_P (discussed in the text) for these measurements.

gives the zeroeth, first and second rank tensors of the D1 line polarizability for the two states (where dashed, dash-dotted and solid lines for k = 0, 1 and 2).

Each data point in the graphs gives the experimental value of the signals measured by populating only one state and detecting it with the respective Detection Laser beam at a particular detuning. The two clock states are populated with $\approx 5 \times 10^7$ atoms and the linear birefringence signals and decays measured are referenced to light field measurements without atoms. The detunings of the two Detection light fields are changed as given in Section 3.2.1. The linear birefringence signal strengths match the theoretical $\alpha^{(2)}$ term polarizabilities as expected from the

discussion in Section 3.1.2. The decays of the states extracted by referencing the signals to those without atoms match the theoretical decay coefficients calculated after accounting for a decay in signal due to the fall of the atoms out of the light's path. These decay coefficients calculated take into consideration the powers of the two Detection light fields - 0.4 mW for the $F2$ detection laser and 1.1mW for the $F1$ detection laser.

The figure of merit κ^2 is derived by considering the scaling of the interaction strength κ with the canonical variables as

$$\kappa \propto \alpha^{(2)}\sqrt{N_A}\sqrt{N_P} \tag{3.22}$$

where κ is defined with the light and atom quadratures as $X_L = X_L^{(in)} + \kappa P_A$; N_A and P_A are the numbers of the interacting atoms and photons respectively. As $\gamma_P \propto 1/N_P$, we can derive the figure of merit to be

$$\kappa^2 \propto \alpha^2/\gamma_P \tag{3.23}$$

for a given atom number N_A. Figure 3.15c) gives the figure of merit with light field detuning for the two states. The optimal detuning at which to probe the two states is given by the detuning at which the figure is maximal. The optimal detuning for the detection of the $|F = 2\rangle$ levels is -400MHz from the $|F = 2\rangle \rightarrow |F' = 2\rangle$ transition and that for the detection of the $|F = 1\rangle$ levels is 80MHz from the $|F = 1\rangle \rightarrow |F' = 1\rangle$ transition. All the measurements discussed in the thesis henceforth use these powers and detunings for the two Detection lasers.

3.6 Detection of Rabi Cycles

This section discusses the detection of Rabi cycles in the two clock states by measuring state populations with the technique outlined in Section 3.4. These measurements are conducted with the powers and optimal detunings of the light fields determined in Section 3.5. Figure 3.16 shows the Rabi cycles detected in the two states driven by MW pulses of power 24 dBm.

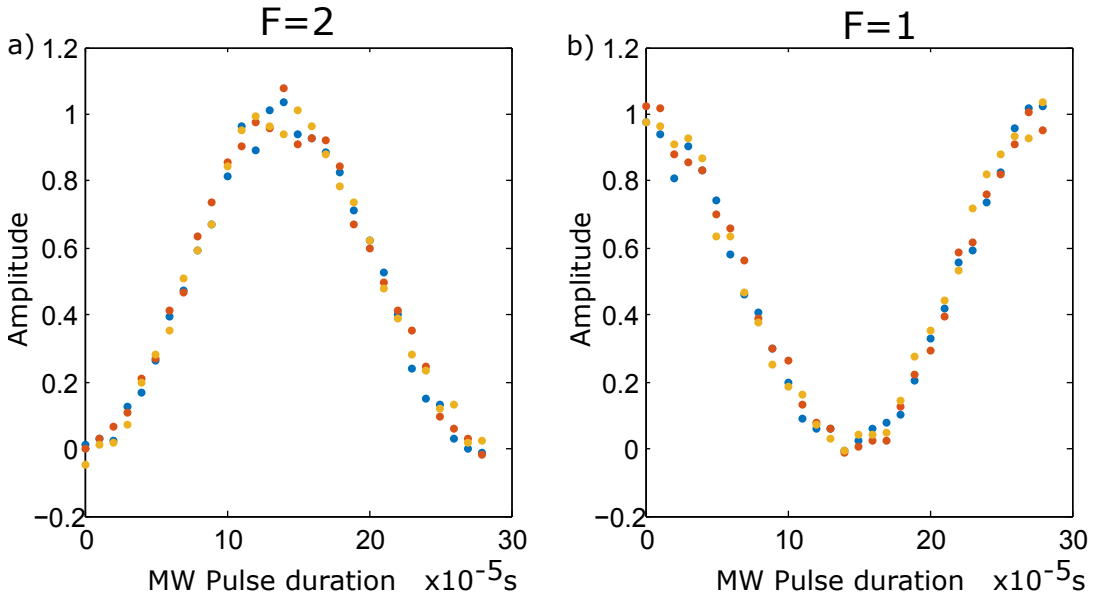


FIGURE 3.16: The figure shows the populations in the $|F = 2\rangle$ and $|F = 1\rangle$ states measured by the linear birefringence detection scheme (following the sequence in Figure 3.14) in panels a) and b) respectively with three repetitions. The MW pulse in the sequence excites the atoms in a Rabi cycle of 5.5 kHz between the two clock states. The signals of the atoms from each state are normalized to the signals measured beforehand with all the atoms in the respective state, thus the amplitudes seen oscillate between 0 and 1.

The Rabi cycles are observed by measuring the state populations at varied MW pulse durations. The signals from each state are normalized to atom number. However, as the number of atoms in each state are proportional to the total number of atoms in the MOT in that particular run, the measurements of individual Rabi cycles are affected by atom number fluctuations. The number of atoms in each state follow the models

$$n_1 = \frac{n_0}{2}(cos\phi), \quad n_2 = \frac{n_0}{2}(1 - cos\phi) \tag{3.24}$$

where n_0 is the total number of atoms in the MOT, n_1 is the number in the $|F = 1; m_F = 0\rangle$ level and n_2 is the number in the $|F = 2; m_F = 0\rangle$ level.

The Figure 3.17 shows the normalized difference of the two signals and their residuals from a model fit.

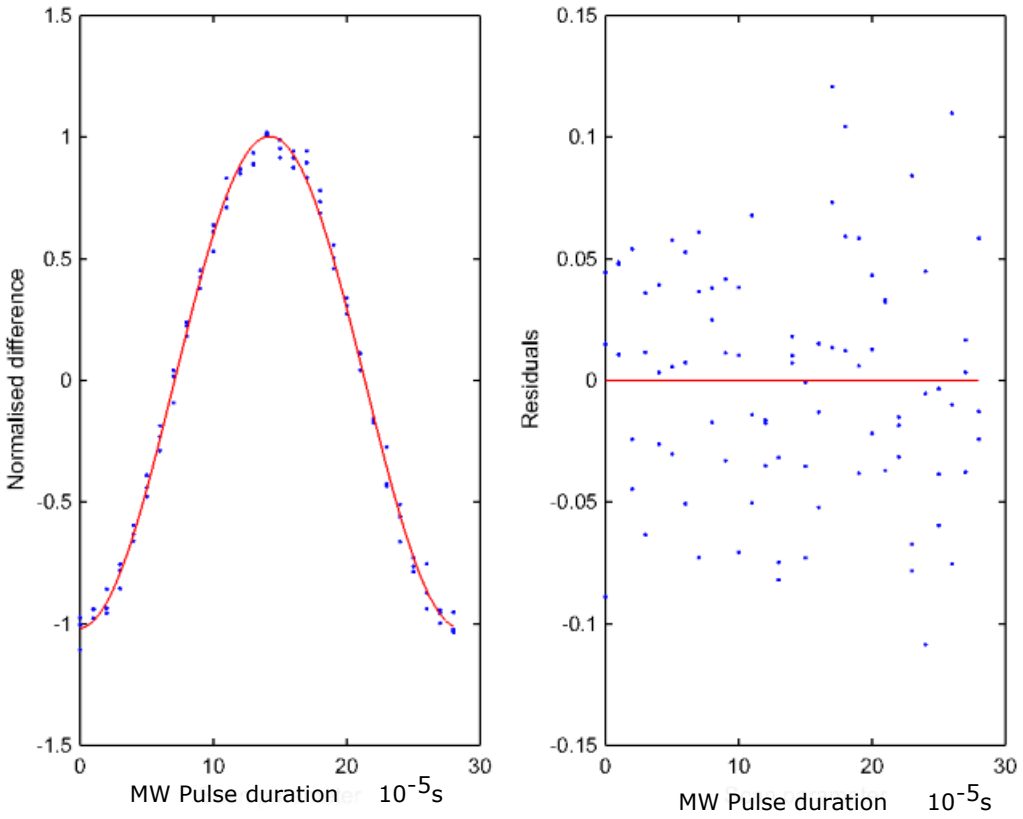


FIGURE 3.17: The figure shows normalized difference of the signals from the two clock states in a) with a model fit following Equation 3.25, $\sigma_z = 1.02\sin(0.23x + 4.58) - 0.01$. The normalized difference is calculated using the amplitudes shown in Figure 3.16. Panel b) shows the residuals of the data points with the model fit.

However, the population difference in the two states when normalized to the total population in the MOT measured in the same experimental run as in our case, will be insensitive to atom number fluctuations as the state transfer probability is given by

$$\sigma_z = \frac{n_2 - n_1}{n_2 + n_1} = \frac{n_0}{2n_0}(-2cos(\phi)) = -cos(\phi) \tag{3.25}$$

The noise in the measurement is observed to be $\approx 5\%$ of the total signals with this detection scheme.

Chapter 4

Radio-frequency Dressed Detection of Atomic Clock States

The linear birefringence detection scheme described in Chapter 3 is advantageous in terms of its non-destructive operation on atoms with the use of off-resonant detection light fields and ability to detect two states in the same experimental run to remove atom number fluctuations in the MOT formation stage. But the technique is still limited due to the presence of various technical noise sources like electronic noise common in these experimental setups. The detection lasers' intensity noise and relative frequency noise limit the common mode suppression of balanced detection as well as the suppression of atom number fluctuations possible with two-state detection. The polarization noise caused due to thermal drifts, acoustic noise and air movement in the beam preparation setup translates to noise in atom number signals from the individual states. Most of the technical noise sources in the experimental setup have low-frequency contributions. Modulating the linear birefringence signals from the atoms at a frequency higher than the common technical noise would suppress most of these noise contributions.

This chapter introduces the technique of dressing the atoms with an RF field before detection that would modulate the signals seen resulting in circumvention of low frequency noise contributions. Section 4.1 describes the Hamiltonian of an

atom in an RF field and the coupling of the hyperfine levels due to the interaction. Section 4.2 and Section 4.3 describe our experimental setup and give examples of the typical signals we see. Section 4.4 show our results of detecting Rabi cycles and Section 4.5 explains the possibility of state to quadrature mapping with our technique.

4.1 Modulation of signals by dressing atoms

This section describes the modulation of the atoms with RF dressing fields. The theory of adiabatic RF dressing of atoms and the dressed linear birefringence discussed in Sections 4.1.1 and 4.1.2 are developed in conjunction by the co-authors of our paper [94].

The linearly polarized RF field introduced just before the detection of atoms has equal components of $\sigma+$ and $\sigma-$ polarizations. Figure 4.1 shows the coupling of the two hyperfine sub-manifolds induced by the RF field.

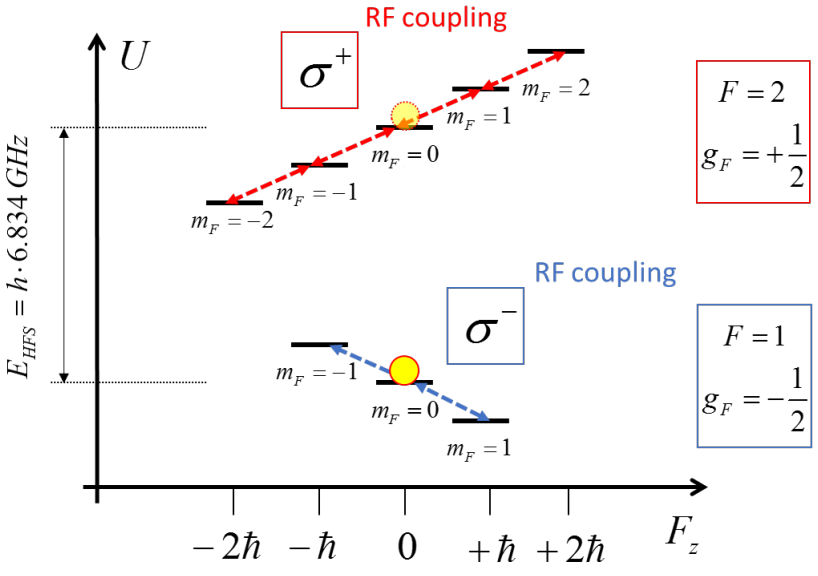


FIGURE 4.1: The figure illustrates the coupling of the hyperfine levels due to the RF field in the atomic ensemble (yellow) prepared in a superposition of the two clock states $|F, m\rangle : |1, 0\rangle$ and $|2, 0\rangle$. The linearly polarized RF field has equal components of $\sigma+$ and $\sigma-$ polarizations which couple the $|F = 2\rangle$ and the $|F = 1\rangle$ levels respectively.

When the static magnetic field affecting the Zeeman splitting of the atomic levels is at the resonance condition with the RF field applied, i.e. $\mu_B g_F B_{DC} = \hbar\omega_{RF}$, the $\sigma+$ and $\sigma-$ components of the RF field couple the $|F=2\rangle$ and the $|F=1\rangle$ levels respectively. The atomic spins precess around the static field due to the RF coupling, which modulates the atomic signal $\langle F_x^2 - F_y^2\rangle$ discussed in Section 3.1.2. This modulation of the signals at a frequency of the same order as that of the RF field applied suppresses noise contributions at lower frequencies. The linear birefringent signals from RF dressed atoms are discussed in more detail in Section 4.1.2.

4.1.1 Adiabatic Radio-frequency Dressing

This section describes the adiabatic RF dressing of the atoms and derives the interaction Hamiltonian between the atomic spin and the applied magnetic field given by

$$\mathbf{B}(t) = \mathbf{B}_{\mathrm{RF}}(\omega t) + \mathbf{B}_{\mathrm{DC}}, \tag{4.1}$$

The Interaction Hamiltonian of an atom with spin $\mathbf{F}$ of constant magnitude in the effective magnetic field $\mathbf{B}_{\mathrm{eff}}$ when the second order Zeeman splitting is neglected can be written as

$$\hat{H} = \frac{\mu_B g_F}{\hbar}\hat{\mathbf{F}}\cdot\left(\mathbf{B}_{\mathrm{RF}}(\omega t) + \mathbf{B}_{\mathrm{DC}}\right), \tag{4.2}$$

The oscillating part of the magnetic field $\mathbf{B}_{\mathrm{RF}}(\omega t)$ is best expressed in terms of the spherical polarization components. Using the spherical basis $\mathbf{e}_\pm = (\mathbf{e}_x \pm i\mathbf{e}_y)/\sqrt{2}$ and $\mathbf{e}_\pi = \mathbf{e}_z$, and choosing $\mathbf{B}_{\mathrm{DC}} = B_{\mathrm{DC}}\mathbf{e}_z$, we can write

$$\mathbf{B}_{\mathrm{RF}}(\omega t) = \mathrm{Re}\left[(B_+\mathbf{e}_+ + B_-\mathbf{e}_- + B_\pi\mathbf{e}_\pi)e^{-i\omega t}\right]. \tag{4.3}$$

Using corresponding spin components with the conventional normalization of raising and lowering operators $\hat{F}_\pm = \hat{F}_x \pm \hat{F}_y$, the Hamiltonian can be expressed as

$$\hat{H} = \frac{\mu_B g_F}{2\hbar}\left[\left(\frac{B_+}{\sqrt{2}}\hat{F}_+ + \frac{B_-}{\sqrt{2}}\hat{F}_- + B_\pi \hat{F}_z\right)e^{-i\omega t} + B_{\mathrm{DC}}\hat{F}_z\right] + h.c. \tag{4.4}$$

We transform to a frame rotating about the z-axis at frequency ω with a given phase φ, such that $\hat{H}_{\mathrm{rot}} = \hat{U}\hat{H}\hat{U}^{-1} + i\hbar\frac{\partial}{\partial t}\hat{U}\hat{U}^{-1}$, using the unitary transformation

$$\hat{U}_\pm = e^{i(\pm\omega t+\varphi)\hat{F}_z/\hbar}, \tag{4.5}$$

where the sign of frequency is chosen equal to the sign of the Landé factor g_F, which determines the sense of rotation that is required to dress atoms resonantly. Using the identity $e^{\alpha\hat{F}_z}\hat{F}_\pm e^{-\alpha\hat{F}_z} = e^{\pm\alpha}\hat{F}_\pm$, the rotating frame Hamiltonian becomes

$$\hat{H}^\pm_{\mathrm{rot}} = \frac{\mu_B g_F}{2\hbar}\left[\frac{B_\mp e^{\mp i\varphi}}{\sqrt{2}}\hat{F}_\mp e^{-2i\omega t} + B_\pi \hat{F}_z e^{-i\omega t} + \frac{B_\pm e^{\pm i\varphi}}{\sqrt{2}}\hat{F}_\pm + \left(B_{\mathrm{DC}} - B_{\mathrm{res}}\right)\hat{F}_z\right] + h.c., \tag{4.6}$$

where we introduced the positive, resonant field B_{res} as

$$B_{\mathrm{res}} = \pm\hbar\omega/\mu_B g_F \tag{4.7}$$

If the RF field is polarized purely in the $\mathbf{e}_\pm$ direction that corresponds to the Larmor precession, i.e. $B_\mp = B_\pi = 0$, atoms will exhibit the same behavior as in an apparently static, effective field

$$\mathbf{B}^\pm_{\mathrm{eff}} = \frac{1}{2}\left(B_\pm e^{\pm i\varphi}\mathbf{e}_\pm + c.c.\right) + \left(B_{\mathrm{DC}} - B_{\mathrm{res}}\right)\mathbf{e}_z, \tag{4.8}$$

described by the corresponding effective, rotating frame Hamiltonian

$$\hat{H}^\pm_{\mathrm{eff}} = \frac{\mu_B g_F}{\hbar}\hat{\mathbf{F}}\cdot\mathbf{B}^\pm_{\mathrm{eff}}. \tag{4.9}$$

In particular, an atomic spin will adiabatically follow the effective field's orientation provided that any reorientation with $\dot{\mathbf{B}}_{\mathrm{eff},\perp} = \boldsymbol{\Omega}\times\mathbf{B}_{\mathrm{eff}}$ occurs at a rate that

is much slower than the effective Larmor frequency, i.e. for $|\mathbf{\Omega}| \ll \mu_B g_F |\mathbf{B}_{\text{eff}}|/\hbar$. When other RF-polarization components are present, the rotating wave approximation can be used, thus neglecting the fast oscillating terms of $\hat{H}_{\text{rot}}$ as long as $\omega \gg \mu_B g_F |\mathbf{B}_{\text{eff}}|/\hbar$. The resulting behaviour remains the same apart from second order energy shifts.

We now consider the specific transformation of atomic spin operators when an eigenstate of $\hat{F}_z$, initially prepared in a static field along the z-direction, is dressed by adiabatically changing the components of the effective field. Here, we assume an RF field that is linearly polarized in the x, y-plane, described by

$$\mathbf{B}_{\text{RF}}(\omega t) = B_{\text{RF}} \cos \omega t \cdot (\mathbf{e}_x \cos \varphi + \mathbf{e}_y \sin \varphi), \tag{4.10}$$

for which case $B_\pm = B_{\text{RF}} e^{\mp i\varphi}/\sqrt{2}$ and $B_\pi = 0$. Consequently, we find for either effective field

$$\mathbf{B}^{\pm}_{\text{eff}} = \frac{B_{\text{RF}}}{2}\mathbf{e}_x + (B_{\text{DC}} - B_{\text{res}})\mathbf{e}_z. \tag{4.11}$$

The initial state $|F, F_z\rangle$ for $B_{\text{RF}} = 0$ is identical in both laboratory and rotating frame apart from the evolution of the dynamical phase or quasi-energy, which we can ignore for our purposes. Upon changing the effective field, we obtain the adiabatic state by the corresponding rotation about the (rotating) y-axis according to

$$|\Psi_{\text{rot}}\rangle = e^{i\theta \hat{F}_y} |F, F_z\rangle, \tag{4.12}$$

by an angle

$$\theta = \frac{\pi}{2} - \tan^{-1} \frac{B_{\text{DC}} - B_{\text{res}}}{B_{\text{RF}}/2}. \tag{4.13}$$

The same state in the laboratory frame is then given by

$$|\Psi(t)\rangle = \hat{U}^{-1}_{\pm}(t) |\Psi_{\text{rot}}\rangle. \tag{4.14}$$

Finally, we can express any laboratory frame observable $\hat{O}$ using

$$\langle \Psi(t)| \hat{O} |\Psi(t)\rangle = \langle F, F_z| \hat{R}_\pm \hat{O} \hat{R}_\pm^{-1} |F, F_z\rangle , \tag{4.15}$$

$$\hat{R}_\pm(t) = e^{-i\theta \hat{F}_y} \hat{U}_\pm(t). \tag{4.16}$$

The result is a time-dependent geometrical rotation of coordinates given by the explicit transformation

$$\begin{aligned} \hat{\mathbf{F}}'(t) &= \hat{R}_\pm(t) \hat{\mathbf{F}} \hat{R}_\pm^{-1}(t) = \mathbf{R}_\pm(t) \hat{\mathbf{F}} \\ &= \begin{pmatrix} \cos\theta \cos\phi_\pm(t) & -\sin\phi_\pm(t) & -\sin\theta\cos\phi_\pm(t) \\ \cos\theta \sin\phi_\pm(t) & \cos\phi_\pm(t) & -\sin\theta\sin\phi_\pm(t) \\ \sin\theta & 0 & \cos\theta \end{pmatrix} \hat{\mathbf{F}}, \end{aligned} \tag{4.17}$$

where we introduced $\mathbf{R}_\pm(t) = \mathbf{R}_z(\phi_\pm(t))\mathbf{R}_y(-\theta)$ as a combination of rotations about coordinate axes according to $\mathbf{R}_k\mathbf{v} = \mathbf{e}_k(\mathbf{e}_k \cdot \mathbf{v})(1-\cos\alpha) + \mathbf{v}\cos\alpha + \mathbf{e}_k \times \mathbf{v}\sin\alpha$ and the time dependent angle $\phi_\pm(t) = \pm\omega t + \varphi$.

This transformation is used in Section 4.1.2 to describe the linear birefringence signals from the atoms in the effective magnetic field given by Equation 4.1.

4.1.2 Dressed linear birefringence

To consider different experimental geometries, in particular for light propagation parallel or orthogonal to the static field, we use rotated light coordinates, expressed by a general rotation matrix $\mathbf{M}$, such that $(x', y', z')^T = \mathbf{M}(x, y, z)^T$. Linear birefringence of eigenstates of the dressed Hamiltonian is then measured by

$$\begin{aligned} \left\langle \hat{S}_{z'}(t) \right\rangle &= \xi \langle F, F_z| \hat{F'}^2_{x'}(t) - \hat{F'}^2_{y'}(t) |F, F_z\rangle \\ &= \xi \langle F, F_z| \hat{\mathbf{F}}^T \mathbf{Q}_\pm \hat{\mathbf{F}} |F, F_z\rangle , \end{aligned} \tag{4.18}$$

where ξ is the experimental gain, and we introduce the quadratic form

$$\mathbf{Q}_{\pm} = \mathbf{R}_{\pm}^{T}(t)\mathbf{M}^{T}\begin{pmatrix} 1 & 0 & 0 \\ 0 & -1 & 0 \\ 0 & 0 & 0 \end{pmatrix}\mathbf{M}\mathbf{R}_{\pm}(t) \tag{4.19}$$

Since the matrix $\mathbf{Q}_{\pm}$ is symmetric and the expectation values of mixed anti-commutators vanish $\langle F, F_z|\{\hat{F}_j, \hat{F}_k\}|F, F_z\rangle_{j\neq k} = 0$, the expression for the signal reduces to the trace

$$\left\langle \hat{S}_{z'}(t)\right\rangle = \xi \sum_{k=1}^{3} Q_{\pm}^{k,k}\hat{F}_k^2, \tag{4.20}$$

which we express in terms of spectral RF components $h_n(\theta)e^{in\omega t}$ as

$$\left\langle \hat{S'}_z(t)\right\rangle = \frac{\xi}{2}S_2(F_z)\sum_{n=0}^{2} h_n(\theta)e^{in\omega t} + c.c. \tag{4.21}$$

We can restrict the description of light geometry to two degrees of freedom, because rotations about the laboratory fixed z-axis are equivalent to a rotated RF field, already described by φ. We choose $\mathbf{M} = \mathbf{R}_x(\alpha)\mathbf{R}_y(\beta) = \mathbf{R}_{y'}(\beta)\mathbf{R}_x(\alpha)$ leading to the result

$$\begin{aligned}&(h_0, h_1, h_2)^T(\theta) = \\ &\begin{pmatrix} \frac{1+3\cos 2\theta}{4}\left(\frac{\cos^2\beta}{2} - \frac{\cos 2\alpha(3-\cos 2\beta)}{4}\right) \\ \sin 2\theta\left(\frac{\cos\alpha\sin 2\beta}{2} \mp i\frac{\sin 2\alpha(3-\cos 2\beta)}{4}\right)e^{\pm i\varphi} \\ -\sin^2\theta\left(\frac{\cos^2\alpha(3-\cos 2\beta)+2\cos 2\beta}{4} \mp i\frac{\sin\alpha\sin 2\beta}{2}\right)e^{\pm 2i\varphi} \end{pmatrix}.\end{aligned} \tag{4.22}$$

For the parallel setting $\alpha = \beta = 0$, the chosen coordinate systems for atomic and light variables coincide. Including first order effects from small misalignment, i.e. for small $\alpha, \beta \ll 1$ and thus neglecting second order terms, we find

$$\begin{pmatrix} h_0 \\ h_1 \\ h_2 \end{pmatrix}_{\parallel}(\theta) \approx \begin{pmatrix} 0 \\ (\beta \mp i\alpha)e^{\pm i\varphi}\sin 2\theta \\ -e^{\pm 2i\varphi}\sin^2\theta \end{pmatrix}. \tag{4.23}$$

A setting with light propagation orthogonal to the static field is described by $\beta = \pi/2 + \delta_\beta$ where we assume a small misalignment of beam direction by $\delta_\beta \ll 1$ as well as $\alpha \ll 1$, which now describes a rotation of beam polarisation. For small deviations, we arrive at

$$\begin{pmatrix} h_0 \\ h_1 \\ h_2 \end{pmatrix}_{\perp}(\theta) \approx \begin{pmatrix} -\frac{1}{4}\left(1 + 3\cos 2\theta\right) \\ (\delta_\beta \mp 2i\alpha)e^{\pm i\varphi}\sin 2\theta \\ -\frac{1}{2}e^{\pm 2i\varphi}\sin^2\theta \end{pmatrix}. \tag{4.24}$$

The results show that due to the axial symmetries of both the setup and the initial state, a parallel measurement (Equation 4.23 with $\alpha = \beta = 0$) only produces signals at frequency $2\omega_{RF}$ as the only non-zero component in Equation 4.23 would be the h_2 component at $2\omega_{RF}$ frequency. This setting also leads to the maximum possible signal oscillation with full swing between $\pm\xi S_2(m)$ when the RF resonance condition $\theta = 0$ is met. The orthogonal setting contains a DC part that is reminiscent of undressed detection with off-resonant amplitude -$\xi S_2(m)$ and leads to a weaker signal at $2\omega_{RF}$ on resonance with an amplitude swing between 0 and $\xi S_2(m)$. In both cases, a signal at frequency ω_{RF} arises only due to misalignment, with a zero crossing at resonance, i.e. at $\theta = 0$.

When the static field is at RF resonance, the changes in magnitude of the static field B_{DC}, which shifts the resonance condition, and the field rotations or equivalent beam misalignment affect the resonant $2\omega_{RF}$-signal only to second order. Since the RF amplitude has no effect, it is advantageous to use higher RF amplitudes to broaden the resonance. The signal becomes less sensitive to fluctuations of external magnetic fields reducing the requirements for magnetic field shielding. A limit to this strategy will be imposed by effects from second order Zeeman splitting. Here, it must be noted that the RF resonance condition given by Equation 4.7 is not met at the same field magnitude for the two states as $g_{F=1} \neq g_{F=2}$. Thus, when Equation 4.7 is met for one state, the other state will be more susceptible to static magnetic field fluctuations. This is discussed in more detail with noise analysis in Section 5.3.3.

4.2 Experimental setup

This section discusses the incorporation of the RF dressing of the atoms into the experimental setup of atomic linear birefringence detection. The detection scheme and the experimental sequence are discussed in Section 4.2.1 and Section 4.2.2 respectively.

4.2.1 RF Dressed Detection Scheme

A linearly polarized RF field is applied in the x-direction through a coil (with 4 turns and a radius of 4.3 cm) above the vacuum chamber to adiabatically dress the atoms with a magnetic field (≈ 10 mG) of frequency $\omega_{RF} = 2\pi \times 180$ kHz. The $|F = 2\rangle$ and the $|F = 1\rangle$ sub-levels are coupled by the $\sigma+$ and the $\sigma-$ components of the linearly polarized RF field respectively. The experimental setup modified slightly from that shown in Section 3.4.1 to account for RF dressing is shown in Figure 4.2.

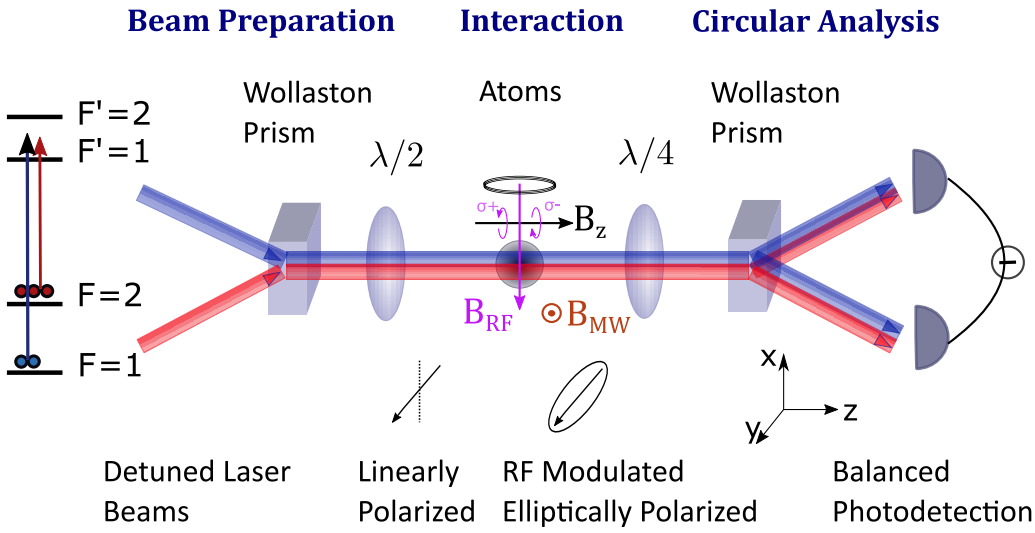


FIGURE 4.2: The figure shows the detection scheme of linear birefringent signals with the application of RF dressing field B_{RF}. The paths of the two detection beams for the $|F = 1\rangle$ level (blue) and the $|F = 2\rangle$ level (red) are outlined. The scheme is similar to Figure 3.12 except for the direction of the static field and the introduction of the RF field.

The RF field's amplitude and frequency are controlled by a function generator. The amplitude is ramped slowly to adiabatically dress the atoms. At nearly the same time, the static fields in the chamber are ramped such that the atomic Larmor frequency is resonant with the RF field. This procedure maintains the magnitude of the total collective spin as well as its alignment with the effective field such that the initial atomic spin projection $F_z = 0$ then rotates within the x, y-plane. While the total populations within each F-manifold remain unchanged, the atomic state then obeys $F_x \cos(\omega_{\mathrm{RF}} t) \pm F_z \sin(\omega_{\mathrm{RF}} t) = 0$, where the sign of rotation depends on the state-dependent Landé factor g_F. Due to this, the signals from the atoms are modulated thereby circumventing low-frequency technical noise. To optimize the signal to photon shot noise ratio, the two detection laser beams are focused such that the beams are mode-matched to the falling MOT at the time of detection as shown in Figure 4.3. This ensures that all the light detected by the photodiode has interacted with the atoms as opposed to the situation before mode-matching where a large fraction of the light contributes to the photon shot noise without contributing to the signal from the atoms. Reducing the size of the beam and mode-matching it to the atomic cloud maximizes the signal to noise ratio.

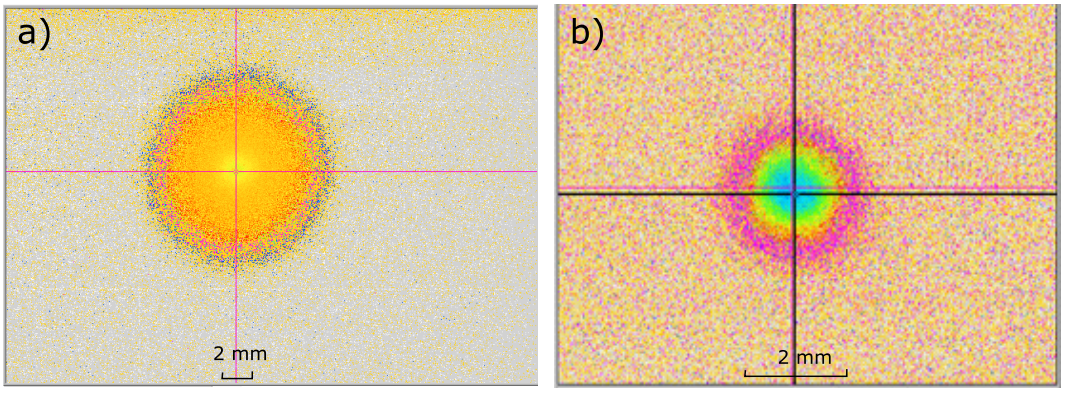


FIGURE 4.3: Mode Matching Detection Beams: Figure gives comparison of sample dispersive images of falling atoms in the $|F = 1\rangle$ level before mode-matching the F=1 Detection Beam to the atomic cloud in a) and after mode-matching in b). The images are taken similar to the image shown in Figure 3.1, except that these images show only one of the σ components of the $F = 1$ detection beam after circular analysis. This is sufficient to align the beam to the MOT at the time of detection as shown by the cursors marking the centre of the atomic cloud.

The function generator signals to the RF coil are amplified with a power amplifier

to get ≈ 3 Vpp voltage across the coil. The signals from the atoms are amplified with an RF amplifier (model ZFL1000+ from minicircuits). The DC components of the signals are removed using a high pass filter as the modulation of the signals makes them redundant. Thus, the laser reference pulses for the detection along with the atom removal sequence (Repumper + Resonant Blow Beams) used in the Two State DC detection sequence (Section 3.4.1) are also made unnecessary.

4.2.2 Experimental Sequence of RF Dressed Detection

The experimental sequence used to adiabatically dress the atoms and detect the two states is given in Figure 4.4. The state preparation sequence (at Figure 4.4b)) and the MW pulse (at Figure 4.4c)) remain the same as in the DC detection scheme shown previously in Figure 3.14.

The RF field is ramped up to nearly 15 mG over a duration of 3 ms (Figure 4.4d)) to adiabatically dress the atoms and the static magnetic fields are ramped at the same time to a magnitude of B_{DC} = 260 mG in the z-direction, i.e. the direction of propagation of beams. The fields in the transverse directions are reduced to compensate the external magnetic fields. The static fields can be oriented in two directions as discussed in Section 4.1.2. The direction chosen for most of the experiments described in the thesis is parallel to the direction of propagation to the light fields as this gives the higher signal from the same number of atoms (oscillating between ±1 as opposed to oscillating between 0 and 1 in the orthogonal case, calculated using Equations 4.23 and 4.24). The amplitudes of the two detection pulses are ramped by modulating the AOM voltages (Figure 4.4e)). This prevents the low-frequency modulation of the atomic signal due to the effect of the light fields on the atomic levels. The whole sequence is set to a trigger from the RF voltage generator so that the signals from the atoms are phase locked to the RF fields. This is achieved by introducing a hold time in the experimental sequence after the MOT duration for the atoms to be released with a trigger from the 50 Hz mains AC line which sets the PXI system (a PC based platform from National Instruments for experimental sequence control) to

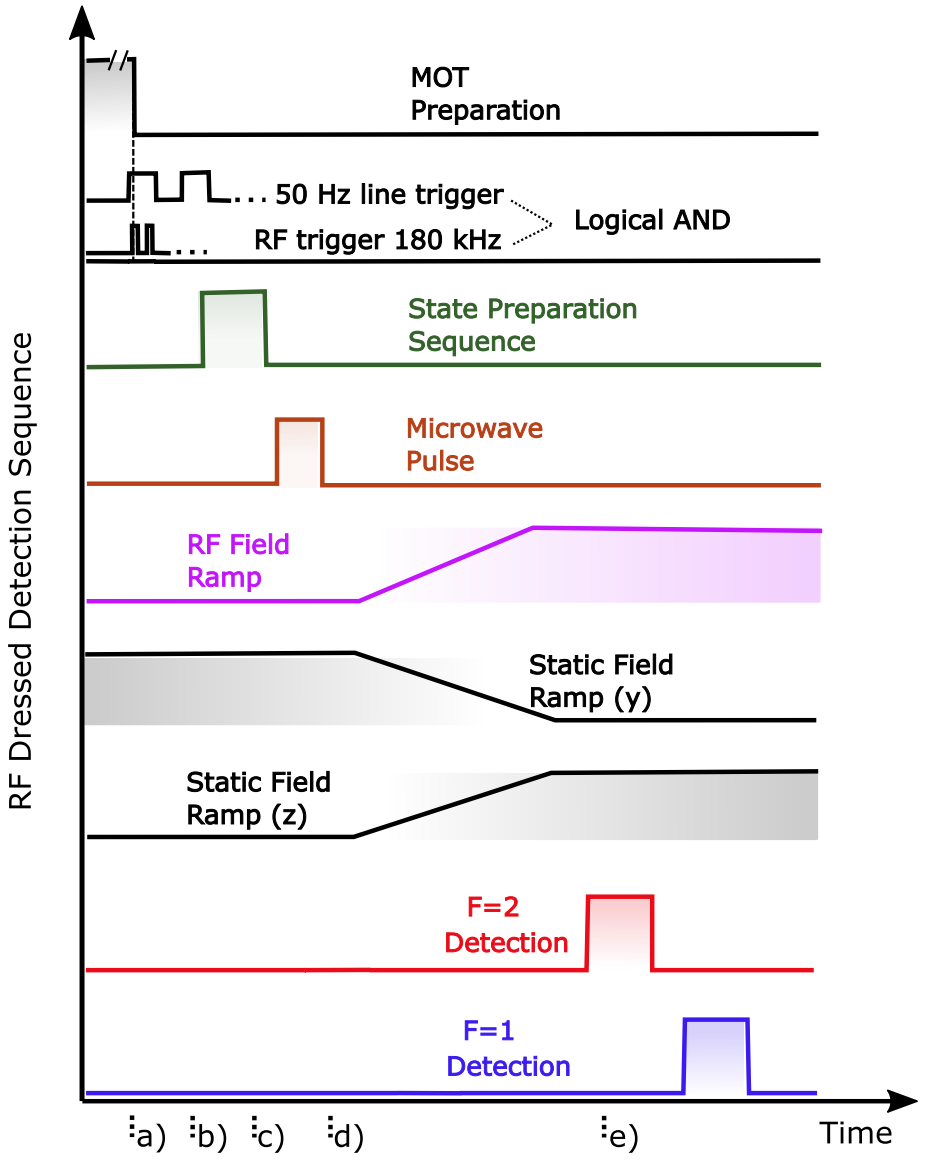


FIGURE 4.4: The figure gives the sequence of steps to perform RF dressed detection. A Logical AND operation (a) between the 50 Hz line and the RF field is used to trigger the end of the MOT preparation, setup to suppress 50 Hz electronic noise and ensure the detected signals are in phase with the RF field. The state preparation sequence (b) from Section 3.3 is used to prepare atoms in the $|F = 1, m = 0\rangle$ state which uses a static field of 430 mG in the y-direction. A MW pulse (c) of variable duration in a 5.5 kHz Rabi cycle is used to create a superposition of the two clock states. The atoms are adiabatically dressed with a 15 mG RF field over 3 ms (d) and the static field is ramped to 260 mG in the z-direction and reduced to 0 mG in the y-direction during the same time. The two Detection lasers are shone consecutively (e) to measure the populations in the two states.

the Armed Trigger stage. The PXI controller is then set to wait for a trigger from the function generator setting the RF field frequency (Figure 4.4a)) to release the MOT and continue with the rest of the sequence. This locks the phase of the

detected signals to the RF field and also to the 50 Hz electronics in the experiment thus reducing the noise in averaging signals from repeated experimental runs. The atomic signals collected are discussed in Section 4.3 and this sequence is followed for the typical experimental signals seen in Figure 4.7.

4.3 Experimental signals from dressed states

This section describes the typical experimental signals we collect and the analysis required. Section 4.3.1 shows the Log Power spectrum of atomic signals from a sample measurement. The incorporation of two state detection into the dressed detection scheme is shown in Section 4.3.2 and the dependence of signal strength on experimental parameters is discussed in Section 4.3.3.

4.3.1 Sideband detection

This section shows the detection of signals on an RF sideband. As explained in Section 4.1, we see atomic signals at ω_{RF} and $2\omega_{RF}$ frequencies, where ω_{RF} = 180 kHz in the experiment. The magnitudes of these signals are given by Equations 4.23 and 4.24 for the two experimental settings described there. Figure 4.5 gives the single-sided, spectral log power density of the experimental signals showing atomic signals at these frequencies.

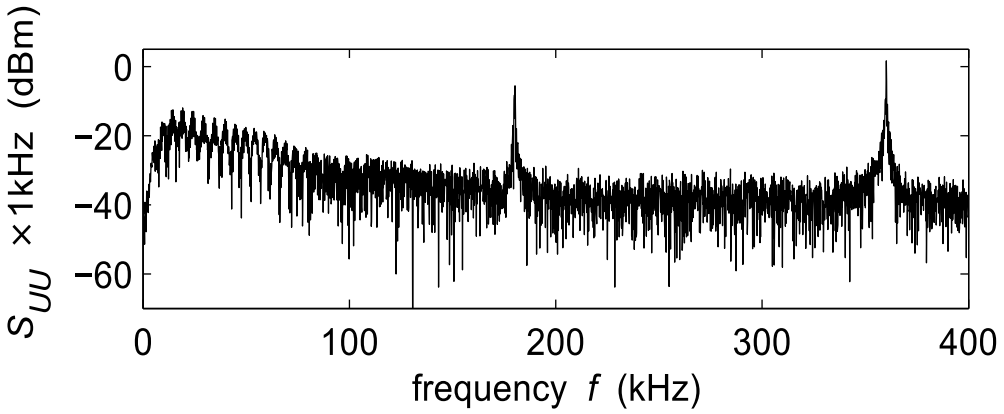


FIGURE 4.5: The figure shows the Spectral Log Power Density S_{UU} of the atomic signal U(t) collected by the balanced photodiode to illustrate detection of atomic signals on an RF sideband. A sample measurement from atoms in the $|F = 2\rangle$ state is shown here. The atomic signals arise at ω_{RF} = 180 kHz and $2\omega_{RF}$ = 360 kHz frequencies, with the experiment in the parallel setting, as described with Equation 4.23.

The signals are amplified and filtered through a high-pass filter before collection through the National Instruments PXI system as discussed in Section 4.2.1. The

raw signals are read into a computer and processed via digital lock-in detection. The lower frequency signals stem from the DC part of the transient pulses. We see that the atomic signals arise at 180 kHz and 360 kHz above the white noise floor, limited by photon shot noise at high frequencies (f ≥ 150 kHz).

4.3.2 Two State Dressed Detection

This section discusses the experimental signals U(t) collected on the balanced photodiode. For the atomic signal strength to be maximum, it is essential for the RF coupling of the hyperfine levels to be optimal, i.e. the static field B_{DC} has to be at resonance, B_{res} given by Equation 4.7. Figure 4.6 is given as an example of the detected RF signals as the static field is scanned across resonance. The atomic signals are usually measured near B_{res} as shown in Figure 4.7.

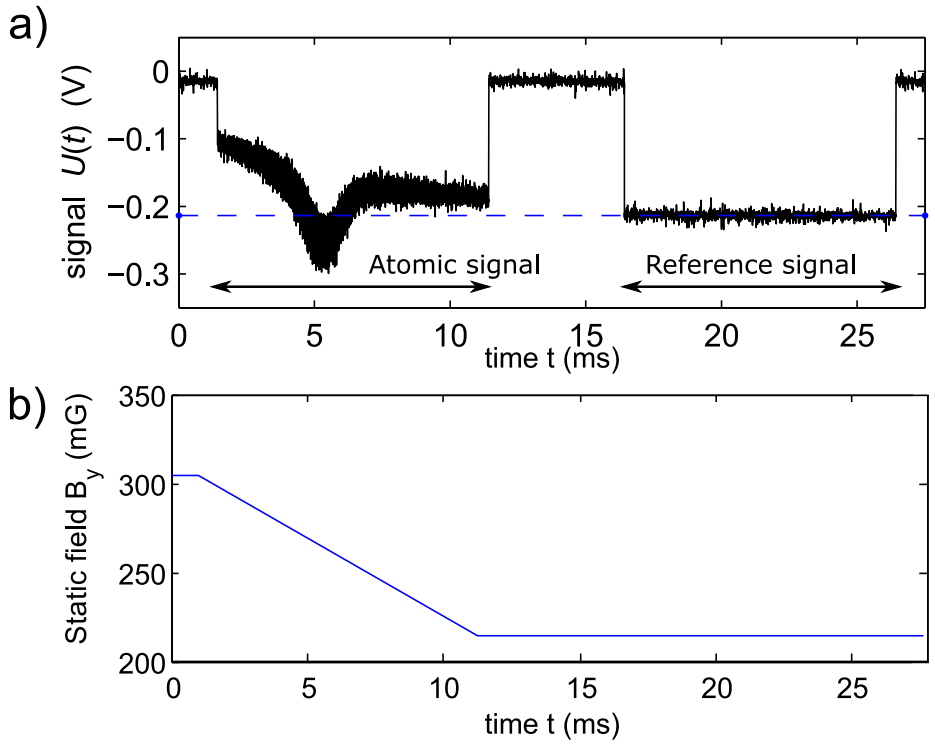


FIGURE 4.6: The figure shows the dressed signals U(t) on the photodiode in panel a) from atoms in the $|F = 2\rangle$ state with a linear scan of the static magnetic field across resonance. The experiment is conducted in the orthogonal setting with B_y scanned from 305 mG to 215 mG during the 10 ms detection period as shown in panel b), where $B_{res} \approx 260$ mG. A reference pulse of the detection beam is taken to mark the offset from 0 V due to experimental conditions.

The detected signals in Figure 4.6 follow the theoretical model for signals collected in the orthogonal setting of the experiment as given by Equation 4.24. An exponential decay of the signals is seen due to spontaneous emission induced by the probe beam in the atoms.

Figure 4.7 gives the typical experimental signals we see and the extraction of the signal strengths from the data. Two state detection is incorporated into this scheme to remove the effects of atom number fluctuations. The sequence followed for this measurement is described in Section 4.2.2.

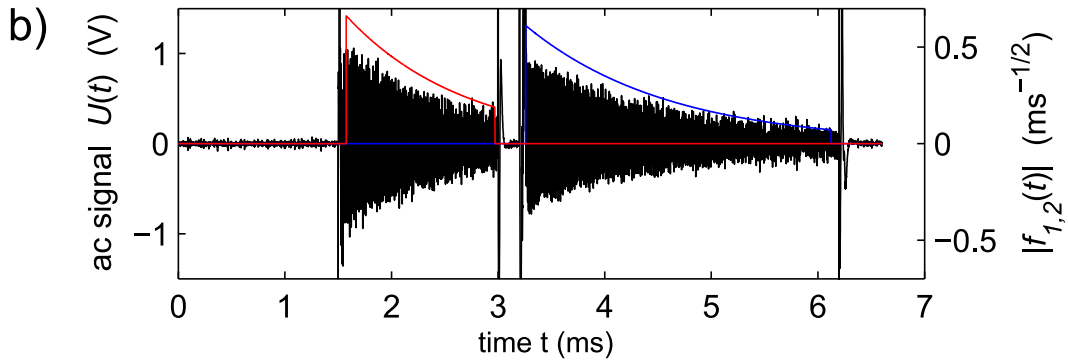


FIGURE 4.7: The figure shows the dressed signals U(t) on the photodiode from the two states, the first pulse from the $|F = 2\rangle$ state and the second from the $|F = 1\rangle$ state. The experiment is conducted in the parallel setting and the static field B_z is ramped to resonance 260 mG before the detection. The blue and red functions are mode amplitudes $\tilde{u}(t)$ extracted from the ac signals U(t) as shown in Equation 4.25. More details of the measurements and analysis are given in the text.

The atomic state with 10^8 atoms is in a superposition of the two states $|F, m\rangle$: $|1, 0\rangle$ and $|2, 0\rangle$ depending on the duration of the MW pulse in the sequence from Figure 4.4. The two detection lasers are shone consecutively to extract the atomic signals from both the states. As can be seen in the figure, the atomic signals decay due to spontaneous emission induced by the probe beams. We obtain signal values proportional to state populations by extracting spectral mode amplitudes $m_{1,2} = \int u^*_{1,2}(t)U(t)dt$ from the RF signal $U(t)$ with L^2-normalized temporal mode functions $u_{1,2}(t) = \tilde{u}(t)e^{2i(\omega t \pm \varphi)}$. In the case of square laser pulses of duration T,

their envelopes take the form

$$\tilde{u}(t) = \begin{cases} \sqrt{\frac{2\gamma}{1-e^{-2\gamma T}}} e^{-\gamma t}, & \text{if } 0 \leq t \leq T \\ 0, & \text{otherwise} \end{cases} \tag{4.25}$$

as shown in Figure 4.7, where γ are the experimentally determined decay rates dependent on the probe powers for the two states.

The decays of the two states are proportional to not only the detection pulse intensities but also the Clebsch-Gordon coefficients coupling the two transitions. We arrive at real signals by correcting each mode amplitude for an experimentally determined constant phase $\varphi_{1,2}$, which includes effects from the geometry and choice of polarization, as in Equations 4.24 and 4.23, as well as phases introduced by the detection electronics. Finally, values for individual measurements of the state transfer probability are obtained as $\sigma_z = (n_2 - n_1)/(n_2 + n_1)$, where we estimate state populations $n_{1,2}$ from the mode amplitudes using experimentally determined gains $g_{1,2}$ such that $n_{1,2} = g_{1,2}^{-1} m_{1,2}(2\omega)$. These are calibrated against atom number estimates from absorption imaging data. The gains $g_{1,2} = g'_{1,2} P_{1,2}$ account for simultaneously measured light powers $P_{1,2}$ and the combined effects of interaction strengths and electronic gain.

4.3.3 Signal strength with Field Detuning

This section discusses the dependence of the signal strength with static field magnitude across resonance. The dependence of the signal strength on the angle of the effective magnetic field is given in Equation 4.23 for the experiment in the parallel setting, where the directions of the different magnetic fields are as shown in Figure 4.2. The angle of $\mathbf{B}_{\text{eff}}$ seen by the atoms changes with the magnitude of the static field $\mathbf{B}_{DC}$. The strength is maximal when the angle is 90°, i.e. when the RF coupling between the $|F = 1\rangle$ and $|F = 2\rangle$ levels is maximum. The peak of the signal occurs at the static field magnitude where the RF coupling is maximal and the FWHM of the resonance depends on the strength of the RF field. The

signal dependence on the field detuning for the two hyperfine manifolds is shown in Figure 4.8, calculated for an RF field amplitude of 15 mG that we use in our experiment.

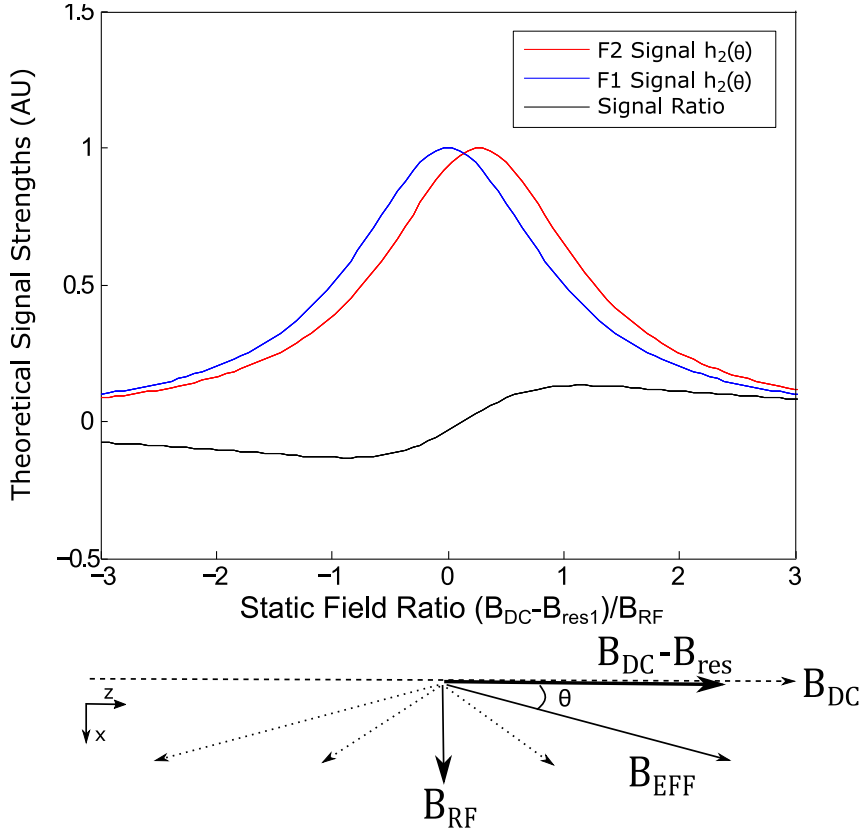


FIGURE 4.8: The figure shows the dependence of the theoretical signal strength following the $h_2(\theta)$ model in Equation 4.23 with static field ratio using B_{res} for $|F = 1\rangle$. θ is the angle between $\mathbf{B}_{\text{eff}}$ and B_{DC} as shown in panel b). It should be noted that as $\mathbf{B}_{\text{res}}$ is not the same for both the sub-manifolds (details in the text), the directions of their $\mathbf{B}_{\text{eff}}$s will be slightly different.

In order to measure atomic populations with high signal-to-noise ratio it is desirable to measure the corresponding mode amplitudes at $2\omega_{RF}$ in the parallel setting exactly on RF resonance. Here, the signals are maximal and exhibit only a second order dependence on the static magnetic field, which should reduce noise from external field fluctuations.

However, even in the regime of vanishing second order Zeeman splitting at low magnetic fields, the hyperfine interaction leads to a first order difference of Larmor frequency between the two hyperfine manifolds. The two corresponding g-factors differ in magnitude by $\Delta|g_F| = 2|g_I|$, where g_I is the negative nuclear g-factor. For

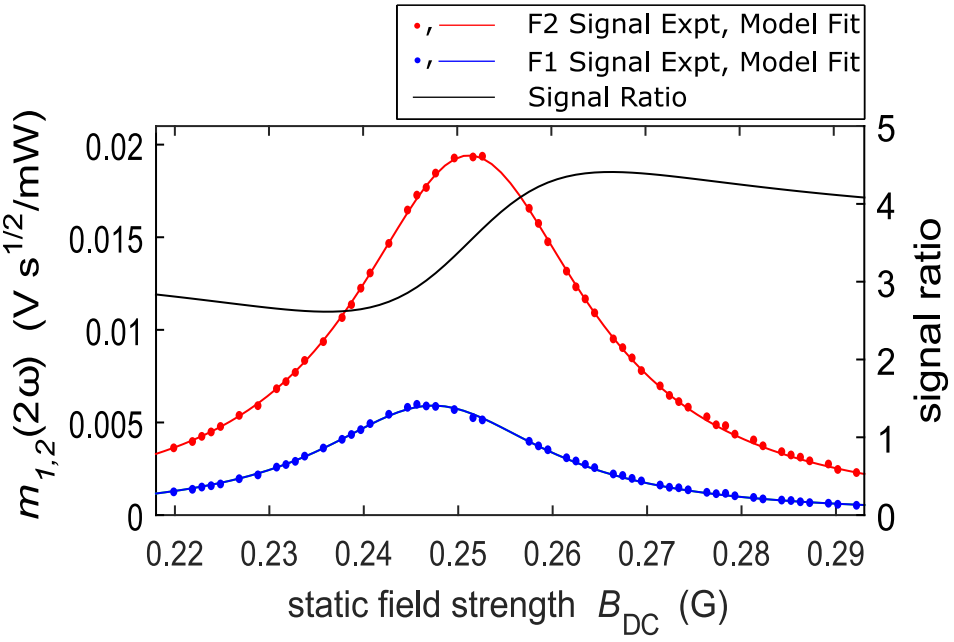


FIGURE 4.9: The figure shows experimental data of the signal strengths (mode amplitudes $m_{1,2}$ extracted as shown in Figure 4.7) with control magnetic field $\mathbf{B}_{\mathrm{DC}}$; when $\mathbf{B}_{\mathrm{RF}}$ = 15 mG. The positions and widths of the resonances are extracted from the model fits following Equation 4.23; as $m = a\sin^2(\pi/2 - a\tan((B-c)/(r/2))$ with $a = 0.005 \pm 0.001, c = 0.1248 \pm 0.0005$ and $r = 0.0146 \pm 0.001$ for the $|F = 1\rangle$ state and $a = 0.0179 \pm 0.001, c = 0.1268 \pm 0.0005$ and $r = 0.015 \pm 0.001$ for the $|F = 2\rangle$ state.

^{87}Rb this corresponds to a frequency difference of $2g_I\mu_B/h = 2.78565$ kHz/G. This is evident in the figure as a slight difference in the static field magnitude (≈ 0.004 G) where the two signals peak.

Figure 4.9 shows experimental data of a scan across the static field RF resonance in the parallel setting together with model fits according to Equation 4.23 for comparison with the theoretical signals shown in Figure 4.8. Each data point is the experimental signal from the two states at a particular magnetic field, i.e. at a particular angle of B_{eff}.

The difference in the amplitudes of the signals from the two hyperfine manifolds is due to the normalization of the signal strengths extracted with the respective laser beam intensities (≈ 0.4 mW for the F2 Detection laser and ≈ 1.1 mW for the F1 Detection laser, more details given in Section 4.3.2). As expected, the main contribution to the RF signal is found at frequency $2\omega_{RF}$. Due to a small

geometric misalignment, we also detect signals at frequency ω. The fit of model functions allows us to extract position and width of the resonances, which we use to calibrate the strength of the applied static field as well as the RF field amplitudes. The latter were measured to be $|B_+| = (15 \pm 1\ \text{mG})$ and $|B_-| = (14 \pm 1\ \text{mG})$. The small amplitude difference is attributed to stray RF fields from induced eddy currents that make the field polarization slightly elliptic at the location of the atomic ensemble. The static field at which the resonances occur extracted from this measurement are used in experiments described later for maximal signal strengths.

4.4 Rabi Cycles with RF dressed detection

With the measurement of populations in both the clock states $|F, m\rangle : |1, 0\rangle$ and $|2, 0\rangle$, we can detect Rabi cycles independent of atom number fluctuations in the MOT. The measurement of driven Rabi cycles in our experiment with this technique are shown in Figure 4.10 and can be compared to Figure 3.17 to see the improvement in detection with RF modulation.

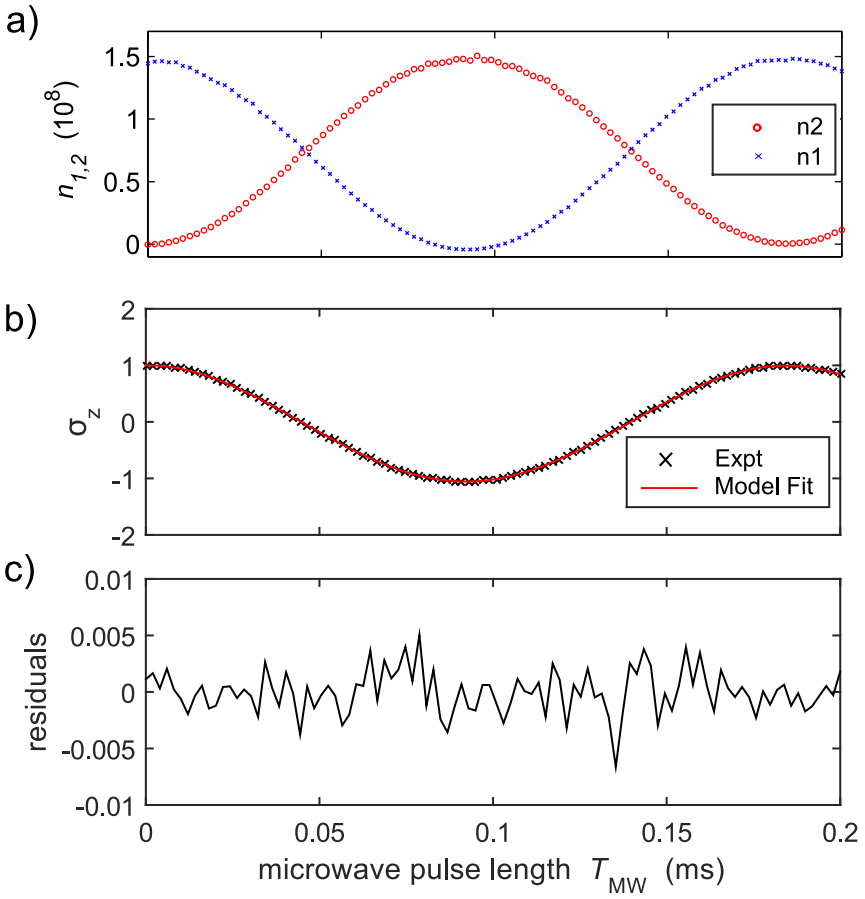


FIGURE 4.10: The figure shows population signals with RF Dressed detection from individual clock states in panel a) with varied MW pulse durations inducing a 5.5 kHz Rabi cycle between the two states and a measurement resolution of 0.002 ms. The signals are normalized to atom numbers calibrated by Absorption Imaging beforehand. Panel b) gives the state transfer probability σ_z calculated and its model fit as $\sigma_z = a\cos(\omega t + b)e^{-idt} + c$ with $a = 1.028, \omega = 5.488$ kHz, $b = 0.0072, d = 0.0416, c = -0.04$.The residuals for these measurements are given in panel c).

To obtain signal values proportional to the state populations, we extract mode amplitudes $m_{1,2} = \int u^*_{1,2}(t)U(t)dt$ from the RF signal $U(t)$ as shown in Figure 4.7b)

with temporal (phase locked) mode functions $u(t)$ normalized to $\int u^2(t)dt = 1$. Each point in the data set is one experimental run with varied microwave driving times. Figure 4.10a) shows the signal strengths from the two states analyzed at the 2ω frequency sideband. The high contrast fringes of Rabi frequency Ω = 5.5kHz are modeled with an exponential decay to account for decoherence induced by various experimental conditions. The signals are normalized with the atom numbers calibrated by absorption imaging. Figure 4.10b) gives the state transfer probability $\sigma_z = (n_1 - n_2)/(n_1 + n_2)$ to show a Rabi cycle between 1 and -1. The data points (black crosses) are fitted to a cos function (red line). Figure 4.10c) shows the residuals of the fit, i.e. the difference between the amplitudes of the data points and the fits. The results of this technique show that the detection of atom number difference of the two states is precise to 0.2%.

4.5 State to Quadrature Mapping

Atomic state to light quadrature mapping is possible in our system as the phase dependence of the detected radio frequency signal on the RF field's angle is different for the two states, represented by the sign of the phase φ in Equations 4.22-4.24. The phase ϕ represents the orientation of the RF field with respect to the coordinate axes. Therefore, a rotation of the light polarization with respect to the atomic coordinate system is equivalent to a rotation of RF field.

Figure 4.11 shows experimental data and a model fit of the RF phase of the $2\omega_{RF}$ signals with angle of light polarization. The angle of the input light polarization is changed by rotating the half wave plate before the UHV chamber. Data is collected by populating one of the clock states and measuring the $2\omega_{RF}$ signal with different angles of the half wave plate through the whole 360°.

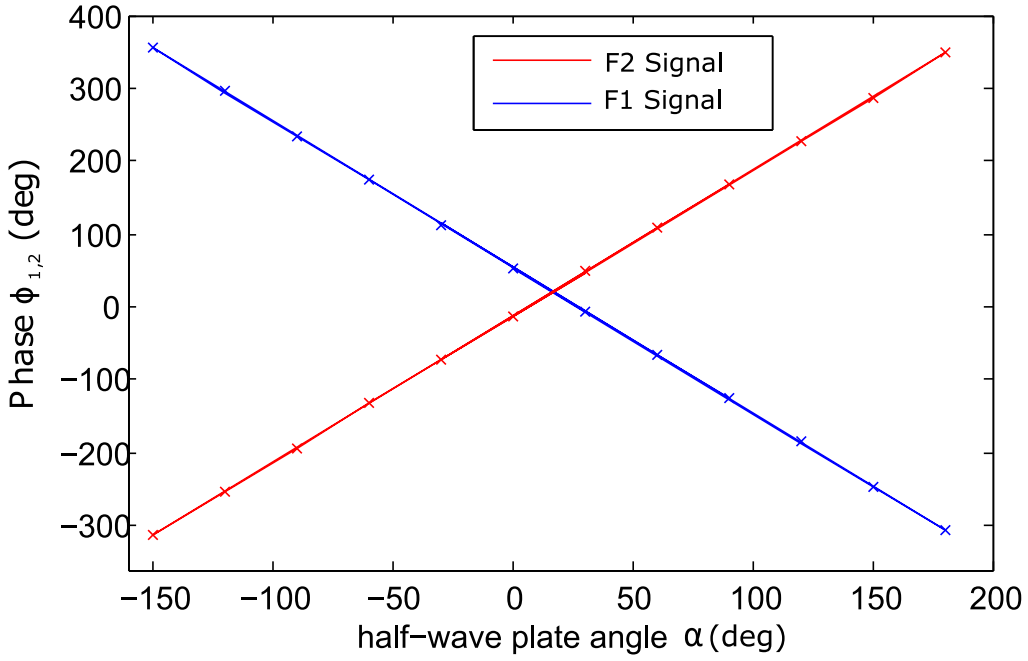


FIGURE 4.11: The figure shows experimental data and model fits (given in the text) for the signal phase dependence on input light polarization angle. The light polarization angle is changed by rotating the half wave plate in the detection scheme given in Figure 4.2. The offset in the model fits is attributed to a misalignment between the half wave plate axis and the RF field axis.

The experiment is conducted in the parallel setting of RF detection. The two manifolds have opposite directions of rotation with the RF field determined by the signs of their g_F factors. The linear fits of the data are given by the following equations:

$$\phi_{F=1} = -4.00\alpha + 15 \tag{4.26}$$
$$\phi_{F=2} = 3.98\alpha - 15$$

where x is the angle of the half-wave plate in degrees.

The fits have slopes of $\pm(3.99 \pm 0.01)$ matching the expected values of ± 4. The slopes have a factor 2 contribution from the fact that the signals oscillate at twice the frequency of the RF field and another factor 2 contribution from the circular analysis of the signals with a quarter-wave plate, as seen by the dependence of the h_2 component of the signal on the angle ϕ in Equation 4.23 where $\phi = 2\alpha$. The ± 15 degree offset is due to the misalignment between the RF field axis and the axis of the half wave plate set on the optical table.

From Figure 4.11, it can be seen that there are two angles of the light polarization where the phases of the signals from the two states differ by 90°. At these points, it is possible to map the two atomic levels onto light quadratures independently thus ensuring state to quadrature mapping.

Chapter 5

Noise Analysis

This chapter discusses the noise performance of the experiment over the following five sections. Section 5.1 revises the quantum limit of detecting atoms. Section 5.2 explains how we calculate the noise performance of the experiment and gives a model for it with the analysis of each source of noise in particular discussed in Section 5.3. The techniques that are used to reduce the technical noises in the experiment are given in Section 5.4 and setup improvements that are expected to realize quantum noise level detection are discussed in Section 5.5.

5.1 Standard Quantum Limit

The interaction between light and atoms enables high-precision measurements of fundamental physical quantities. All measurements are limited by the Heisenberg Uncertainty Relation $(\Delta x)(\Delta p) \geq \hbar/2$ between the quadrature measured and its conjugate variable following the commutator relation.

For an atomic ensemble system prepared in a spin state in the x-axis, the Heisenberg uncertainty relation for measuring the atomic state superposition, i.e. measuring the spin components of the ensemble is given by

$$\Delta J_z . \Delta J_y \geq \langle J_x \rangle / 4 \tag{5.1}$$

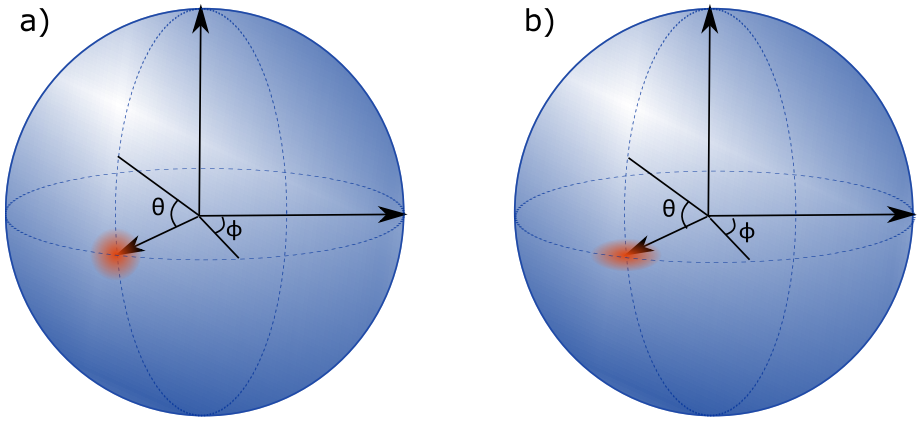


FIGURE 5.1: The figure illustrates Projection Noise for a Coherent Spin State (CSS) in panel a) with noise at the standard quantum limit; and for a Spin Squeezed State (SSS) in b) with noise in one component below the standard quantum limit.

The uncertainty in these measurements is least, i.e. the equality in the Heisenberg relation holds when the atomic ensemble is in a Coherent Spin State (CSS) (shown in Figure 5.1). The atoms are in a coherent superposition of the two states and the ensemble wavefunction can be written as

$$|\Psi\rangle = \left[\frac{|\uparrow\rangle + |\downarrow\rangle}{\sqrt{2}}\right]^{\otimes N_A}, \tag{5.2}$$

with $\langle J_x\rangle = \hbar/2N_A$. This state is discussed in Section 2.1, its spin expectation values and variances given by Equation 2.7 and Equation 2.8 respectively. The uncertainty in determining the atomic state, in other words, the projection noise of the spin state is characterized by a Binomial distribution of probability and can be expressed in terms of the angle uncertainties

$$\Delta\theta = \Delta\Phi = \frac{\Delta J_{z/y}}{\langle J_x\rangle} = \frac{1}{\sqrt{N}} \tag{5.3}$$

which is called the atomic shot noise limit.

In principle, a reduction in the measurement uncertainty is possible with the generation of the non-classical Spin Squeezed States (SSS) shown in Figure 5.1. This

does not violate the Heisenberg uncertainty relation as the reduction in one quadrature's uncertainty, say $\Delta\theta$, is accompanied by an increase in $\Delta\phi$ thereby keeping their product above the limit set by Equation 5.1. The atomic projection noise in such a state can be lower than the noise of a coherent spin state.

The uncertainty in measurement can be expressed as

$$\Delta\theta = \frac{\epsilon_{SS}}{\sqrt{N}} \tag{5.4}$$

where ϵ_{SS} is called the spin squeezing factor.

The generation of such states experimentally is possible with an off-resonant QND method of detecting atoms with coherent light beams, such as our technique of detecting the state transfer probability. The spin squeezed state can then be used in further experiments for precision measurements.

Identifying and reducing the different sources of noise seen in the experiment is a step towards achieving atomic shot noise limited detection and using the technique to produce spin squeezed atoms in the future.

5.2 Performance of the system

This section discusses the current noise performance of the experiment. The atomic ensemble is prepared in a 50 : 50 superposition of the two clock states $|F, m\rangle$: $|1, 0\rangle$ and $|2, 0\rangle$. Repeated measurements of the populations of the two states are conducted with the RF dressed detection technique as shown in Section 4.3.2 to determine the variance of the state transfer probability $\sigma_z = (n_1 - n_2)/(n_1 + n_2)$. To measure the noise scaling with atom number in the ensemble, the variance of the state transfer probability is determined for different atom numbers by varying the MOT loading duration. The atom number in the MOT with loading duration is calibrated beforehand with absorption imaging.

Figure 5.2 gives the variance of state transfer probability σ_z for measured signals of the two states with the total atom number in the MOT. At atomic shot noise level, the variance should fall as $1/N_A$ with total atom number. These variances are used in further analysis to determine technical noise as shown in Figure 5.3.

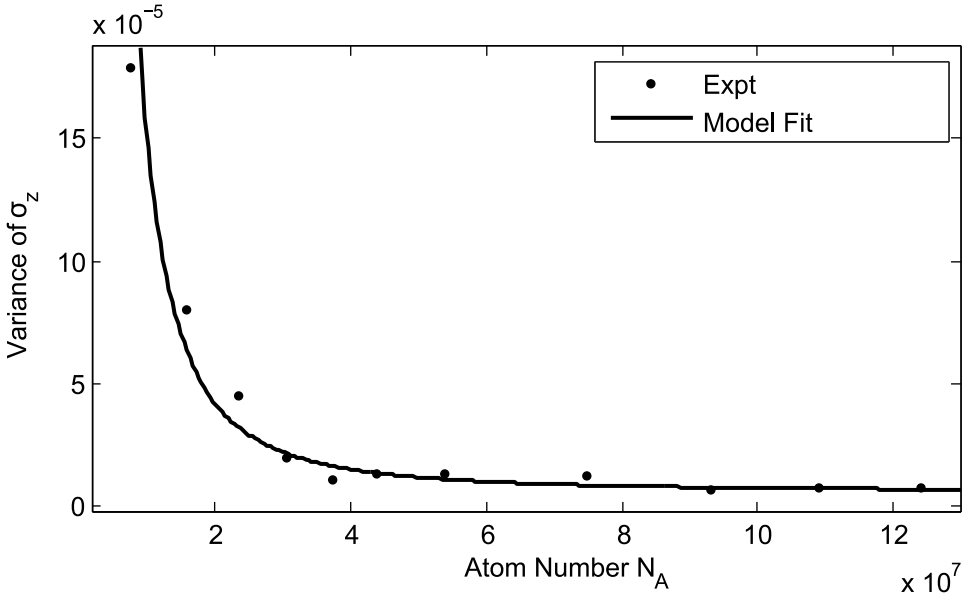


FIGURE 5.2: The figure shows variance of state transfer probability $\langle(\Delta\sigma_z)^2\rangle$ of population measurements in a 50 : 50 superposition of the clock states conducted at various MOT loading durations with 50 repetitions for each point. The model fit $\sigma_z^2 = aN_A^{-2} + c$ gives $\sigma_z^2 = (1.4 \pm 0.8) \times 10^{10} N_A^{-2} + (6 \pm 3) \times 10^{10}$.

This measurement can be translated to atom number equivalent noise by analyzing the variance of atom number difference as shown in Figure 5.3. The variance of atom number difference is obtained by taking the product of the variance of σ_z shown in Figure 5.2 with N_A^2.

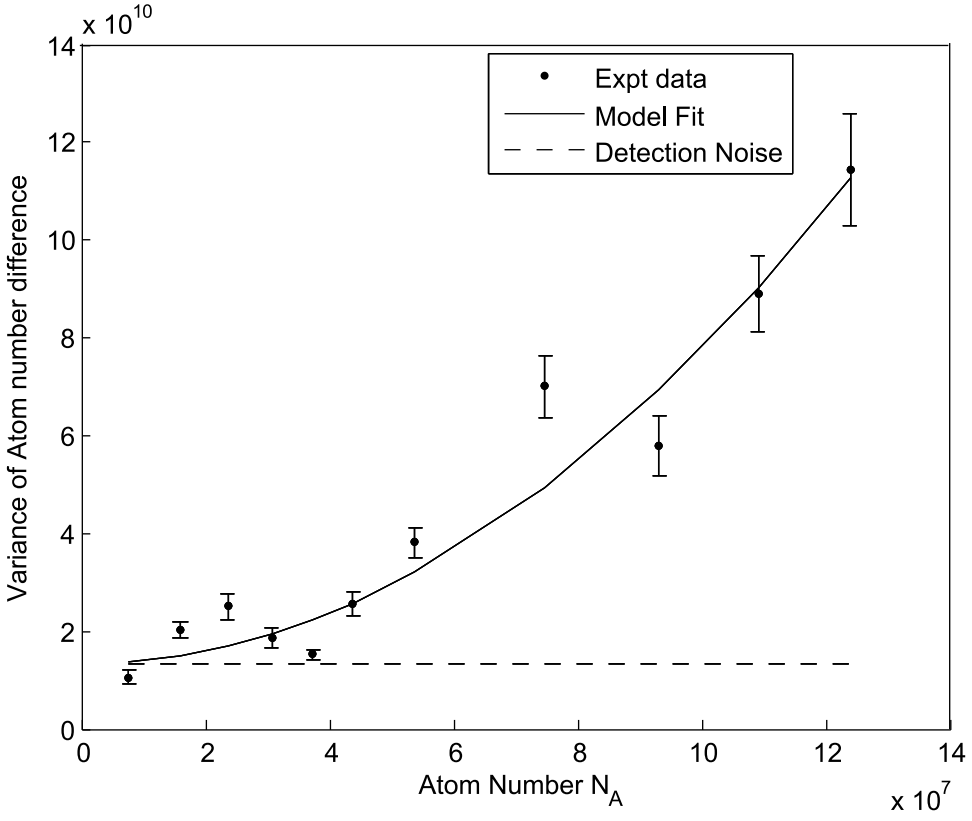


FIGURE 5.3: The figure shows noise scaling with atom number, where variance of atom number difference = $\langle(\Delta\sigma_z)^2\rangle \times N_A^2$ obtained from the measurement in Figure 5.2. The model fit $\langle(\Delta(N_1 - N_2))^2\rangle = a + b \times N_A^2 = 1.33 \times 10^{10} + 6.47 \times 10^{-6} \times N_A^2$ is weighted according to the standard deviation (error bars) of the measurements.

The model fit in Figure 5.3 is used to determine the technical and detection noise in the experiment. The offset 1.33×10^{10} in the fit represents the detection noise and the quadratic factor 6.47×10^{-6} represent the technical noise. The detection noise limited atom number resolution is $\sqrt{1.33 \times 10^{10}} \approx 1.15 \times 10^5$ and the technical noise is $\sqrt{6.47 \times 10^{-6}} \approx 0.25\%$. At 10^8 atoms in the MOT, the atomic shot noise limit would be 0.01%. From the ratio of the technical noise and the atomic shot

noise limit, it can be said that the experiment is 28 dB above the atomic shot noise limit for 10^8 atoms.

5.3 Analysis of noise sources

This section isolates the different noise sources in our system and analyzes their contribution to the total noise performance. The isolation of noise sources is essential for designing improvements to the system and reach the quantum noise limit. Section 5.3.1, Section 5.3.2 and Section 5.3.3 analyze the noise in the state preparation of the scheme, the photon shot noise and the electronic noise in our experiment respectively. Section 5.4 shows reduction of noise by varying the static field and Section 5.5 discusses possible schemes that can be implemented to reach the atomic shot noise limit.

5.3.1 State Preparation noise

Irrespective of the noise in the detection, the noise in the signals from the two states are also affected by the fluctuations of their atom numbers due to the noise in the microwave pulses. The state transfer probability is determined by the duration of the microwave pulses which induce Rabi cycles with a certain frequency. This Rabi frequency depends on the interaction strength between the atoms and the microwave field and can be given by

$$\Omega = -\frac{B_{MW}}{2\hbar}\left(\mu_B g_S - \mu_B g_I\right) \tag{5.5}$$

where B_{MW} is the magnetic field component of the Microwave field. Fluctuations in the intensity of the microwave pulses from the source leads to slight variations in the Rabi frequency which translates to noise in the state transfer probability even though the duration of the pulses is tightly controlled.

Figure 5.4 characterizes the noise in the state preparation process due to the MW field fluctuations with power ≈ 250 mW. The variances of the state transfer probabilities are measured at odd multiples of the $\pi/2$ pulse durations.

The technical noise inherent in the state preparation process can be extracted from the model fit in Figure 5.4. At 46 μs, which is the duration of the $\pi/2$ pulse used

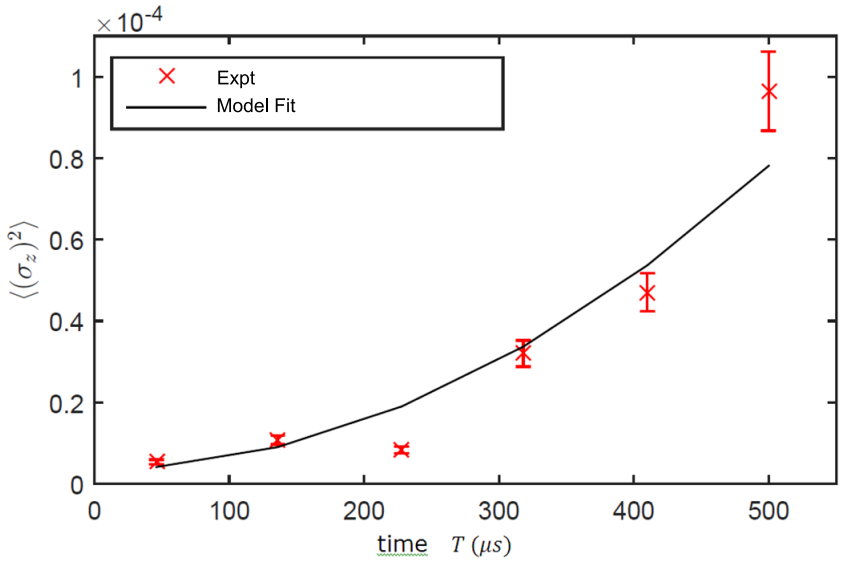


FIGURE 5.4: The figure shows the dependence of state preparation noise on MW pulse duration of power 250 mW inducing a 5.5 kHz Rabi cycle. The measurements are conducted with 10^8 atoms in the initial MOT at the first six consecutive 50:50 distribution points between the two states, i.e. odd multiples of the $\pi/2$ pulse. The variance of state transfer probability $\langle(\Delta\sigma_z)^2\rangle$ is plotted with MW pulse duration. The model fit $\langle(\Delta\sigma_z)^2\rangle = a \times \mu s^{-2}T^2 + b$ gives $\langle(\Delta\sigma_z)^2\rangle = 2.98 \times 10^{-10}\mu s^{-2}T^2 + 3.47 \times 10^{-6}$.

in all the experiments discussed here, the noise in the state transfer probability $\langle(\sigma_z)^2\rangle$ is calculated from the model fit to be 0.63×10^{-6} which is approximately 25% of the technical noise measured by analyzing the noise with atom number performance of the system at the same time.

5.3.2 Light Noise

The measurement of population difference in the two atomic states is affected by not only the uncertainties in the superposition state but also the uncertainties inherent in the light pulses themselves. The laser pulses can be considered as coherent monochromatic light fields. These pulses can be described quantum mechanically as a coherent state $|\alpha\rangle$ given by

$$|\alpha\rangle = \exp\left(-\frac{1}{2}|\alpha|^2\right)\sum_{n=0}^{\infty}\frac{\alpha^n}{\sqrt{n!}}|n\rangle \tag{5.6}$$

which is an eigenstate of the field annihilation operator $\hat{a}$ such that:

$$\hat{a}\,|\alpha\rangle = \alpha\,|\alpha\rangle \tag{5.7}$$

For these states, the first and second moments, i.e. the mean and standard deviation of the photon numbers in the pulses are given by

$$\begin{aligned}\langle\alpha|\hat{a}^\dagger\hat{a}|\alpha\rangle &= |\alpha|^2 = \bar{n}\\ \delta^2(\hat{a}^\dagger\hat{a}) &= \bar{n}\end{aligned} \tag{5.8}$$

Any measurement signal with these light fields is dependent on the number of photons in the pulse, i.e. the intensity of the beam and the accuracy of these measurements is fundamentally limited by the uncertainty of the photon number in the pulse. The measurement is light shot noise limited when its variance is linearly proportional to the mean number of photons.

The balanced detector pair (Thorlabs PDB210A) is photon shot noise limited, confirmed by the linear dependence of spectral noise power density of the RF signal S_{UU} on light power in absence of atoms, as shown in Figure 5.5. We use this shot noise scaling to calibrate the conversion gain of the detection $g_C = U/\Delta P$, defined as output voltage U per optical power difference ΔP incident on the two detectors.

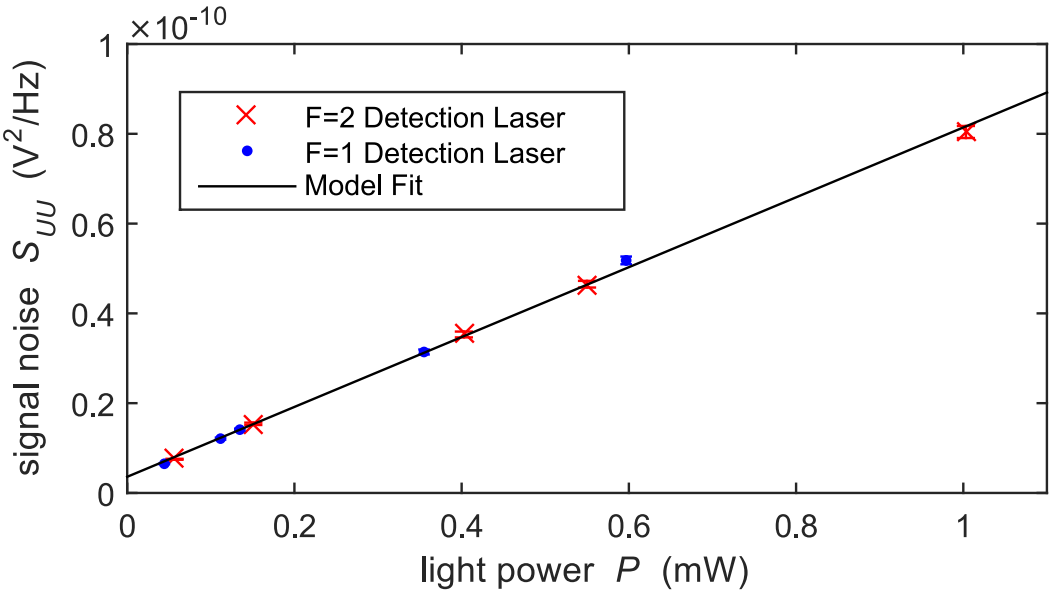


FIGURE 5.5: The figure shows the measured signal noise S_{UU} and errors with different light powers of the two lasers by taking 100 measurements for each data point. The model fit S_{UU} = a.P+b = $(7.83\pm0.05)\times10^{-11}.P+(3.69\pm0.05)\times10^{-12}$. This model fit can be used to calibrate the gain of the photodetector as shown in the text.

For coherent states of the input light field of power P_{in} and known detector efficiency $\eta < 1$, the conversion gain can be measured as $g_C = \sqrt{\eta\lambda S_{UU}/hcP_{in}}$. Detector efficiency relates to responsivity $r = I/P$, i.e. photocurrent I per incident optical power P, as $\eta = rhc/e\lambda$, resulting in $g_C = \sqrt{rS_{UU}/eP_{in}}$. We find $S_{UU}/P_{in} = 7.8 \times 10^{-8}$ V^2s/W and corresponding gain $g_C = 5.19 \times 10^5$ V/W for λ = 795nm and the values $r = 0.55$ A/W or $\eta = 0.86$ which are taken from the photodetector sheet.

5.3.3 50 Hz Noise and Influence of other external noise

The second order Zeeman splitting affects the Larmor frequencies of the two hyperfine manifolds as shown in Section 4.3, which translates to a difference in the static field magnitude at which their RF coupling is resonant. This affects the suppression of common mode noise when state transfer probabilities are derived from the individual populations. Figure 5.6a) gives the variance of the measured state transfer probabilities at different static field strengths across the RF resonance. Three experimental conditions are shown for comparison: presence of external low frequency static field noise (black); without external static field noise but in presence of 50 Hz noise from the AC mains supply (blue) and with AC triggering of the experimental sequence as discussed in Section 4.2.2 to get rid of 50 Hz noise (red).

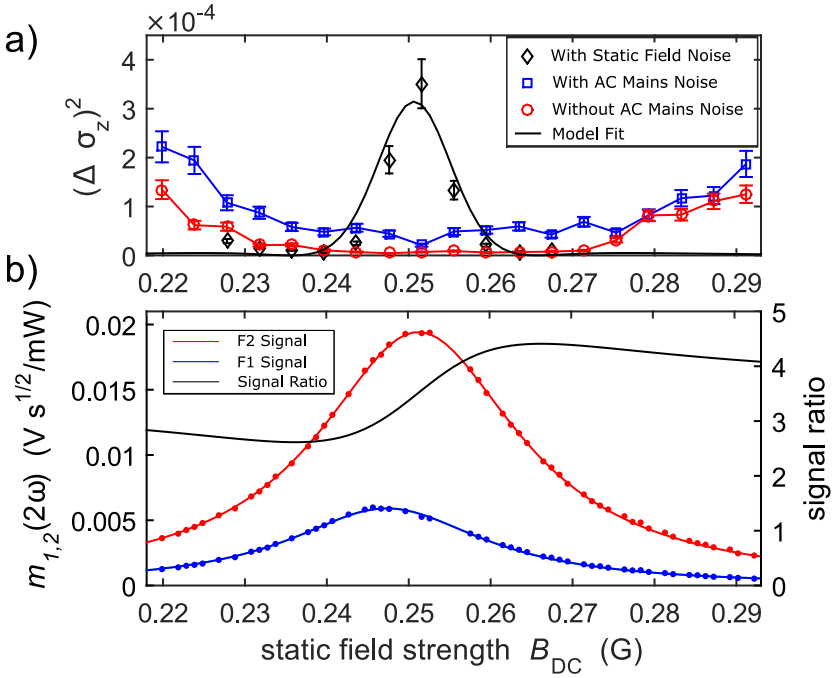


FIGURE 5.6: The figure shows the dependence of technical noise on static field in panel a) with 50 repetitions for each data point in three different experimental conditions. Panel b) gives signal strengths from the two clock states with static field as in Figure 4.9, repeated here for comparison with a). With external technical noise (black in a)), the variance of measurements is least when the ratio of signal strengths is extremal as discussed in the text, whereas without external noise (red and blue), the variance is least at static field resonance. The technical noise is least when we employ 50 Hz AC triggering (red) of the experimental sequence as shown in Section 4.2.2.

Common mode noise includes total atom number fluctuations as well as signal strength variations. While the suppression of noise due to external field fluctuations improves with the resonance width it is highest when the ratio of the two mode amplitudes as a function of external field is extremal or, equivalently, when the ratio of signal strength to signal slope is identical for the two states (which can seen in Figure 5.6b)). The parameter set that meets this condition depends on frequency shift and widths of both resonances. For equal resonance width, i.e. $|B_+| = |B_-| = |B_{\mathrm{RF}}|/\sqrt{2}$ and resonant field difference $\Delta_B = \hbar\omega/2g_I\mu_B$, the optimal static field is found shifted from the resonance mean by $\pm\frac{1}{2}\sqrt{|B_{\mathrm{RF}}|^2 + \Delta_B^2}$. As a consequence, the signal strength will be approximately half of the maximum when it is traded for maximal common mode noise suppression. This can, in fact, be improved by deliberately increasing the imbalance between the two $B_\pm$-components, which shifts the optimal point closer to maximum. As expected, the resulting variance when there is external noise becomes minimal near the stationary point that is closest to maximum. Without the external noise, the difference between the noise amplitudes with and without AC triggering is evident and the noises are minimum close to the resonances of the two manifolds.

5.4 Noise Reduction with detection at different fields

This section looks into various methods of noise reduction possible with the current experimental setup. The analysis of the different sources of technical noise in the experiment helps to determine the problems to be addressed before reaching the quantum noise limit.

5.4.1 Dependence of state transfer probability with static field

We try to reduce technical noise due to field fluctuations by looking at the behaviour of the state transfer probability variance with static field shown in Figure 5.6 and choosing an optimal field magnitude. As explained in Section 5.3.3, the effect of technical noise in the experiment is lowest when the ratio of signal strength to signal slope is identical for the two states. This optimal field can be determined from Figure 4.9 where the ratio of signal strengths is extremal. The experimentally measured noise at this field insensitive point is given in Figure 5.7. The measurement in Figure 5.3 with the static field at B_{res} for the $|F = 2\rangle$ level is shown here again for comparison.

The analysis of the variances determines the dependence of detection noise and technical noise with static field. The measurement with near maximal signal strength (at B_{res} for the $|F = 2\rangle$ level) yields a detection noise limited atom number resolution of 1.15×10^5 and technical noise of 0.25%, which is 28 dB above the atomic shot noise limit. At the optimal detuning (the field insensitive point), the reduced signal strength of the two states increases the detection noise to $\sqrt{3.84 \times 10^{10}} \approx 1.96 \times 10^5$. The technical noise in this case reduces to $\sqrt{4.47 \times 10^{-6}} \approx 0.21\%$ which is 26 dB away from the atomic shot noise limit of 0.01% for measurements with 10^8 atoms.

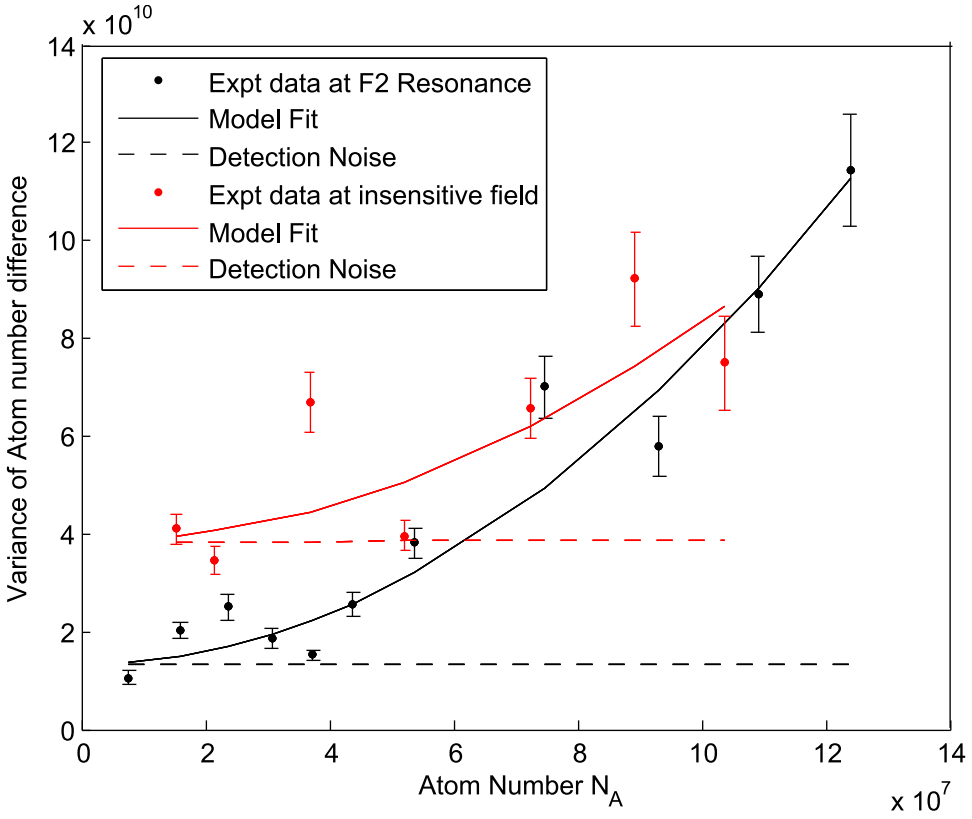


FIGURE 5.7: The figure gives the comparison of Noise Performance with atom number taken at B_{res} for the $|F = 2\rangle$ level (black, repeat of Figure 5.3) and the field insensitive point (red). The measurements are conducted with 10^8 atoms with 50 repetitions for each data point. The model fit for the measurement at B_{res} is given by $\langle(\Delta(N_1 - N_2))^2\rangle = 1.33 \times 10^{10} + 6.47 \times 10^{-6} \times N_A^2$ whereas that for the measurement at the field insensitive point is given by $\langle(\Delta(N_1 - N_2))^2\rangle = 3.84 \times 10^{10} + 4.47 \times 10^{-6} \times N_A^2$.

5.4.2 Detection of two states with static field shift

To get the best noise performance with the current setup, we ramp the static field between the two detection pulses such that both the states are detected at their respective resonance fields, i.e. both the $|F = 2\rangle$ levels and the $|F = 1\rangle$ levels are fully coupled at the time of their detection. The noise performance of such a measurement is compared to the noise performance without the field shift in Figure 5.8. As the difference between the two field resonances is only ≈ 0.004 G, this field ramp takes less than 0.5 ms, and the atoms in the second detected state still remain mode matched to their detection beam.

The measurement at resonance of one state gives detection noise $\sqrt{1.73 \times 10^{10}} \approx$

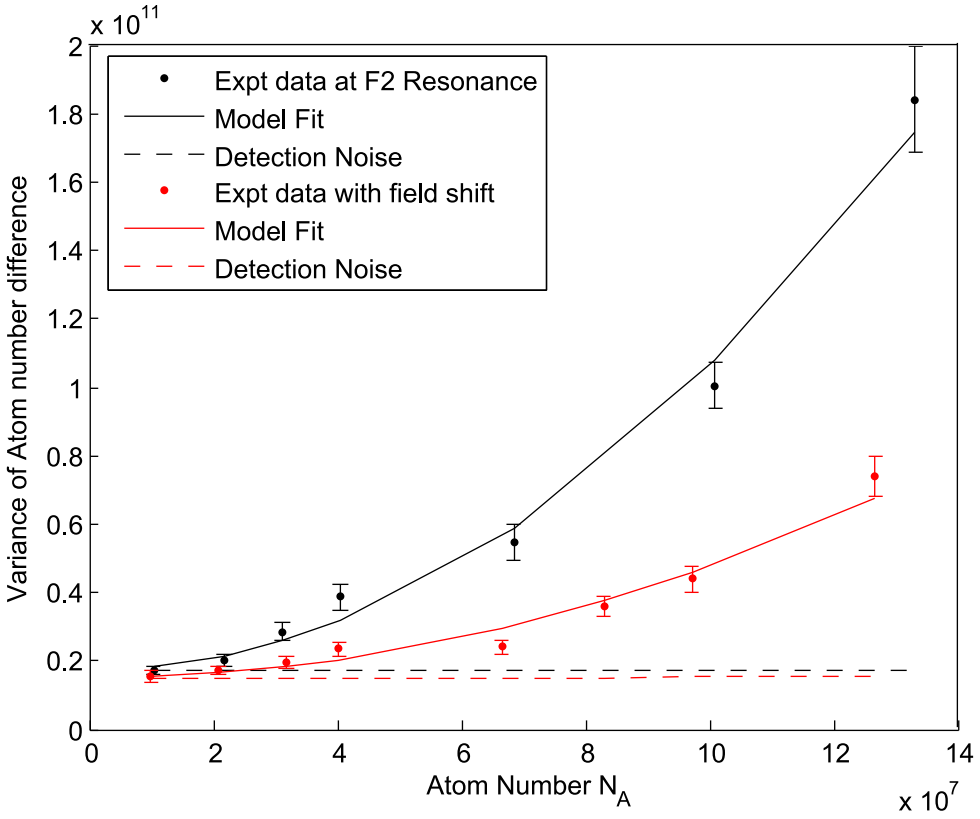


FIGURE 5.8: The figure shows comparison of Noise Performance with atom number at the static field resonance point B_{res} for the $|F = 2\rangle$ level (black) and at resonance for both the states (red) achieved with a field ramp between the two detection pulses. Each data point is taken with 50 repetitions. The model fit for noise at B_{res} is given by $\langle(\Delta(N_1 - N_2))^2\rangle = 1.73 \times 10^{10} + 8.86 \times 10^{-6} \times N_A^2$ whereas that for noise measured with the field ramp is $\langle(\Delta(N_1 - N_2))^2\rangle = 1.51 \times 10^{10} + 3.26 \times 10^{-6} \times N_A^2$.

1.31×10^5 and technical noise of $\sqrt{8.86 \times 10^{-6}} \approx 0.29\%$. This particular measurement is conducted in the same scenario as that discussed in Section 5.2 and is taken again for the best comparison with the second scenario. Indeed the technical noise is slightly different, attributed to influence of external noises on our experiment. Detection of both the states at maximal signal strength leads to a slight reduction in detection noise ($\sqrt{1.51 \times 10^{10}} \approx 1.23 \times 10^5$) in the measurement with field shift. The technical noise is reduced to $\sqrt{3.26 \times 10^{-6}} \approx 0.18\%$, i.e. 62% of the previous value. The measurement here is 25 dB above the atomic shot noise limit for 10^8 atoms.

5.5 Outlook - Towards detection of atoms at the quantum limit

Achieving QND measurements at the atomic shot noise limit is one of the methods used to realize spin squeezed states as discussed in Section 5.1. The standard deviation of measurements at the quantum limit follows the trend $1/\sqrt{N_A}$ with atom number. With the current noise performance given in Section 5.4, both detection noise of the atoms as well as technical noise in the experiment have to be decreased to be able to detect atoms at the projection noise limit. The noise due to our state preparation scheme can be decreased as shown in Section 5.4. The technical noise in the current detection scheme can be suppressed by using the same laser to detect both the states simultaneously. This enables direct subtraction of the two signals eliminating noise due to separate analysis for the two states. However, detecting both the states with the same laser simultaneously is also possible with the principle of state to quadrature mapping shown in Section 4.5. The implementation of the technique is shown in Section 5.5.1. The possibility of reducing the detection noise level of the atoms using a cavity around the chamber is discussed in Section 5.5.2.

5.5.1 Simultaneous Detection of the two clock states

Detecting the two states consecutively in the same experimental cycle allows us to get rid of the noise induced by atom number fluctuations in the MOT formation stage as shown in Section 3.6. Being able to detect the two states truly simultaneously would help circumvent the external technical noise affecting the experiment. Performing simultaneous detection of the two states with the same laser would also reduce the noise in detection due to relative laser intensity fluctuations and frequency fluctuations. Simultaneous detection is usually difficult as the intensities of the two detection light fields cannot be separated on the photodetector. But it is possible with state to quadrature mapping by encoding the signals from

the two states in the two quadratures of the detection light beam and separating them later.

As explained in Section 4.5, the phase of the detected radio-frequency signal is state-dependent, represented by the sign of the phase φ. In order to encode signals from both the states into the same pulse of light, its input polarization is adjusted such that the two signals exhibit a phase difference of 90° which encodes the two signals in orthogonal quadratures of the light pulse. Thus, the two signals do not affect each other. The signals from the pulse can be analyzed and the real and imaginary parts of the signals separated. The situation is demonstrated in Figure 5.9, which shows the experimental data for a particular point in a Rabi cycle, taken with the two detection laser pulses shone at the same time and the separation of the population signals from the two states.

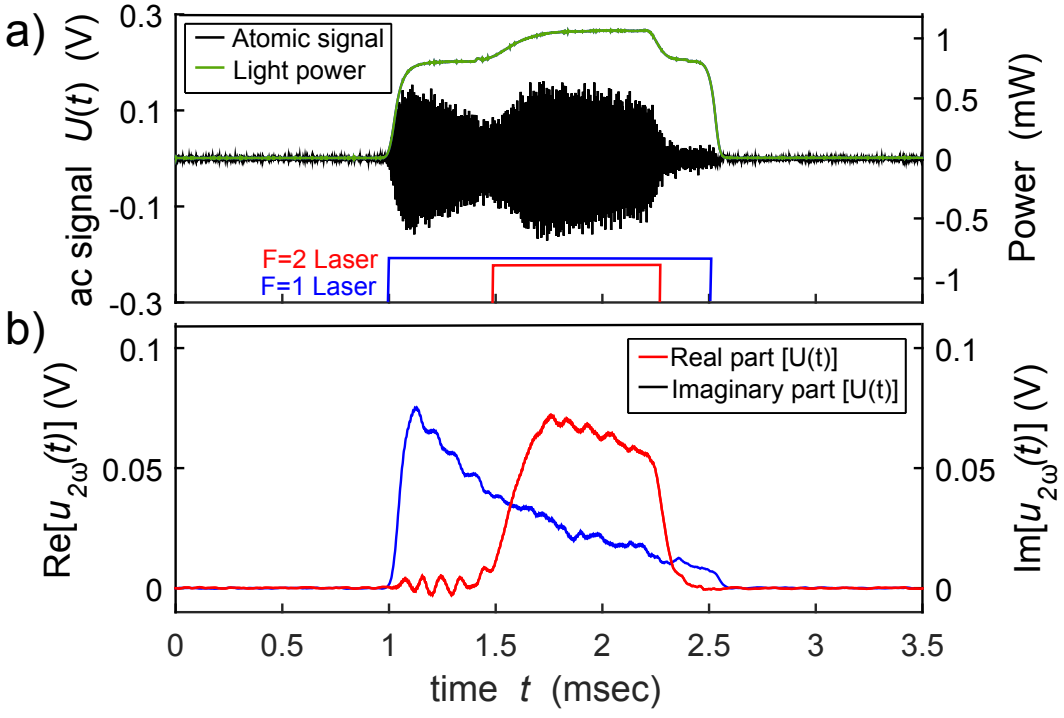


FIGURE 5.9: The figure shows a sample simultaneous measurement of two states realized with state to quadrature mapping. Panel a) gives the raw ac signal U(t) in Volts (black) from the balanced photodiode. The green signal gives the laser beam power monitored by the photodiode. The two detection beam intensities cannot be separated on the photodiode, but the red and blue pulses inserted show the duration of the two detection beams set by the control sequence. Panel b) shows the signal intensities from the two states separated by phase, i.e. the real (blue) and imaginary (red) parts of the ac signal U(t) showing the signals from the atoms in the $|F = 1\rangle$ and $|F = 2\rangle$ levels respectively.

These signals can now be analyzed to get the state transfer probability of the two states as shown in previous sections. Performing this detection with a single laser would circumvent noise due to laser intensity and frequency fluctuations that is inherent in detecting the two states with different lasers as described so far. To use a single laser for the process, an EOM can be used that uses an input frequency and outputs two sidebands at ≈ 3.4 GHz thus giving two pulses separated by ≈ 6.8 GHz. These sidebands can be shone onto the atoms as discussed in Section 4.2 and the two signals separated using their phase as described here.

5.5.2 Reduction of detection noise with a low-finesse cavity

At the optimal detuning with common mode noise suppression, the technical noise in our system is 0.18% which is 25 dB away from the atomic shot noise 0.01% for 10^8 atoms. The light - atom interaction strength for this measurement given by the inverse ratio of the detection noise to the atomic shot noise is $\kappa^2 = 0.081$. To reach the atomic shot noise level, the interaction strength has to be increased to 1 which can be done by implementing a low - finesse cavity around the UHV chamber which has to have a finesse of at least $1/0.08 = 12.5$.

Part II

Radio-Frequency Dressed Microwave Spectroscopy

Summary

The extension of quantum memory or atom interferometric schemes to magnetically trapped atomic systems require measurements with trappable states instead of non-trappable clock states used elsewhere. Performing quantum memory experiments with atoms loaded into a Hollow-Core Fibre using an atom chip, as proposed in Section 1.1, requires such a modification. This part demonstrates the possibility of addressing the trappable clock states in the electronic ground state hyperfine ensemble of ^{87}Rb atoms. The atomic levels are dressed with an RF field to facilitate pseudo one-photon transitions between the two sub-ensembles of the ground state with frequencies in the microwave range. Chapter 6 gives the proof of concept of microwave spectroscopy with RF dressed atoms and discusses the data shown in the context of our experiment. Chapter 7 concentrates on the three narrow transitions seen, that we shall refer to as the clock triplet. The characterization of these transitions and identification of limitations is necessary before their use in atom interferometry schemes.

Chapter 6

Radio-frequency Dressed Microwave Spectroscopy

This chapter discusses the use of an RF dressing field for ^{87}Rb atoms and the microwave transitions between the electronic ground state hyperfine sub-ensembles that become possible with it. Detecting and characterizing the RF dressed microwave transitions with parameters like the static and RF field strengths is required to optimize these parameters for particular transitions that can be used in future schemes. Section 6.1 elaborates the discussion on the RF dressing fields given in Section 4.1 that are used in these experiments to derive the frequencies of the Rabi oscillations induced in the atoms due to this dressing. Section 6.2 illustrates the pseudo one-photon microwave transitions between the RF dressed hyperfine sub-ensembles with data to compare microwave spectra taken with bare states and RF dressed states. Section 6.3 explains the experimental sequence used to collect data and notes the effect of different parameters on the transitions in the spectra. Section 6.4 discusses the collection of data in different geometrical configurations in our experiment and explains their significance. Section 6.5 categorizes the group of dressed transitions around one of the bare transitions with experimental data.

6.1 RF Dressing of the ground state ensemble

This section builds on the effective field description of the interaction Hamiltonian between the RF dressed atoms and the static magnetic field B_{DC} in Section 4.1.1 to derive the Eigenvalues of the effective Hamiltonian that describe the energies of the dressed states. The effective magnetic field $\mathbf{B}_{\text{eff}}$ that the atoms see due to the adiabatic RF dressing and the interaction Hamiltonian of the atoms with the field are given by Equation 4.1 and Equation 4.4 respectively. As the frequency of the RF field ω is much larger than the effective Larmor frequency ($\mu_B g_F B_{\text{eff}}$), the Rotating Wave Approximation can be applied to the Hamiltonian. This discards the time dependent terms in the rotating frame Hamiltonian given in Equation 4.6 to give

$$\hat{H}_{F=1} = \mu_B . g_F \left(\left(B_{\text{DC}} - B_{\text{res1}} \right) \hat{F}_z + \frac{B_- \hat{F}_- + B_-^\dagger \hat{F}_+}{2\sqrt{2}} \right)$$

$$\text{and} \quad \hat{H}_{F=2} = \mu_B . g_F \left(\left(B_{\text{DC}} - B_{\text{res2}} \right) \hat{F}_z + \frac{B_+ \hat{F}_+ + B_+^\dagger \hat{F}_-}{2\sqrt{2}} \right) \tag{6.1}$$

where $B_{\text{res1,2}}$ are the positive resonant fields for the RF coupling as given in Equation 4.7 for the $|F = 1\rangle$ and the $|F = 2\rangle$ levels respectively. These equations reflect the fact that the $|F = 1\rangle$ sub-levels are coupled by the B_- RF field whereas the $|F = 2\rangle$ sub-levels are coupled by the B_+ RF field.

Further, for spin-1/2 systems such as ^{87}Rb, this Hamiltonian can be expressed in the $|\uparrow\rangle, |\downarrow\rangle$ basis described in Section 2.1 wherein the spin operators $\hat{F}_z$, $\hat{F}_+$ and $\hat{F}_-$ can be expressed as $\frac{1}{2}\begin{pmatrix} 1 & 0 \\ 0 & -1 \end{pmatrix}$, $\begin{pmatrix} 0 & 1 \\ 0 & 0 \end{pmatrix}$ and $\begin{pmatrix} 0 & 0 \\ 1 & 0 \end{pmatrix}$. In this description, the Hamiltonians for the two levels can be written as

$$\hat{H}'_{F=1} = \frac{1}{2}\begin{bmatrix} \mu_B g_F B_{\text{DC}} - \hbar\omega & \frac{\mu_B g_F B_-}{\sqrt{2}} \\ \frac{\mu_B g_F B_-^\dagger}{\sqrt{2}} & -\mu_B g_F B_{\text{DC}} + \hbar\omega \end{bmatrix}$$

$$\text{and} \quad \hat{H}'_{F=2} = \frac{1}{2}\begin{bmatrix} \mu_B g_F B_{\text{DC}} - \hbar\omega & \frac{\mu_B g_F B_+}{\sqrt{2}} \\ \frac{\mu_B g_F B_+^\dagger}{\sqrt{2}} & -\mu_B g_F B_{\text{DC}} + \hbar\omega \end{bmatrix} \tag{6.2}$$

The RF field leads to new energies for the dressed states. These energies, described by the Eigenvalues of the reduced Hamiltonian in Equation 6.2 are given by

$$E_{|F=1,m\rangle} = \mathrm{m}_F.\mu_B.g_F|\mathbf{B}_{\mathrm{eff}}| = \mathrm{m}_F.\mu_B.g_F\sqrt{\frac{|B_-|^2}{2} + \left(B_{\mathrm{DC}} - B_{\mathrm{res,F=1}}\right)^2}$$

$$E_{|F=2,m\rangle} = \mathrm{m}_F.\mu_B.g_F|\mathbf{B}_{\mathrm{eff}}| = \mathrm{m}_F.\mu_B.g_F\sqrt{\frac{|B_+|^2}{2} + \left(B_{\mathrm{DC}} - B_{\mathrm{res,F=2}}\right)^2} \tag{6.3}$$

where F represents the hyperfine sub-ensemble (F = 1,2 for ^{87}Rb) and m_F their magnetic quantum numbers.

The anti-diagonal elements in Equation 6.2 represent the coupling frequencies $\Omega_{\mathrm{RF}\pm}$ for the two sub-ensembles $|F = 1\rangle$ and $|F = 2\rangle$ where

$$\begin{aligned}\Omega_{RF\pm} &= \frac{\mu_B.g_F.|B_{\mathrm{eff}}|}{\hbar} \\ &\approx \frac{\mu_B.g_F.|B_\pm|}{\sqrt{2}\hbar}\end{aligned} \tag{6.4}$$

It is to be noted here that the two coupling frequencies Ω_{RF+} and Ω_{RF-} are not exactly equal as the resonant static fields for the two levels $B_{\mathrm{res1,2}}$ are usually of slightly different magnitudes.

The Hamiltonians $\hat{H}'_{F=1}$ and $\hat{H}'_{F=2}$ can now be written in a neater fashion as

$$\hat{H}'_{F=2,1} = \frac{1}{2}\begin{bmatrix} \mu_B g_F B_{\mathrm{DC}} - \hbar\omega & \hbar\Omega_{RF\pm} \\ \hbar\Omega^\dagger_{RF\pm} & -\mu_B g_F B_{\mathrm{DC}} + \hbar\omega \end{bmatrix} \tag{6.5}$$

The σ_+ polarized field B_+ couples the $|F = 2\rangle$ levels with the frequency Ω_{RF+} and the σ_- polarized field B_- couples the $|F = 1\rangle$ levels with the frequency Ω_{RF-}. For a linearly polarized RF field with $|B_+| = |B_-|$, the two sub-ensembles will be coupled with nearly the same frequency. Figure 6.1 illustrates the splitting of the energy levels due to the RF field applied.

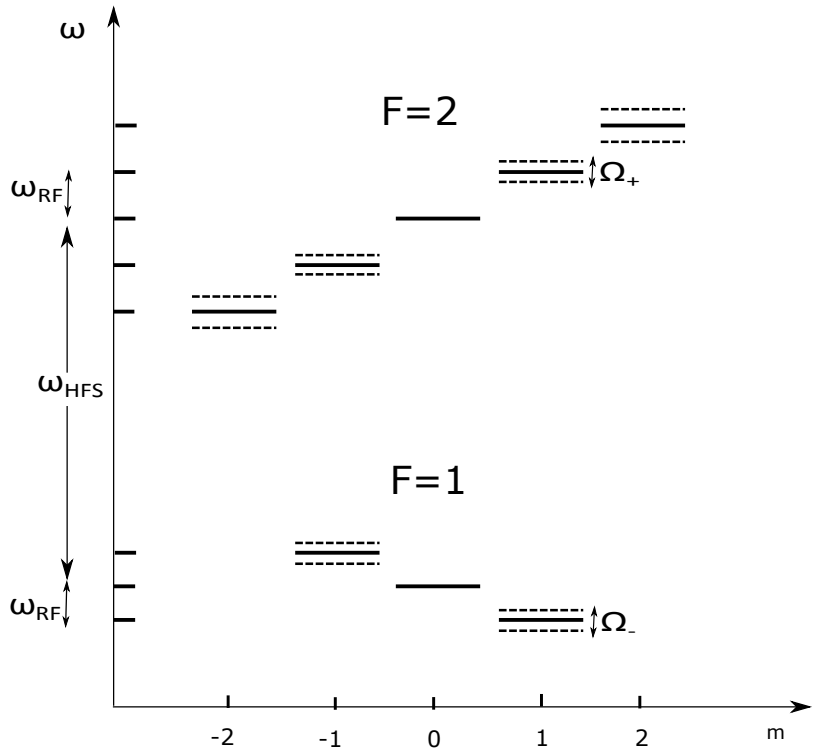


FIGURE 6.1: The figure shows the energy levels splitting due to the RF field applied. The Zeeman splitting occurring due to the static magnetic field is responsible for the $\hbar\omega_{RF}$ energy gap between consecutive levels. The RF field induces splitting of magnitude $\frac{1}{2}\hbar\Omega_+$ in the $|F = 2\rangle$ levels and $\frac{1}{2}\hbar\Omega_-$ in the $|F = 1\rangle$ levels.

When the static field B_{DC} is at resonance B_{res} such that $\mu_B g_F B_{DC} = \hbar\omega$, the Eigenvalues of the Hamiltonian become $E_\pm = \pm\frac{1}{2\sqrt{2}}\mu_B.g_F.|B_+| = \pm\frac{1}{2}\hbar|\Omega_+|$ for the $|F = 2\rangle$ levels and $E_\pm = \pm\frac{1}{2\sqrt{2}}\mu_B.g_F.|B_-| = \pm\frac{1}{2}\hbar|\Omega_-|$ for the $|F = 1\rangle$ levels.

With this description in place, the interactions of the dressed states with microwave fields can be studied.

6.2 Microwave Interaction

This section discusses the microwave interaction between the $|F = 1\rangle$ and the $|F = 2\rangle$ sub-ensembles of the ^{87}Rb ground state and determines the frequencies of the bare and RF dressed transitions in terms of the RF coupling frequencies. The field coupling the two sub-ensembles is the magnetic component of the microwave field. The total magnetic field that the atoms see is given by

$$\mathbf{B}(t) = \mathbf{B}_{\mathrm{DC}} + \mathbf{B}_{\mathrm{RF}}(t) + \mathbf{B}_{\mathrm{MW}}(t), \tag{6.6}$$

The nine MW transitions possible in the bare states (when $\mathbf{B}_{\mathrm{RF}}(t) = 0$) occur at frequencies given by:

$$\omega_{MW\,\mathrm{Bare}} = \omega_{HFS} + \mathrm{m}_1\omega_B + \mathrm{m}_2\omega_B \tag{6.7}$$

where m_1 is defined as the magnetic quantum number m_F for the $|F = 1\rangle$ levels and m_2 that for the $|F = 2\rangle$ levels. Following the selection rules, $\Delta m = m_2 - m_1 \in [-1, 0, 1]$. The hyperfine splitting ω_{HFS} for ^{87}Rb atoms is 6.834682610GHz and ω_B is the first order Zeeman splitting of the two sub-ensembles due to the static magnetic field $\mathbf{B}_{\mathrm{DC}}$ applied. The nine transitions are represented in the schematic Figure 6.2a) and are marked as σ_+, π or σ_- polarized depending on Δm_F of the transition. However, the pair of transitions $|F, m\rangle : |1, 0\rangle \rightarrow |2, -1\rangle$ and $|1, -1\rangle \rightarrow |2, 0\rangle$ occur at the same MW detuning $(-\omega_{RF})$ from the clock transition $|F, m\rangle : |1, 0\rangle \rightarrow |2, 0\rangle$ and the pair of transitions $|F, m\rangle : |1, 0\rangle \rightarrow |2, 1\rangle$ and $|1, 1\rangle \rightarrow |2, 0\rangle$ occur at the same ω_{RF} MW detuning; so the bare MW spectrum shows only seven transitions.

Due to the RF coupling of the magnetic sub levels in the $|F = 1\rangle$ and $|F = 2\rangle$ levels, each of the bare transitions mentioned above give rise to transitions from the other sub levels, as essentially, the atoms in the $|F = 1\rangle$ level are oscillating among its sub levels and likewise for the atoms in the $|F = 2\rangle$ level. Therefore, each of the bare transitions can give rise to 15 transitions in the RF dressed picture, i.e. from

each of the three $|F = 1\rangle$ sub levels to each of the five $|F = 2\rangle$ sub levels. These transitions are represented in the schematic Figure 6.2b) which shows the group of MW transitions in the dressed picture which arise from any of the bare transitions given in Equation 6.7.

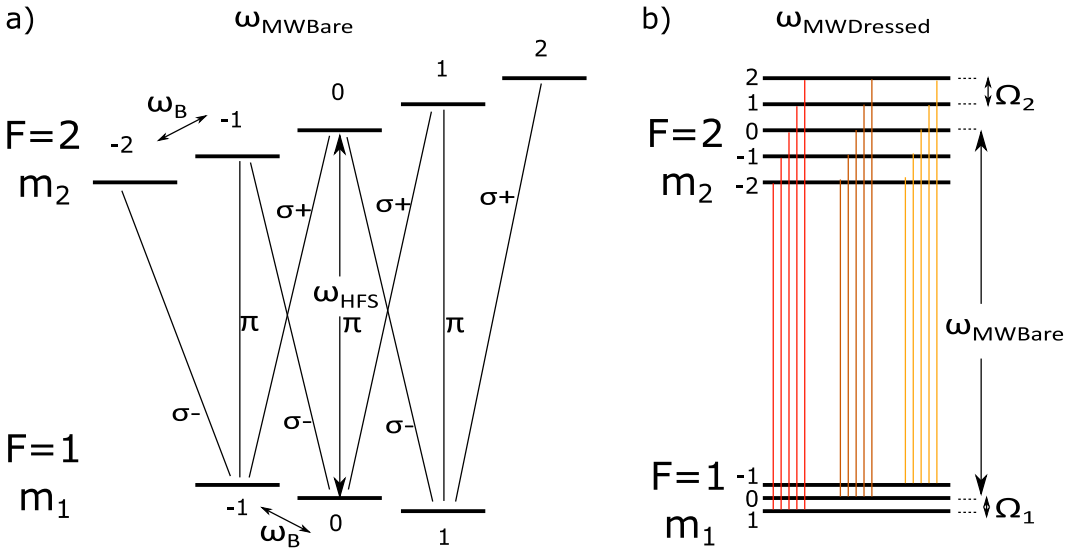


FIGURE 6.2: The figure shows the nine bare MW transitions in panel a) with two pairs of degenerate transitions evident from the frequencies $\omega_{MW\text{Bare}}$ given by Equation 6.7, where $\omega_{HFS} \approx 6.8$ GHz. Panel b) shows the 15 RF dressed transitions possible around each bare MW transition (from each of the three $|F = 1\rangle$ sub-levels to each of the five $|F = 2\rangle$ sub-levels) with the frequencies $\omega_{MW\text{Dressed}}$ given by Equation 6.8.

To write down the frequencies at which the RF dressed MW transitions occur, we have to note that the m_F sub levels in the $|F = 1\rangle$ level oscillate at $m_F.\Omega_{RF-}$ frequencies whereas the m_F sub levels in the $|F = 2\rangle$ level oscillate at $m_F.\Omega_{RF+}$ frequencies due to the RF dressing where $\Omega_{RF\pm}$ are given by Equation 6.4. Therefore, the frequencies at which transitions in between the RF dressed states occur can be derived as for the bare transitions in Equation 6.7, but with additional terms containing $\Omega_{RF\pm}$ as:

$$\begin{aligned}\omega_{MW\text{Dressed}} &= \omega_{MW\text{Bare}} + \mathrm{m}_1\Omega_{RF-} + \mathrm{m}_2\Omega_{RF+} \\ &= \omega_{HFS} + m_{Bare}.\omega_{RF} + \mathrm{m}_1\Omega_{RF-} + \mathrm{m}_2\Omega_{RF+} \end{aligned} \tag{6.8}$$

where $m_{Bare} \in [-3,-2,-1,0,1,2,3]$ is used to represent the 7 bare transitions mentioned previously; m_1 and m_2 in this case go over all the m_F sub levels, i.e. $m_1 \in [-1,0,1]$ and $m_2 \in [-2,-1,0,1,2]$. The frequency ω_{RF} is the first order Zeeman splitting of the two sub-ensembles at the resonant static magnetic field $\mathbf{B}_{res}$ and is equal to the frequency of the RF field applied. As seen from Figure 6.2, each of the 7 bare transitions lead to 15 transitions in the RF dressed case, giving a total of 105 transitions possible in the RF dressed MW spectrum. Experimental data for one group of 15 transitions is provided in Section 6.5.2. Figure 6.3 gives the experimental data for the bare and RF dressed MW spectra to substantiate the Figure 6.2.

The details of the experimental sequence and setup are given in Sections 6.3 and 6.4, this set of data is included here only to illustrate the concept of RF dressed MW transitions. Figure 6.3a) gives the MW spectrum of the bare transitions from $\approx 1 \times 10^8$ atoms prepared in a mixed state of the three $|F = 1\rangle$ sub-levels and MW interaction duration of 8 ms. The signals from the $|F = 2\rangle$ levels are the linear birefringent signals taken with our technique of RF dressed detection and it should be noted that the amplitude of signals from each sub-level is proportional to its S_2 moment given in Table 3.1. The signals are normalized to detection beam intensity. The MW Detuning shown in both the graphs is the detuning from the clock transition $|F,m\rangle : |1,0\rangle \rightarrow |2,0\rangle$ at $\omega_{HFS} \approx 6834682$ kHz and the data is taken with a resolution of 2 kHz. The static field $\mathbf{B}_{\mathrm{DC}}$ is set to ≈ 430 mG during the MW interaction, which results in $\omega_B \approx 300$ kHz.

Figure 6.3b) gives the MW spectrum of the RF dressed transitions from $\approx 1 \times 10^8$ atoms prepared in a mixed state of the three $|F = 1\rangle$ sub-levels and MW interaction duration of 8 ms. The states are dressed with an RF field of 180 kHz before the MW interaction and the signals shown are the dressed linear birefringent signals from the $|F = 2\rangle$ sub-levels. The frequency ω_B in this case is the RF field frequency $\omega_{RF} = 180$ kHz and represents the gap between consecutive groups of transitions. The signals shown here are normalized to atom number (with a linear trend fit to the signals from the $|F = 1\rangle$ levels) and detection beam intensity. The

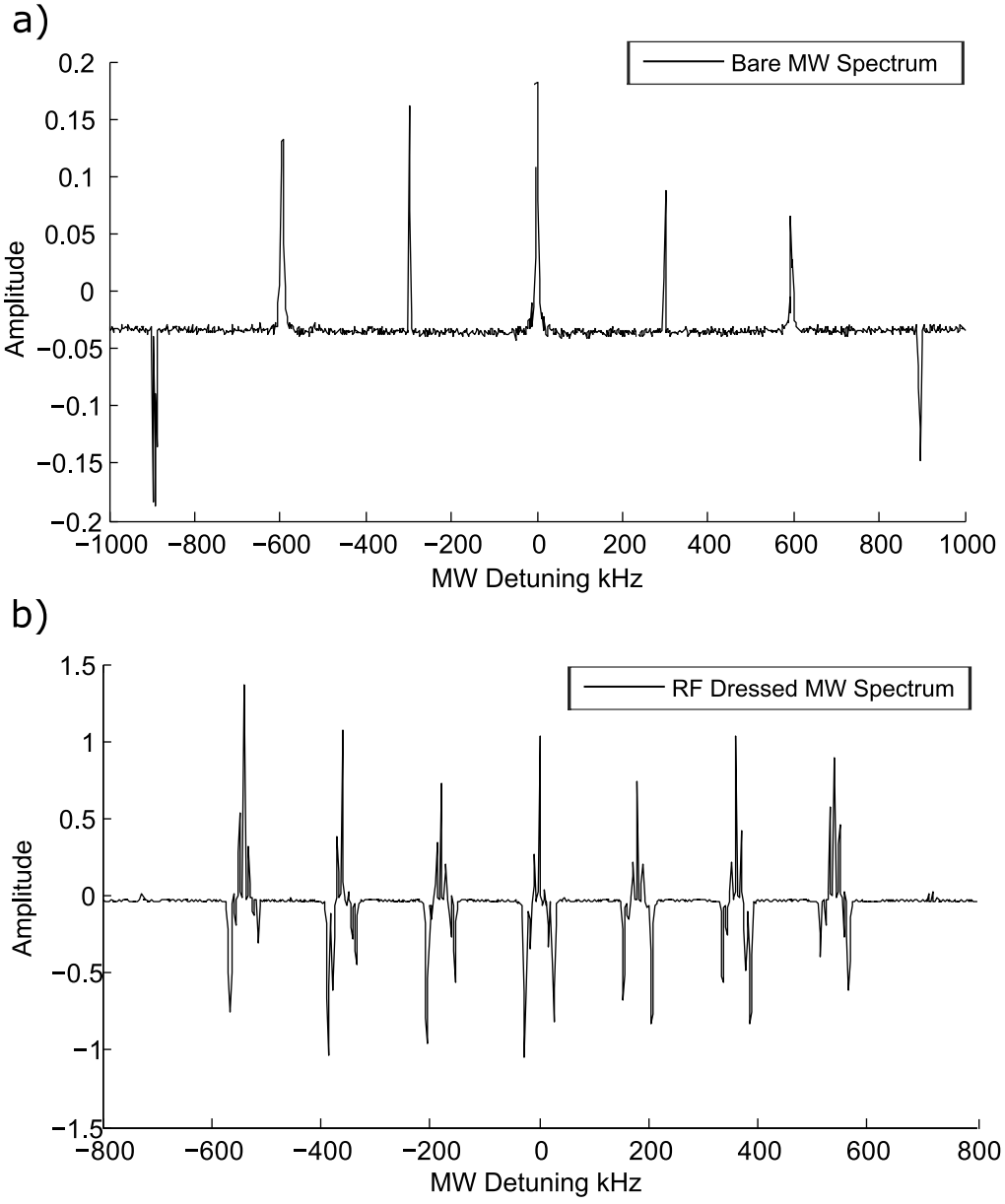


FIGURE 6.3: The figure gives experimental RF dressed detection signals from the $|F = 2\rangle$ levels showing MW spectra from 10^8 atoms initially in a mixed state of the $|F = 1\rangle$ levels which are driven with MW pulses of different frequencies, 8 ms duration and 100 mW power. The detuning shown in the figures is from the clock transition $\omega_{HFS} = 6834682$ kHz. Panel a) shows the bare MW transitions, i.e the RF dressing field $B_{RF} \approx 11$ mG is introduced for the detection after the MW interaction. The static field is set to ≈ 430 mG which results in $\omega_B = 300$ kHz. Panel b) shows the RF dressed MW transitions, i.e. the dressing field is introduced before the MW interaction and left at the same amplitude for the detection. The static field is set to 260 mG which results in $\omega_B = \omega_{RF} = 180$ kHz.

normalization to atom number removes the effect of changes in atom number of the MOT on the signals' amplitudes over the duration of the whole experiment.

6.3 Experimental Sequence

This section explains the experimental setup and sequence used for the RF dressed MW spectroscopy experiments. The setup remains the same as in Section 4.2 and the experiment can be conducted in the orthogonal or parallel setting (to the MW magnetic field component in the y-axis) by ramping the static magnetic field in the y- or z- axis. Figure 6.4 shows the experimental sequence.

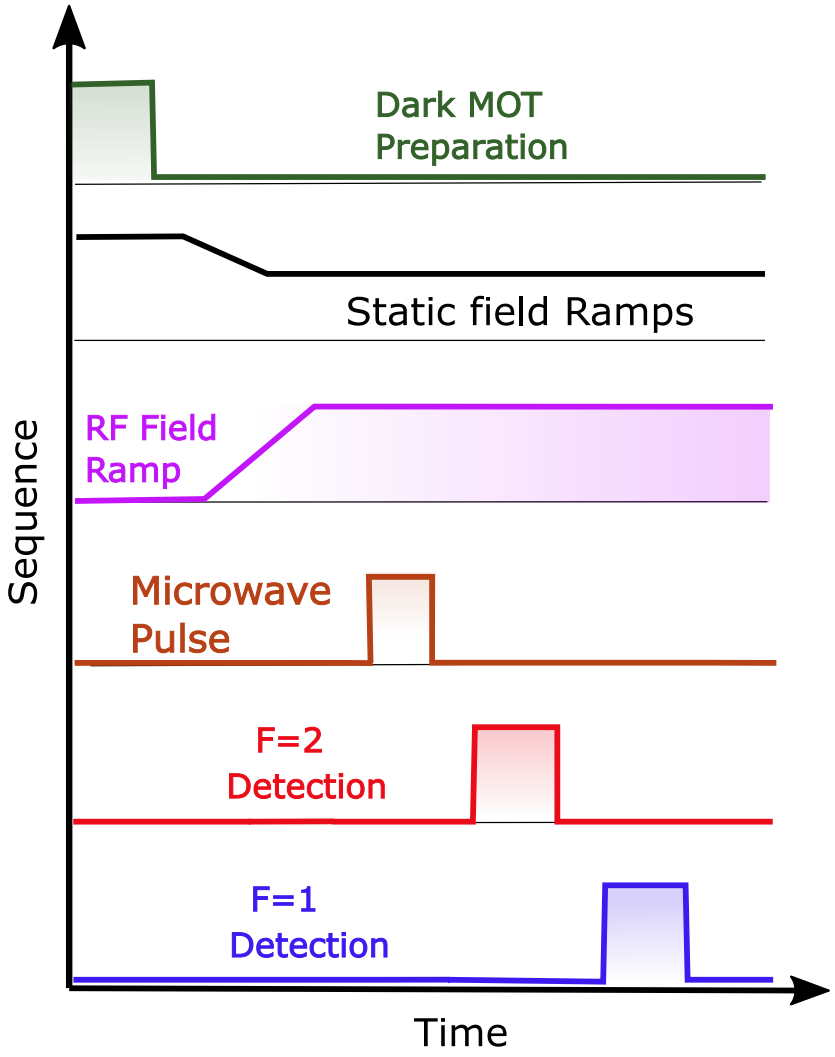


FIGURE 6.4: The figure shows the experimental sequence used to obtain RF dressed MW spectra. The atoms are usually prepared in a Dark MOT, i.e. a mixed state of $|F = 1\rangle$ levels unless stated otherwise. The Static field and RF dressing field are ramped to typical values of 260 mG and 11 mG respectively. A MW pulse of varied frequency and power is shone to induce Rabi cycles from the $|F = 1\rangle$ levels to the $|F = 2\rangle$ levels after which atom numbers are measured in both the levels with the two Detection Beams.

The process is started with the preparation of a Dark MOT by shining the Cooler beams for 2 ms without the Repumper beam. The static field is ramped to $\mathbf{B}_{res}$ in the orthogonal or parallel setting. At nearly the same time, the RF field is ramped adiabatically to $\mathbf{B}_{RF}$ in 3 ms. The MW pulse is shone for varied durations, the frequency and pulse intensity set by digital modulation of the source. The transitions are marked by the amplitude of the atomic signals from the two states by the dressed detection method. The strengths of the Rabi oscillations induced at each of the frequencies $\omega_{MW\text{Dressed}}$ are dependent on the intensities of the MW pulses and the Clebsh-Gordon coefficients of the transitions. The atomic numbers in the sub levels involved in the transitions also depend on the durations of the MW pulses. The signals from the $|F = 1\rangle$ levels are useful for estimating the atom numbers in the MOT and any trends over the duration of the whole experiment so that the signals from the $|F = 2\rangle$ levels can be normalized to atom number. All signals are also normalized to detection beam intensities.

6.4 Orthogonal and Parallel Settings

This section discusses the experimental configurations possible and the transitions seen in each. The static magnetic field ramped in the sequence Figure 6.4 in the y- or z- axes sets the setup in the orthogonal or parallel configuration to the magnetic field component of the MW field. The Figure 6.5 gives the schematic figures and the experimental data taken in the two configurations.

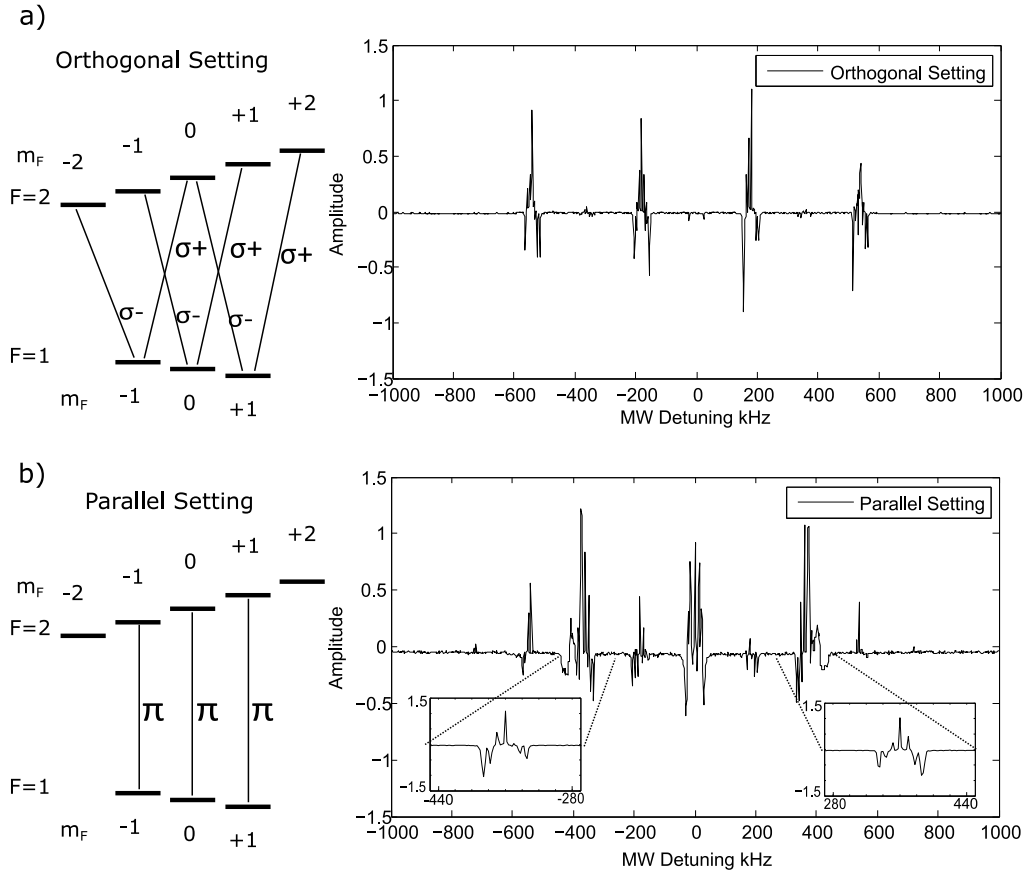


FIGURE 6.5: The figure gives experimental RF dressed detection signals from the $|F = 2\rangle$ levels showing MW spectra from 10^8 atoms initially in a mixed state of the $|F = 1\rangle$ levels which are driven with MW pulses of different frequencies, 8 ms duration and 100 mW power. The detuning shown in the figures is from the clock transition ω_{HFS} = 6834682 kHz. Panel a) shows the dressed MW spectrum in the orthogonal setting which allows the groups of transitions around the bare σ transitions. Panel b) shows the dressed MW spectrum in the parallel setting which allows the groups of transitions around the bare π transitions. The data collection starts at 0 kHz detuning and alternates between positive and negative detunings in steps of 2 kHz, which means the anomalies near ±410 kHz occurred in the same time period. The insets show another set of data from 280 kHz to 400 kHz and from −280 kHz to −400 kHz without the anomalies, therefore the anomalies in the current set are attributed to external field noise.

Figure 6.5a) shows the schematic of the bare transitions and the experimental data of the RF dressed MW transitions taken in the orthogonal configuration of the experiment with $\approx 1 \times 10^8$ atoms in the MOT that are prepared in a superposition of the $|F = 1\rangle$ sub levels. Only the $\sigma+$ and $\sigma-$ transitions occur in the bare states case, i.e. where $\Delta m = m_2 - m_1 \in [-3, -1, 1, 3]$. Therefore, the only transitions that occur in the dressed case are the ones based on these transitions. The data shown here is taken with MW pulses of 20 dBm power and 8 ms duration and at a resolution of 2 kHz. The transitions in the other groups that occur with very small amplitudes are due to slight experimental misalignments. The signals shown here are from $|F = 2\rangle$ state and are normalized to detection beam intensities and atom number trends from the $|F = 1\rangle$ signals.

Figure 6.5b) shows the schematic of the bare transitions and the experimental data of the RF dressed MW transitions taken in the parallel configuration of the experiment with $\approx 1 \times 10^8$ atoms in the MOT that are prepared in a superposition of the $|F = 1\rangle$ sub levels. The transitions that occur in the bare states case are π polarized, i.e. where $\Delta m = m_2 - m_1 \in [-2, 0, 2]$ and hence only the groups that arise from these transitions occur strongly in the RF dressed states case. The data shown here is taken with MW pulses of 20 dBm power and 8 ms duration and at a resolution of 2 kHz. Due to experimental static field misalignments, the data also shows the groups based on σ polarized transitions with lower strengths. As always, the signals are normalized to atom number trends and detection beam intensities.

For the sake of completeness, it should be mentioned that the data shown in Figure 6.3b) are taken with the same experimental conditions as here except for the static field which is aligned at a 45° angle to the MW magnetic field. This allows both the σ and the π transitions to occur in the bare states case and thus, all seven groups occur with equal strengths in the RF dressed case.

6.5 Dressed Transitions from individual sub-levels at ω_{RF} detuning

This section looks at the experimental data of the group of transitions that occur at 1 ω_{RF} MW detuning from the bare clock transition, i.e. the transitions that arise from the $|F, m\rangle : |1, 0\rangle \rightarrow |2, 1\rangle$ bare transition. We try to separate the 15 transitions into three categories, one from each of the individual sub levels of the $|F = 1\rangle$ level. This enables us to assign frequencies to each of the transitions in the group with better accuracy than if we were to look at the transitions from atoms prepared in a superposition of the $|F = 1\rangle$ level. This designation of experimental frequencies to individual transitions in the group allows us to compare the data to the theoretical frequencies of the RF dressed transitions given in Equation 6.8.

6.5.1 Preparation of individual sub-levels

To separate the 15 transitions in the group into the three categories, we try to prepare the initial state of the atoms for the MW interaction such that most of the atoms are in only one m_F sub-level. Experimentally, this has been easier for the $|F, m\rangle : |1, 0\rangle$ sub-level than for the other two.

Preparation of $|1, 0\rangle$ sub-level

The preparation of the $|1, 0\rangle$ sub-level follows the state preparation process discussed in Section 3.3 except for the Optical Pumping step. This results in $|1, 0\rangle$ sub-level atom number that is $\approx 50\%$ of the atoms in the initial MOT. This state is clean as the remaining atoms are blown away as discussed in the state preparation process.

Preparation of $|1,-1\rangle$ and $|1,1\rangle$ sub-levels

The preparation of the $|1,-1\rangle$ is less straightforward. We first prepare a superposition of the $|1,-1\rangle$ and $|1,1\rangle$ sub-levels by removing the atoms in the $|1,0\rangle$ sub-level of a Dark MOT. This is done by shining a π pulse on the clock transition and to excite the atoms to the $|2,0\rangle$ sub-level and blowing these atoms away. We then try to shine a π pulse on the $|F,m\rangle : |1,1\rangle \rightarrow |2,1\rangle$ transition with a MW frequency as given in the bare MW spectrum shown in Figure 6.3a). As this transition happened to be $\approx$ 15kHz broad, we achieved this with repeated MW pulses separated by 3kHz alternating with blowing away the atoms in the excited level. However, a clean $|1,-1\rangle$ state has not been achieved, but the atom number in the $|1,1\rangle$ level has been greatly reduced. The resulting atom number in the $|1,-1\rangle$ is $\approx$ 33% of the number in the initial MOT.

The $|1,1\rangle$ state is likewise prepared to get a $\approx$ 33% atom number with a similar process. The atom number in the $|1,-1\rangle$ sub-level is reduced by shining the MW pulses on the $|F,m\rangle : |1,-1\rangle \rightarrow |2,-1\rangle$ transition. As in the above case, a clean state has not been achieved.

6.5.2 Data of the dressed transitions

We look at the transitions from the individual sub-levels by taking dressed MW spectra around 180 kHz MW frequency detuning with each of the above prepared states. The spectra are taken at the static field resonant with the $|F=2\rangle$ level RF coupling, with $\approx 3-5\times10^7$ atoms in each sub-level, 5 dBm MW pulse power and 5 ms pulse duration. The resolution of the data is 0.2 kHz.

The three spectra are shown in Figure 6.6. The spectrum from the $|1,0\rangle$ prepared state is clean and shows only the five expected transitions to the $|F=2\rangle$ level. The other two spectra however have extra transitions due to the prepared state not being entirely clean. These transitions are separated by looking at the five stronger transitions in the two spectra and assigning them to their respective states.

These experimental frequencies can be compared to the frequencies derived from Equation 6.8, plotted in the same figure. The experimental frequencies match the expected frequencies for Ω_{RF+} = 8.2 kHz and Ω_{RF-} = 7.8 kHz. The inequality in the two coupling frequencies is due to the difference in the resonant static fields $\mathbf{B}_{res}$ for the two levels.

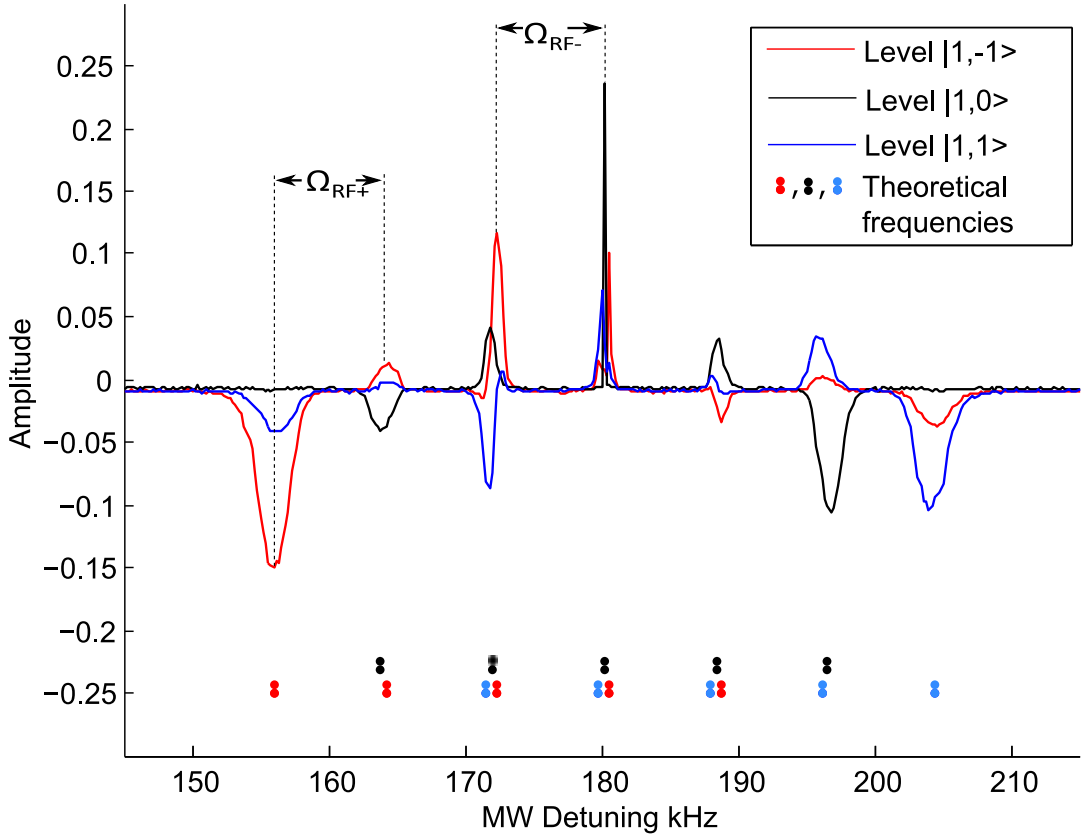


FIGURE 6.6: The figure shows experimental data of the dressed transitions around MW detuning = ω_{RF} = 180 kHz from ω_{HFS}, along with theoretical frequencies calculated using Equation 6.8 with Ω_{RF+} = 8.2 ± 0.4 kHz and Ω_{RF-} = 7.8 ± 0.4 kHz, the inequality due to the difference in B_{res} for the two levels. Of the 15 transitions, 5 transitions can be assigned to each of the $|F = 1\rangle$ sub-levels as shown in Figure 6.2b), which is discussed in the text. This figure is high resolution data (0.2 kHz) of the transitions around 180 kHz in Figure 6.3 and is taken in the orthogonal setting (as in Figure 6.5).

It is evident from the figure that the coupling frequency Ω_{RF+} represents the gap between the consecutive transitions in each category and the coupling frequency Ω_{RF-} represents the gap between consecutive categories. It is to be noted that

the narrowest transitions in the group are the three transitions nearest to the ω_{RF} detuned frequency which is where the dressed clock transition occurs and the transitions get broader as the MW frequency is detuned further from this dressed clock transition frequency. The three narrow transitions represent the $|F, m\rangle : |1, 0\rangle \rightarrow |2, 0\rangle$, $|F, m\rangle : |1, -1\rangle \rightarrow |2, 1\rangle$ and $|F, m\rangle : |1, 1\rangle \rightarrow |2, -1\rangle$ transitions. The widths of the 15 transitions are not rigorously examined with MW frequency detuning in this thesis.

Chapter 7

Characterization of the Dressed Clock Transitions

This Chapter builds on the theory and data presented in Chapter 6 to analyze the three narrow transitions seen - $|F, m\rangle : |1, 0\rangle \rightarrow |2, 0\rangle$, $|F, m\rangle : |1, -1\rangle \rightarrow |2, 1\rangle$ and $|F, m\rangle : |1, 1\rangle \rightarrow |2, -1\rangle$. The occurrence of these transitions allows the extension of schemes in various fields like Quantum Memory or Atomic Clocks and Interferometry to include trappable states and the advantages they offer. The dependence of these transitions on various experimental parameters have to be examined before designing such schemes. The Section 7.1 shows the three clock transitions that occur in the RF dressed ground state ensemble of ^{87}Rb atoms. The characterization of these transitions with the static magnetic field is shown in Section 7.2. The strengths of these transitions are characterized in Section 7.3.

7.1 The clock transitions

This section shows the occurrence of the three transitions $|F, m\rangle : |1, 0\rangle \rightarrow |2, 0\rangle$, $|F, m\rangle : |1, -1\rangle \rightarrow |2, 1\rangle$ and $|F, m\rangle : |1, 1\rangle \rightarrow |2, -1\rangle$ with experimental data. First, it is important to note that the frequencies at which these transitions occur, from Equation 6.8, would have been equal if $\Omega_{RF+} = \Omega_{RF-}$. This would translate to the equality of the effective magnetic fields seen by the two levels. But these two factors differ slightly due to the different resonant static fields at which the two levels couple, as discussed in Section 4.3.3. Due to this, the two coupling frequencies Ω_{RF+} and Ω_{RF-} differ by ≈ 0.25 kHz at the 10 mG linearly polarized RF field applied and the static field $\mathbf{B}_{DC} = \mathbf{B}_{\text{res}}$ for the $|F = 2\rangle$ level. This difference in the three frequencies is evident in Figure 7.1 below.

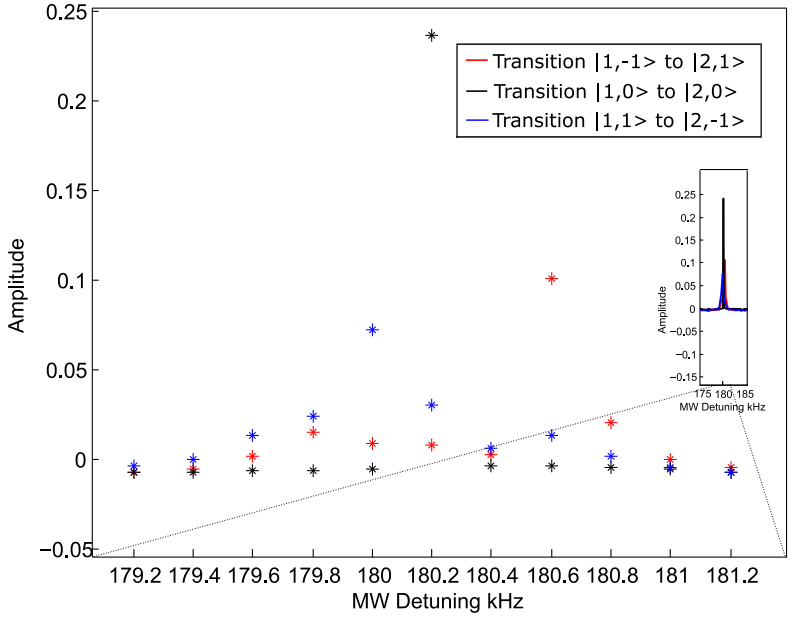


FIGURE 7.1: The figure gives experimental linear birefringence signals from the $|F = 2\rangle$ levels showing the three narrow RF dressed clock transitions, one from each of the three $|F = 1\rangle$ sub-levels. The inset gives the part of Figure 6.6 showing the same transitions. The figure combines three separate data sets, each one with $3 - 5 \times 10^7$ atoms prepared in a single $|F = 1, m_F\rangle$ sub-level as discussed in Section 6.5.1. The data is taken with 5 ms MW pulse duration and 0.2 kHz resolution which is limited by the impure preparation of $|F = 1, m_F = \pm 1\rangle$ sub-levels, as discussed in the text.

The Figure 7.1 shows the occurrence of the three narrow dressed transitions at slightly different frequencies. These dressed transitions arise out of the bare

$|F, m\rangle : |1, 0\rangle \rightarrow |2, 1\rangle$ transition at 180 kHz. Due to the impure preparation of $|F = 1, m_F = \pm 1\rangle$ sub-levels, as given in Section 6.5.1, the data from those sub-levels shows signals at two frequencies - the stronger being from the prepared sub-level and the weaker signal from the atoms left in the other sub-level. The resolution of the data taken is restrained to be able to separate the two transitions and assign them to one of the sub-levels. The occurrence of the transition from $|1, 0\rangle$ at 180.2 kHz instead of the theoretical 180 kHz calculated using Equation 6.8 implies that the MW source is 200 Hz off and shines a 180 kHz pulse when it is digitally programmed to 180.2 kHz.

7.2 Dependence on static field magnitude

This section looks into the dependence of the dressed transitions on the static magnetic field $\mathbf{B}_{DC}$ during the MW interaction. The energy Eigenvalues of the sub-levels in the $|F = 2\rangle$ and $|F = 1\rangle$ levels are given by the Equation 6.3, which clearly gives the dependence of each on the static magnetic field $\mathbf{B}_{DC}$. The frequencies of the dressed transitions with static field can be expressed in terms of these energies as

$$\omega_{MW\text{Dressed}} = \omega_{MW\text{Bare}} + \frac{E_{|F=2,m\rangle} - E_{|F=1,m\rangle}}{\hbar} \tag{7.1}$$

where $\omega_{MW\text{Bare}}$ is the frequency of the bare state transition on which the dressed transitions are based; E_{2m} and E_{1m} are given by Equation 6.3 for the different magnetic sub-levels in the two levels.

7.2.1 Dependence of the clock transitions on the static field

We look at the dependence of the three clock transition frequencies $|F, m\rangle : |1, 0\rangle \rightarrow |2, 0\rangle$, $|F, m\rangle : |1, -1\rangle \rightarrow |2, 1\rangle$ and $|F, m\rangle : |1, 1\rangle \rightarrow |2, -1\rangle$ in particular on the static field with experimental data. The bare transition frequency $\omega_{MW\text{Bare}}$ for these experiments is taken to be 180 kHz. The data is taken as shown in Figure 7.1 and repeated at various static fields. We prepare the atomic state in the $|F, m\rangle : |1, 0\rangle$ level and monitor the dressed MW interaction at different MW detunings with the signals from the $|F = 2\rangle$ levels. This is repeated with the atomic state in a superposition of the $|1, -1\rangle$ and $|1, 1\rangle$ levels to determine the frequencies of the transitions from those levels. The frequencies of the three transitions are plotted with the experimental control magnetic field in Figure 7.2. The static fields at which the two levels couple resonantly with the experimentally determined RF field are also shown in the figure.

The frequencies of the transition $|1,0\rangle \rightarrow |2,0\rangle$ are independent of the magnetic field. We see that these transitions occur at 180.2 kHz, as discussed in Section 7.1, this is due to the offset of the MW source.

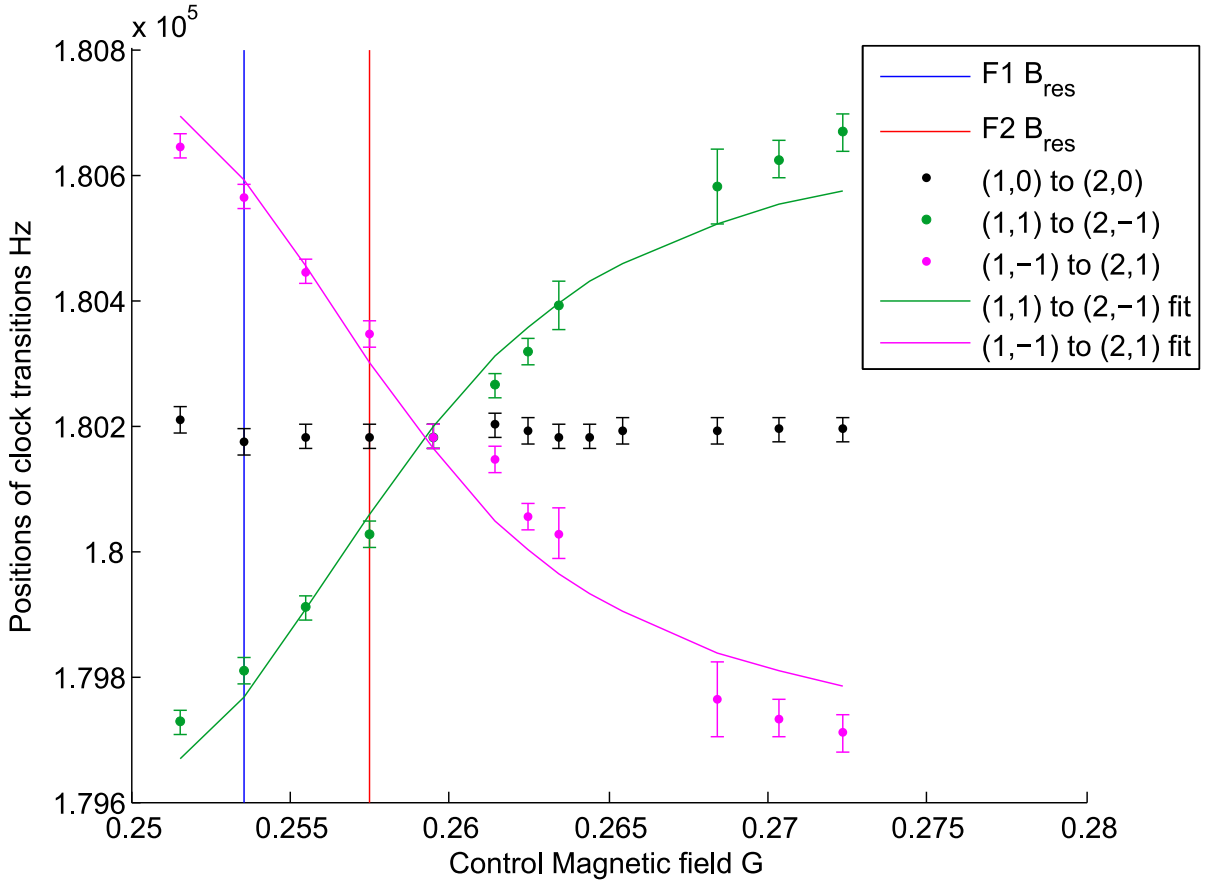


FIGURE 7.2: The figure shows the experimental data and model fits (discussed in the text) showing the dependence of the frequencies of the three clock transitions on static field. The experimental runs are conducted with $\approx 5 \times 10^7$ atoms in each of the $|F = 1\rangle$ sub-levels, driven with MW pulses of varied frequencies and detected in the $|F = 2\rangle$ levels. The positions and widths of the transitions are then extracted to obtain the frequencies and error bars in the figure. The model fits are preliminary; the frequencies calculated from Equation 7.1 for the different static fields in the experiment.

The model fits for the other two transitions are plotted as in Equation 7.1. The static field at which the three transitions occur at the same frequency is expected to be in between the two resonant static fields (F1 B_{res} and F2 B_{res} in the figure), but is in fact larger than both of them in the experiment due to the ellipticity of

the RF field, where $B_+ > B_-$. The model fits use estimated values of $B_\pm$ as free parameters to match this experimentally determined static field. The values of $B_\pm$ from the fits are $B_+ = 11.5$ mG and $B_- = 8.7$ mG which do not both match those obtained from Figure 6.6 ($B_+ = 11.2 \pm 0.4$ mG and $B_- = 10.6 \pm 0.4$ mG); the mismatch is attributed to external field fluctuations over the experimental runs at different static fields. The data set and preliminary fits are included in the thesis as the experimental trend follows that from Equation 7.1.

7.3 Dressed transition strengths

This section discusses the strengths of the three dressed clock transitions $|F,m\rangle : |1,0\rangle \rightarrow |2,0\rangle$, $|F,m\rangle : |1,-1\rangle \rightarrow |2,1\rangle$ and $|F,m\rangle : |1,1\rangle \rightarrow |2,-1\rangle$ and the experimental determination of these strengths compared to the bare clock transition. The frequencies of the Rabi Cycles seen on each of the transitions depend on not only the power of the MW pulses but also the Clebsh-Gordon coefficients of the transitions. Measuring and analyzing the dependence of the Rabi frequencies of each of these transitions with MW pulse power gives an estimate of the coupling coefficients. These coefficients can be expressed in terms of the Clebsh-Gordon coefficient of the bare clock transition $|F,m\rangle : |1,0\rangle \rightarrow |2,0\rangle$ by similar measurement of Rabi frequencies with MW pulse power for this transition.

The Figure 7.3 shows an example of extracting the Rabi frequency of a dressed transition ($|F,m\rangle : |1,0\rangle \rightarrow |2,0\rangle$) at 10 mW MW pulse power.

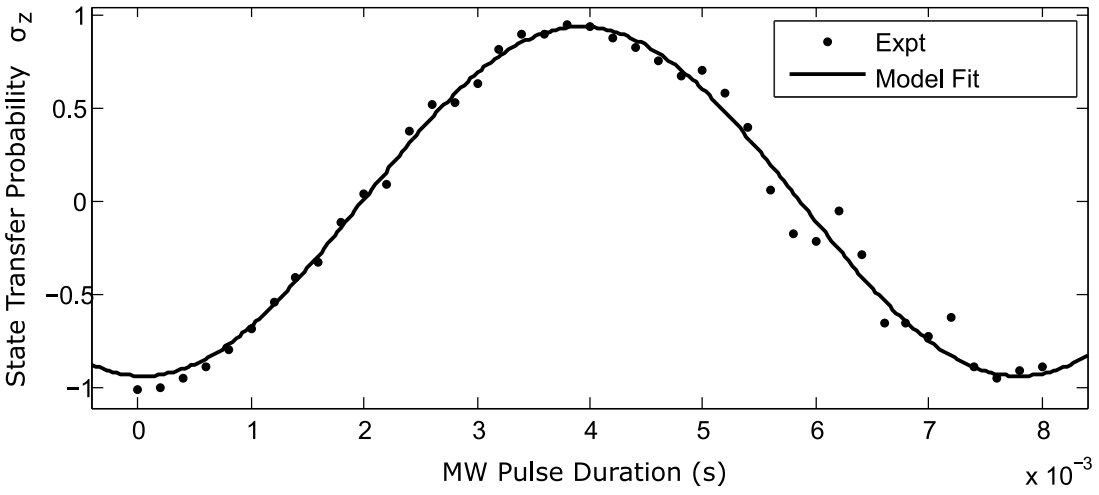


FIGURE 7.3: The figure shows a sample measurement of Rabi cycles on the clock transition $|F,m\rangle : |1,0\rangle \rightarrow |2,0\rangle$ in RF dressed atoms, where the RF field strength is ≈ 10 mG. The state transfer probability is calculated from the populations measured as outlined in Figure 6.4 with $\approx 5 \times 10^7$ atoms and 10 mW MW pulse power. The model fit a*sin(b*x+c) = (0.94 ± 0.04)*sin$\big((810 \pm 79)$*x+$(-1.61 \pm 0.09)\big)$ gives the Rabi frequency b/(2*π) = 128.9 ± 12.6 Hz which will be used to estimate the coupling coefficient as shown in Figure 7.4. The measurements for the Rabi cycles are not repeated considering the amount of data required for analysis in Figure 7.4 and the errors in the Rabi frequency are instead taken from the fitting uncertainty.

The measurements of Rabi cycles as shown in Figure 7.3 are repeated with different MW pulse powers for the three dressed and one bare clock transitions. The frequencies extracted from these measurements are shown in Figure 7.4.

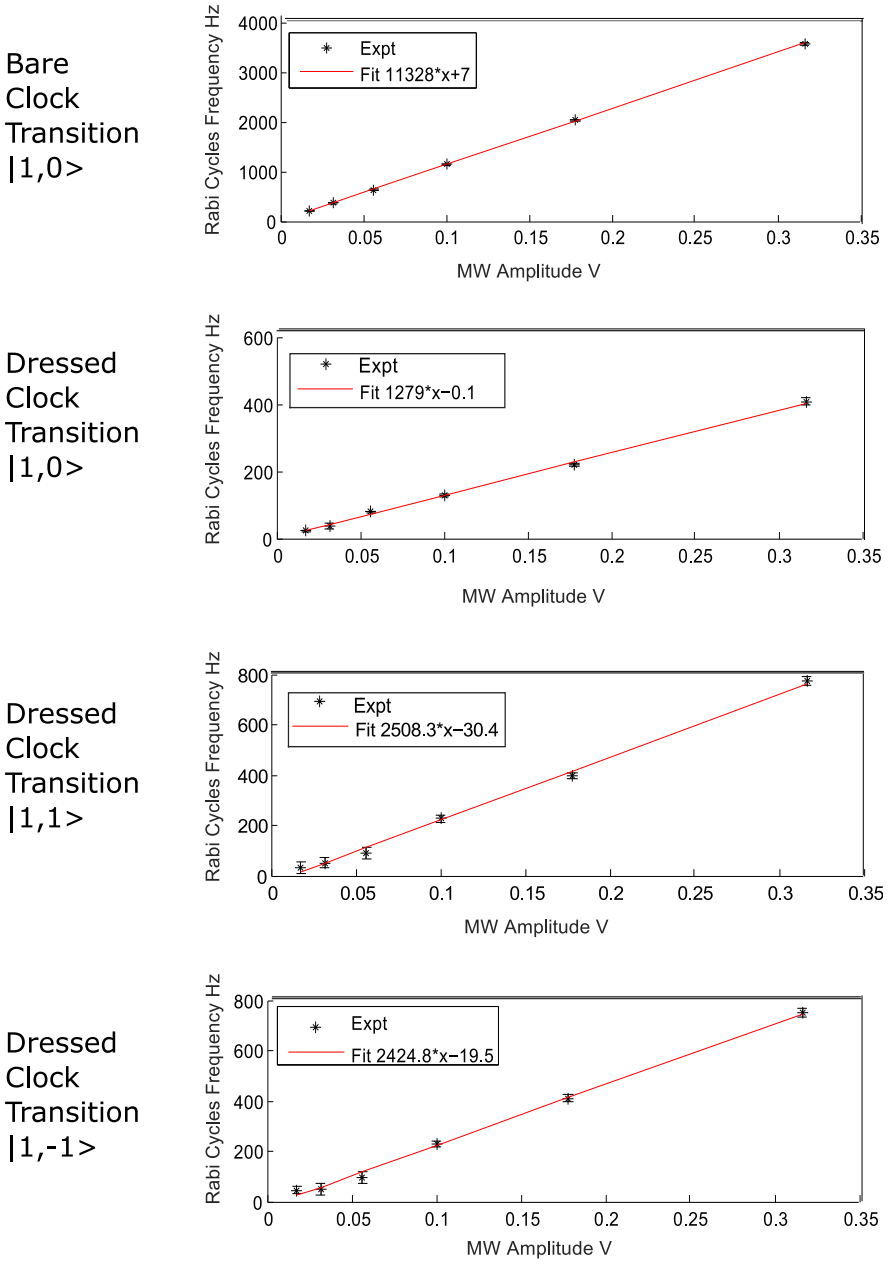


FIGURE 7.4: The figure shows experimental data of Rabi frequencies with MW pulse intensities for the three dressed and one bare clock transitions. Each data point is extracted from a measurement of Rabi cycles on the transitions as shown in Figure 7.3. The transitions' strengths can be estimated from the linear coefficients of the model fits (which are 11328 ± 140 Hz/V for the bare transition $|1,0\rangle \rightarrow |2,0\rangle$; 1279 ± 1 Hz/V for the dressed transition $|1,0\rangle \rightarrow |2,0\rangle$; 2508 ± 1 Hz/V for the dressed transition $|1,1\rangle \rightarrow |2,-1\rangle$ and 2425 ± 1 Hz/V for the dressed transition $|1,-1\rangle \rightarrow |2,1\rangle$.

It is to be noted that though the state preparation for the $|1,0\rangle$ sub-level is efficient, the preparation of the $|1,-1\rangle$ or the $|1,1\rangle$ sub-levels is not clean and thus would result in a superposition of the two. The data shown here for these two sub-levels is not taken with prepared states as given in Section 6.5.1 but with 6×10^7 atoms in a mixed state of the two sub-levels. The two clock transitions are only ≈ 0.5kHz apart and thus the Rabi cycles shown in the data would actually be excitations on the superposition of the sub-levels and not just one of them. As theory expects the two transitions to have the same coupling coefficients, the data is taken into consideration by averaging the two linear coefficients.

The linear coefficients extracted from the analysis in Figure 7.4 give the strengths (or Clebsh-Gordon coefficients) of the dressed transitions in terms of the strength or (Clebsh-Gordon coefficient) of the bare clock transition. The ratio of the strengths of the dressed transition $|1,0\rangle \rightarrow |2,0\rangle$ and the bare clock transition is 0.1129 ± 0.0015; whereas that for the other two dressed transitions with the bare clock transition is 0.2177 ± 0.0028 on average. Private communication from Thomas Fernholz at the University of Nottingham gives the calculated theoretical values for these strengths to be 0.125 and 0.2164 respectively.

Part III

Hollow-Core Fibre based light matter interface

Summary

This part introduces the proposal for the light matter interface based on trapping and loading atoms into a hollow core fibre with an atom chip. Light matter interaction in hollow core fibres has been realized recently in different experiments as discussed in Section 1.1, but the integration of such a fibre into an atom chip experiment demands different modifications to the design of the scheme. These modifications and the preliminary designs and results for this setup are given in Chapter 8.

Chapter 8

Hollow-Core Fibre based light matter interface

8.1 Introduction

Light-matter interfaces designed to measure quantities near the standard quantum limit require the Interaction Strength between light and atoms κ to be of the order of 1. For an ensemble of atoms, κ is given by

$$\kappa = \frac{\sigma}{A}.\frac{\gamma}{\Delta}.\sqrt{N_A.N_P} \tag{8.1}$$

where κ is defined with the light and atom quadratures as $X_L = X_L^{(in)} + \kappa P_A$. Here, σ is the resonant cross section; A is the cross-sectional area of interaction; γ is the lifetime of atomic state; Δ is the optical detuning; N_A and N_P are the numbers of interacting atoms and photons respectively.

Under consideration of spontaneous emission induced atomic decay, the interaction strength achievable in these experiments is limited by the optical density of the atomic ensemble. Using larger number of interacting atoms and photons would increase the optical density but also result in increasing the system's sensitivity to technical noise. The other option to increase the optical density is to reduce the

cross-sectional area of interaction. Using a very small area of interaction like in a Hollow-Core Fibre, typically $10-100\mu m^2$, loaded with cold atoms can result in an interaction strength κ in this regime, as the area occupied by the atoms matches the area of the light sent into the fibre, thereby optimizing the interaction between them.

Figure 8.1 shows the proposed light-matter interface of atoms loaded into a Hollow Core Fibre.

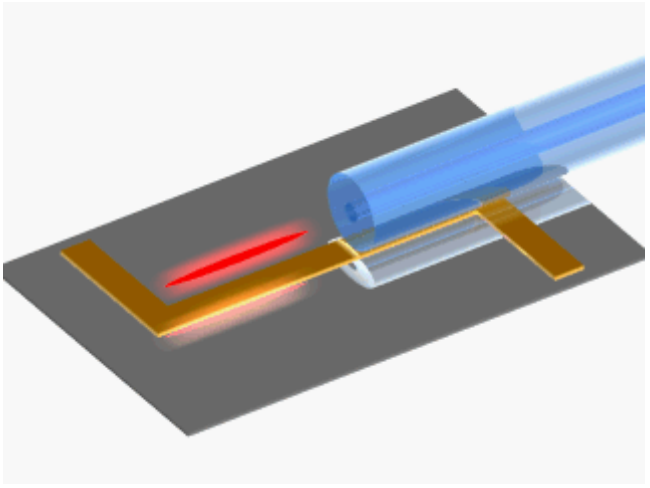


FIGURE 8.1: Figure illustrating the proposed Light-Matter Interface with a Hollow-Core Fibre (blue) on an atom chip (grey), with wires (gold) on the chip creating magnetic fields to trap and load the atoms (red) into the core of the fibre.

The key elements of the proposal, i.e. magnetically trapping and guiding the atoms into a Hollow-Core Fibre with an atom chip are represented. This proposal raises design issues such as the alignment of the fibre with the magnetic field produced by the atom chip and the integration of a Hollow-Core Fibre with an Ultra High-Vacuum chamber; and schematic issues such as the extension of Quantum Memory or Atom Interferometry measurements to trappable atomic levels and the light-atom interaction scheme for detecting the atoms in a fibre. Part II of the thesis introduces RF dressed MW spectroscopy as a method to apply these schemes to trappable levels. Part I introduces a technique to detect the dressed atomic levels, such as those used in Part II, that can be applied to atoms in a fibre. Section 8.2 discusses the design of the set-up to deal with the integration of the fibre in an atom chip experiment.

8.2 Setup Designs

This section outlines the proposed design to integrate a hollow core fibre into an atom chip experiment as shown in Figure 8.2. The atoms from a MOT would be trapped and transported to the loading zone by a Transport PCB. Two fibres would be aligned on the atom chip, one of them being a hollow core fibre, to send and receive the interacting light beams. The atoms would be transferred from the PCB trap to the trap generated by the atom chip, which is then used to guide the atoms into the core of the fibre. Vacuum feedthroughs are required to prevent any pressure leakages near the inputs of the fibres into the UHV chamber.

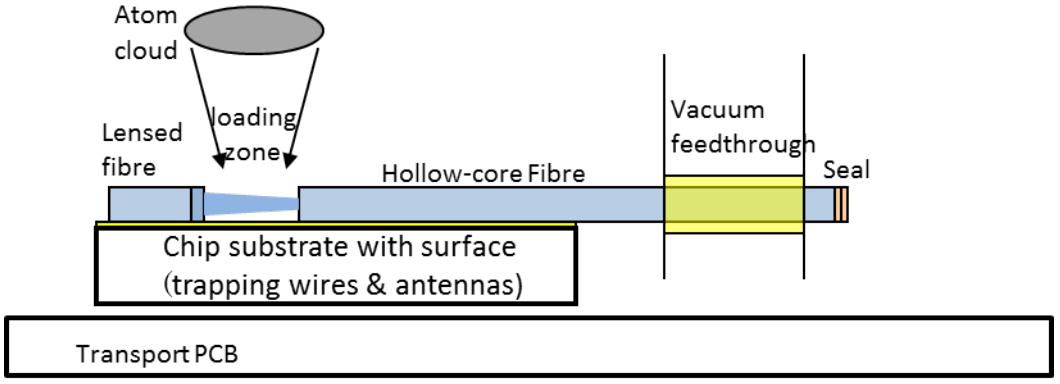


FIGURE 8.2: Figure showing schematic for the integration of the HCF into the atom chip experiment. A Transport PCB will be used to trap atoms from a MOT and transport them to a loading zone close to the atom chip in between the HCF and another fibre. The fibres will be brought into the UHV chamber through vacuum feedthroughs to prevent leakages.

The following sections discuss designs for alignment of the fibres on the chip (Section 8.2.1) and the implementation of the vacuum feedthroughs (Section 8.2.2).

8.2.1 Fibres on Chip

This section discusses the use of guiding structures that can be microfabricated onto the chip [95] for aligning the fibres precisely to the magnetic field axis generated by the atom chip. Polymer structures have been designed to align and hold the two fibres on the chip. The polymer SU-8 50, a negative photoresist generally used for micromachining microsystems [96], has been chosen such that structures

with 90 μm high walls can be fabricated, which is ideal to hold and support fibres that are 125 μm in diameter on the chip. The polymer has already been shown to withstand high temperatures and stress induced in vacuum systems [97].

Structures for testing purposes have been fabricated in a cleanroom, by spinning the photoresist onto a silicon chip followed by exposure to UV light and development of the photoresist. Figure 8.3 shows the typical design of the structures tested to hold the fibres. As SU-8 is a negative photoresist, the design of the structures has to be inverted such that the area forming the structures is exposed to the UV light for curing.

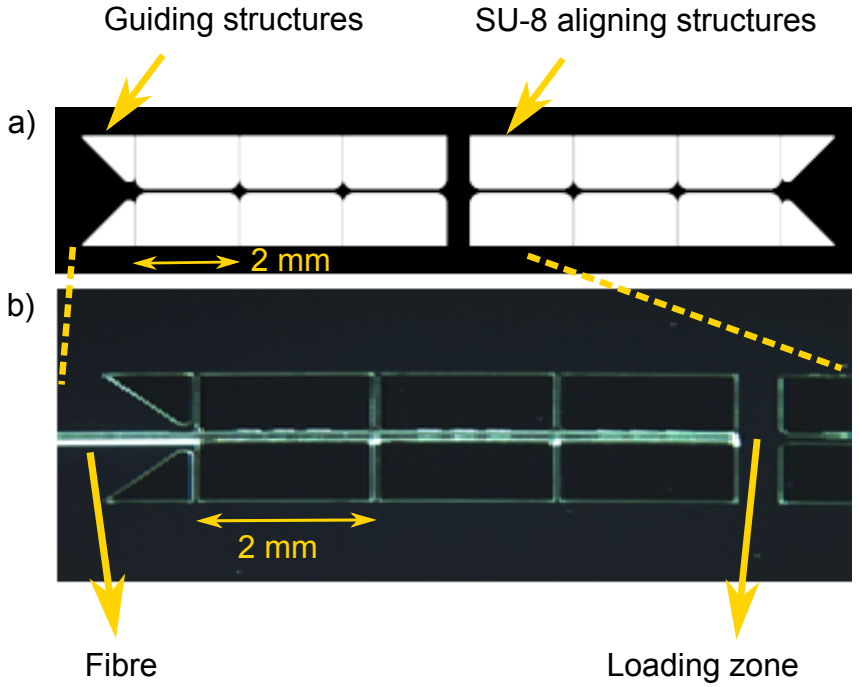


FIGURE 8.3: The figure a) shows the design plot of structures for the UV mask needed to align two fibes with a loading zone at the centre for atoms. The fibre would be inserted through the triangular guides into the gap between the two rows of SU-8 structures. Figure b) shows a sample picture of such structures fabricated on a chip with a fibre inserted through one set of the guiding structures.

The design allows two fibres to be aligned with each other such that their cores are in a line. There is a gap of 500 μm in between the two sets to allow a loading zone for the atoms. Each fibre is held by two walls of dimensions 6 mm x 1 mm. Spaces of 50 μm are left in the structures to allow for heat expansion while baking

out the vacuum chamber. Triangular frames have been added to the outer ends to guide the fibres towards the centre.

The structures can be fabricated precisely up to 1 μm, to ensure that the fibre supported by these structures is in alignment with the magnetic trap; and with the other fibre in the chamber that is used to collect light from the HCF. Figure 8.3 shows how the fibre can be passed in between SU-8 structures such that it is aligned with the second fibre that is similarly held. The UV exposure time for fabricating these structures has been reduced such that their walls are slightly sloping instead of straight, called undercut walls. This holds down the fibres on the chip and minimises the amount of glue used that can outgas in the UHV chamber. Figure 8.4 shows the results of reduced UV light exposure time during the fabrication of the structures to produce the undercut walls required to hold the fibres on the chip.

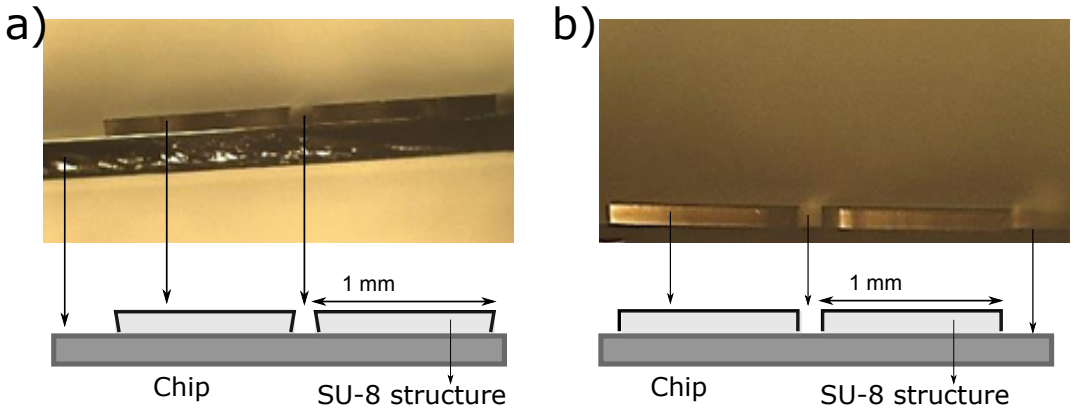


FIGURE 8.4: Modified Structure Edges for holding the fibres: showing side-view pictures of the fabricated structure cross-sections produced with a) 12 s exposure time to UV light compared to b) 17 s exposure time. Illustrations of expected results are shown below for clarity.

The precision attained in the fabrication of the guiding structures exceeds the precision of the diameters of the typically available hollow core fibres maintained by the manufacturing companies. This creates problems of the fibres being a misfit for the structures fabricated or a misalignment of the two fibres resulting in reduced coupling of light between them. To solve this, we modified the design of the structures such that one wall has projections that move with pressure from

the fibre which adjusts the gap between the walls to the fibre diameter exactly. The two modifications are shown in Figure 8.5; one with small enclosures of SU-8 that can be compressed by the fibre and the other with finger-like projections that can be pivoted to adjust for the fibre diameter.

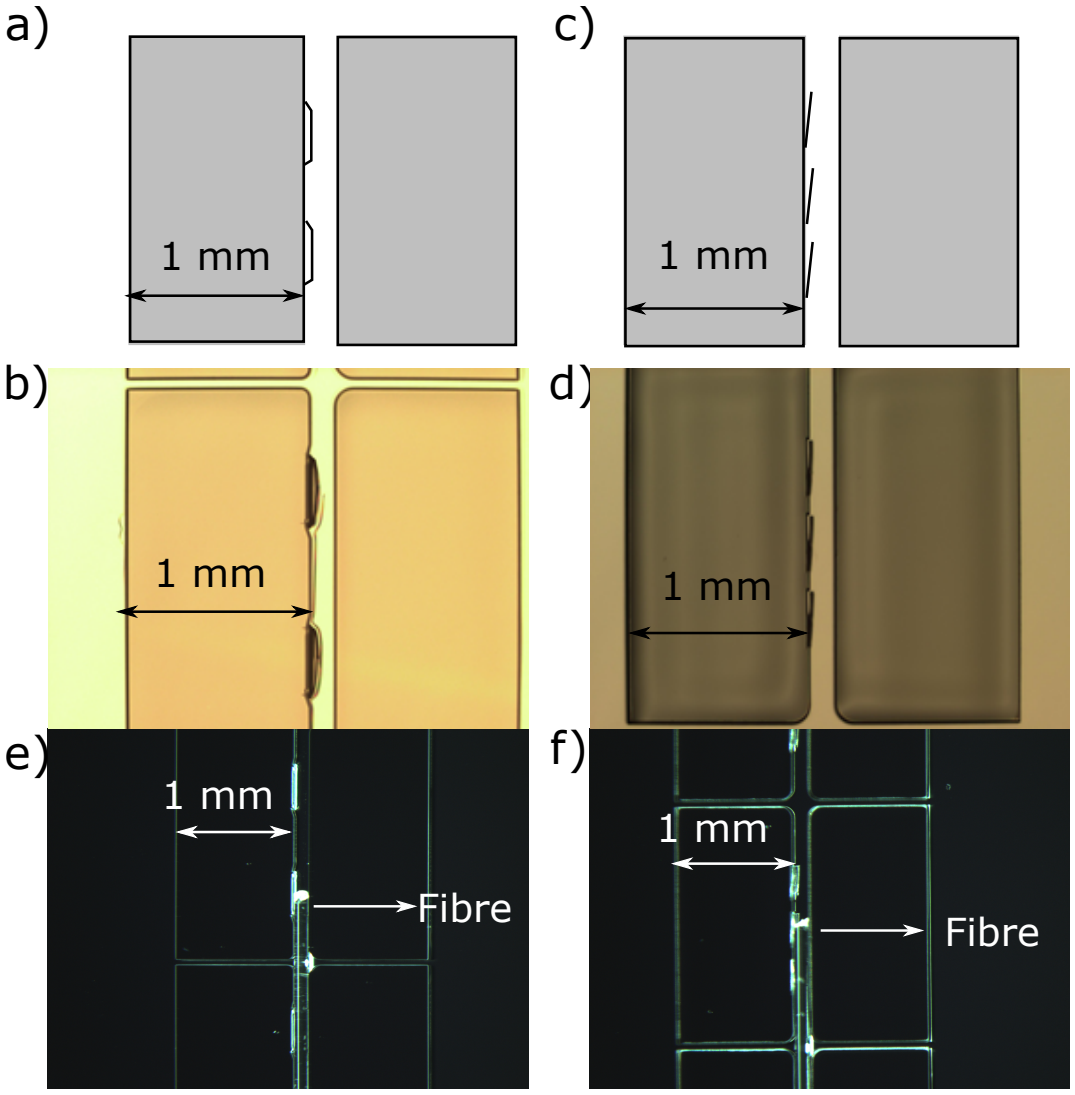


FIGURE 8.5: Modified Support Structures for compatibility to fibre diameters: Figure a) shows the design illustration for SU-8 enclosures with pockets of compressible air to adjust for fibre diameter. Figures b) and c) show top-view pictures of fabricated structures with and without a fibre respectively. Figure c) shows the design illustration for the finger-like projection modifications. Figures d) and e) show top-view pictures of fabricated structures with and without a fibre respectively.

Two normal single-mode fibres have been placed on a chip with these structures for the first tests of coupling light between them as shown in Figure 8.6. A coupling of

80% efficiency has been achieved between these fibres during these tests, using only the fabricated structures for the alignment of the two fibres, i.e. no translation stages or other tools have been used to adjust the coupling efficiency.

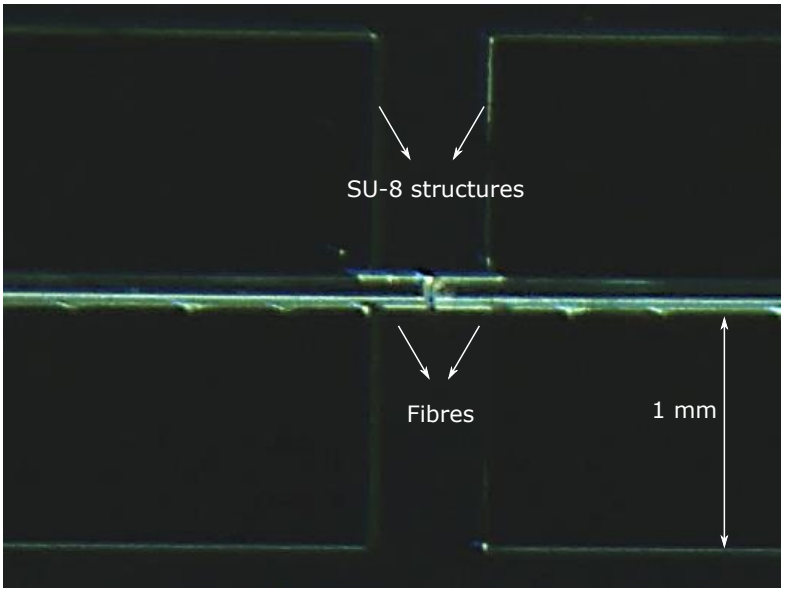


FIGURE 8.6: Coupling of two fibres on a chip: Figure showing the use of the fabricated guiding structures to hold and align two fibres on a chip and test coupling efficiency.

As shown in Figure 8.1, a loading zone of at least a few hundred μm is required between the two fibres to load atoms into the core of the HCF. This means that the light from one fibre should be focused at a distance onto the core of the other fibre. Using a Gradient Index (GRIN) lens in front of a single mode fibre such that the light from the HCF is collected by the lens and focused to the core of the single mode fibre is one option to adapt the scheme to include a loading zone for atoms. However, using a lensed fibre (a fibre designed to collimate or focus light at a distance; that is essentially a single mode fibre with a GRIN lens fused to one end) would address the same issue with reduced optical loss between the GRIN lens and the second fibre. A custom made fibre has been procured (from IDIL Fibre Optiques) to have a focus of 6 μm at a distance of 300 μm. Using these fibres removes the need for gluing GRIN lenses on the chip and increases the efficiency of coupling between the two fibres.

These results prove the feasibility of the scheme using two fibres held on an atom chip, aligned and coupled by the microfabricated guiding structures with good efficiency.

8.2.2 Vacuum Feedthrough

This section discusses the integration of fibres into a UHV chamber and the preliminary tests conducted to facilitate the integration. The possible ways of extracting information from fibres in a UHV chamber is to couple a small length of said fibre in the chamber with one outside through the window of the chamber, or to bring the fibre outside using a vacuum feedthrough and directly interact with the fibre. To optimize the coupling of the fibres in the chamber to light sources or measurement devices outside the chamber, vacuum feedthroughs have been tested to take the fibres into the chamber. The tests of these feedthroughs have been conducted on a separate UHV chamber setup shown in Figure 8.7a), used solely for the purposes of testing vacuum compatibility of various devices.

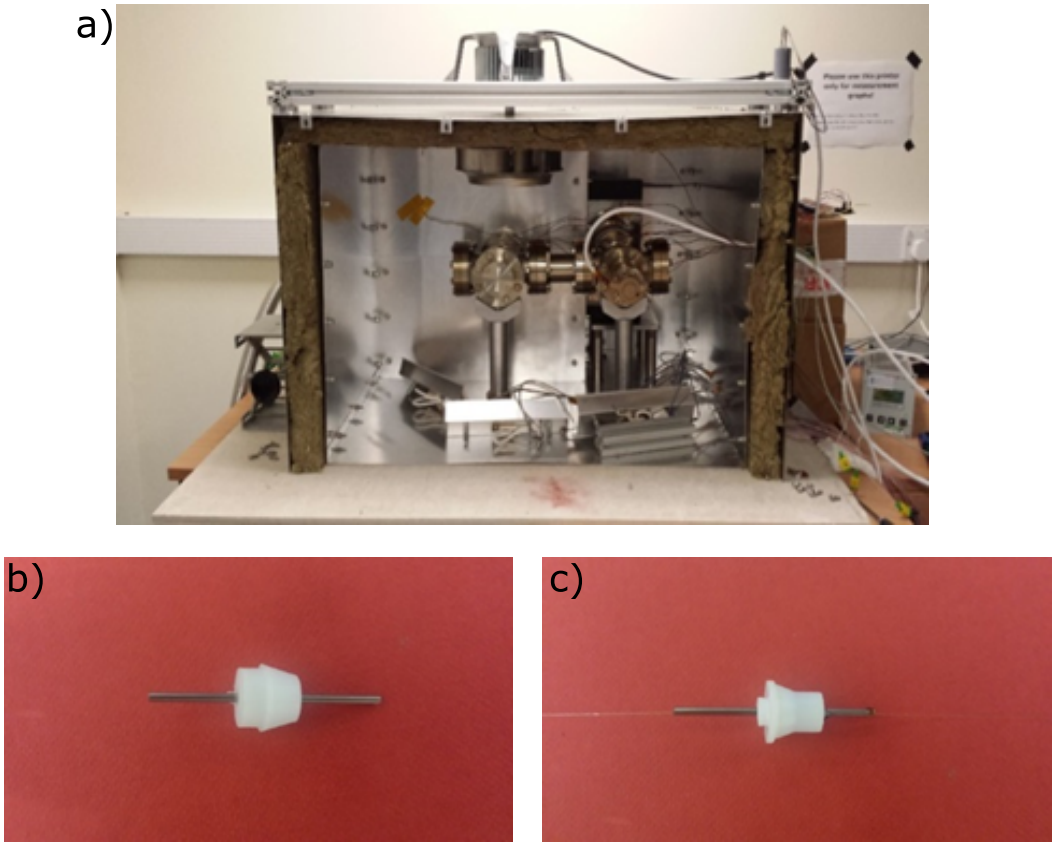


FIGURE 8.7: Figure shows the UHV chamber setup a) for vacuum compatibility tests, the feedthrough design before b) and after c) the test.

The UHV chamber is enclosed in an insulated oven for baking. The first tests have been conducted by taking a fibre through a Teflon ferrule which is then sealed by a Swagelok flange [98], but this design was found to have pressure leaks while cooling down the UHV chamber after baking at 120°C.

The design of the ferrule is modified [99] to accommodate a steel tube with a fibre passing through it. The steel tube is sealed with epoxy glue while taking the fibre through it and then baked at 100 °C for an hour to cure the glue. This tube is then passed through the ferrule and put in the Swagelok flange. This setup is much better for photonic crystal fibres as tightening the Swagelok would apply stress on the steel tube and not on the fibre directly, thus there would be no damage to the crystal structure of the fibre.

Baking at 120 °C achieved a pressure of 7E-11 mBar with this feedthrough for a typical single-mode fibre without any leaks. Figures 8.7b) and c) show the feedthrough with the fibre before and after the test. The distortion is due to the tightening of the Swagelok.

The hollow core of the fibre could act as a pipe permitting leakage of air into the chamber, due to which the pressure of the chamber will not be conducive to ultracold atom expeiments. The core of the fibre outside the chamber would be sealed by a transparent polymer coating with a refractive index 1 to prevent such leakages, yet still allow light to be coupled into the fibre.

These results prove the feasibility of the scheme of integrating Photonic Crystal fibres into a UHV chamber with vacuum feedthroughs.

Chapter 9

Conclusions

This thesis assembles and tests the elements required to perform quantum memory and atomic clock experiments with magnetically trappable levels of alkali atoms in a Hollow-Core Fibre - namely, a proposal to load atoms into an HCF with an atom chip, microwave spectroscopy of Radio-Frequency dressed atoms and dispersive detection of such RF dressed atoms. These elements combine to enable a scheme with longer measuring times due to magnetically trapping atoms compared to experiments on freely falling atoms and quantum noise level measurements with high interaction strength between light and atoms in the proposed light-matter interface as explained in Section 8.1.

The new method to detect atomic levels in RF dressed alkali atoms modulating the atomic response at RF sidebands demonstrated in Part I allows low-noise measurements of atom numbers in two states with an experimentally simple polarimetric setup, enabling quantum noise measurements with lower technological input and passive stabilization compared to for example experiments with optical cavities. The measurement of linear birefringence of the atomic sample with laser beam frequency matches the theoretical $\alpha_F^{(2)}$ terms of off-resonant ^{87}Rb D1 line polarizability, enabling the experimental verification of the figure of merit for such detection as shown in Section 3.5. The ability to perform state to quadrature mapping makes it possible to further reduce technical noise in these measurements.

The technique can be improved by simultaneous probing of the two states with two frequencies generated by a single modulated laser. Combined with state to quadrature mapping, this enables direct measurement of differential state population and potential generation of spin squeezing in the regime of strong light-matter coupling when the atomic ensemble is at sufficient optical density. The method can be used in various internal atom interferometry schemes, any experiments with RF manipulation of atomic traps and may be extended to other dressed state schemes.

To achieve quantum memory or atomic clock schemes with magnetically trapped atoms, the elementary schemes have to be extended to magnetically trappable atomic levels. This extension is proved possible with the demonstration of Radio-Frequency dressed microwave spectroscopy in Part II. The data outlines the extension of the microwave spectroscopy seen in ^{87}Rb atoms from bare states to RF dressed states and discusses the dependence of the transitions on various factors to enable a better understanding of its possible applications.

Finally, a new light-matter interface with a Hollow-Core Fibre in an atom chip experiment is discussed and initial designs tested in Part III to achieve high interaction strength between light and atoms needed for spin squeezing experiments. The fibres on the atom chip have to be aligned precisely with the axis of the magnetic trap for the atoms to enable loading which is achieved with micro-fabication of polymer guiding structures on the chip. The integration of photonic crystal fibres in ultra high vacuum experiments is also demonstrated. This interface establishes the possibility of achieving long measuring times by using magnetic traps for atoms while maintaining the high interaction strength between light and atoms, and thus can be used for a new range of atomic clock, quantum memory, atom interferometry or atomic sensing experiments.

Appendix A

The Off-resonant limit

This section discusses the treatment of the light-atom Interaction Hamiltonian in the off-resonant regime following the calculations done in [89]. In the off-resonant limit, i.e. when the optical laser field is far detuned from the resonance of the atomic transition, the interaction Hamiltonian can be changed to an effective Hamiltonian that depends on the light amplitudes and the ground state spin operators. The coherences $\hat{\sigma}_{F,m;F',m'}$ between the ground and excited states will follow the light field and ground state adiabatically as the population of the excited states is negligible. The coherence $\hat{\sigma}_{F,m-1;F',m}(z,t)$ can be calculated using the Heisenberg equation that governs its time evolution

$$\begin{aligned}\frac{\partial\hat{\sigma}_{F,m-1;F',m}(z,t)}{\partial t} =& \frac{1}{i\hbar}\Big[\hat{\sigma}_{F,m-1;F',m}(z,t), \hat{H}\Big] \\ =& -i(\omega_0 + \Delta_{F'})\hat{\sigma}_{F,m-1;F',m}(z,t) \\ & - ig^{+}_{F,m-1;F',m}\hat{a}_{+}(z,t)\hat{\sigma}_{F,m-1;F,m-1}(z,t) \\ & - ig^{-}_{F,m+1;F',m}\hat{a}_{-}(z,t)\hat{\sigma}_{F,m-1;F,m+1}(z,t)\end{aligned} \tag{A.1}$$

which is derived from the Hamiltonian Equation 2.24 by using the commutation relation and the terms with coherences from the excited state are neglected as the populations in those states are negligible. In the rotating wave approximation, the terms that oscillate with large frequencies (the light amplitudes $\hat{a}_{+}(z,t), \hat{a}_{-}(z,t)$ and the coherence $\hat{\sigma}_{F,m-1;F',m}(z,t)$) have to be transformed to the rotating frame

with the slowly varying operators

$$\hat{\sigma}_{F,m-1;F',m}(z,t) = \tilde{\sigma}_{F,m-1;F',m}(z,t)e^{-i\omega_0 t} \quad \text{and} \quad \hat{a}_{\pm}(z,t) = \tilde{a}_{\pm}(z,t)e^{-i\omega_0 t} \tag{A.2}$$

where a tilde marks the operator as slowly varying. The Heisenberg Equation A.1 can be rewritten with the slow operators as

$$\begin{aligned}\frac{\partial\tilde{\sigma}_{F,m-1;F',m}(z,t)}{\partial t} = &- i\Delta_{F'}\tilde{\sigma}_{F,m-1;F',m}(z,t) \\ &- ig^{+}_{F,m-1;F',m}\tilde{a}_{+}(z,t)\hat{\sigma}_{F,m-1;F,m-1}(z,t) \\ &- ig^{-}_{F,m+1;F',m}\tilde{a}_{-}(z,t)\hat{\sigma}_{F,m-1;F,m+1}(z,t)\end{aligned} \tag{A.3}$$

The term oscillating at frequency $\Delta_{F'}$ is much faster than the typical time scale of the other two terms, thus we can equate the time derivative to zero. The coherence terms $\tilde{\sigma}_{F,m-1;F',m}(z,t)$ and $\tilde{\sigma}_{F,m-1;F',m}(z,t)$ can then be derived [89] as

$$\begin{aligned}\tilde{\sigma}_{F,m-1;F',m}(z,t) = &\frac{-1}{\Delta_{F'}}\Big[g^{+}_{F,m-1;F',m}\tilde{a}_{+}(z,t)\hat{\sigma}_{F,m-1;F,m-1}(z,t) \\ &+ g^{-}_{F,m+1;F',m}\tilde{a}_{-}(z,t)\hat{\sigma}_{F,m-1;F,m+1}(z,t)\Big], \\ \tilde{\sigma}_{F,m-1;F',m}(z,t) = &\frac{-1}{\Delta_{F'}}\Big[g^{-}_{F,m+1;F',m}\tilde{a}_{-}(z,t)\hat{\sigma}_{F,m+1;F,m+1}(z,t) \\ &+ g^{+}_{F,m-1;F',m}\tilde{a}_{+}(z,t)\hat{\sigma}_{F,m+1;F,m-1}(z,t)\Big]\end{aligned} \tag{A.4}$$

The coherence $\tilde{\sigma}_{F,m-1;F',m}(z,t)$ represents the superposition of the atomic state between the ground state $|F,m-1\rangle$ and $|F',m\rangle$. This superposition can be created in two ways, given by the two terms on the right hand side of the equation. The term with the coherence $\hat{\sigma}_{F,m-1;F,m-1}(z,t)$ represents the population in the ground state $|F,m-1\rangle$ driven to the excited state $|F',m\rangle$ by the field $\hat{a}_{+}$ with strength $g^{+}_{F,m-1;F',m}$. The second term with the coherence $\hat{\sigma}_{F,m-1;F,m+1}(z,t)$ represents the atomic state already in a superposition between the ground states $|F,m-1\rangle$ and $|F,m+1\rangle$. The fraction of the atomic population in the state $|F,m+1\rangle$ is driven into $|F',m\rangle$ by the field $\hat{a}_{-}$ with strength $g^{-}_{F,m+1;F',m}$.

Appendix B

Calculations for Interaction Hamiltonian

Here, the calculations of the $C^{\pm}(\Delta, m)$ and the $b(\Delta, m)$ coefficients are shown for the D1 line of ^{87}Rb atoms (as given in [94] by the co-authors) to complete the calculation of the effective interaction Hamiltonian given in Sec.3.1.1.

B.1 Calculating $C^{\pm}(\Delta, m)$

For a given J', the sum over all the excited states for the coupling terms $(g^{\pm}_{Fm,F'm\pm1})^2$ can be written as:

$$C^{\pm}(\Delta, m) = -2\left(\frac{E_0^2}{\hbar}\right)\left(\sum_{F'} \frac{\bar{d}^2_{Fm,F'm\pm1}}{\Delta_{F'}}\right) \times |\langle J||e\mathbf{r}||J'\rangle|^2 \tag{B.1}$$

with

$$\begin{aligned}\bar{d}^2_{Fm,F'm\pm1} =& (2F+1)(2F'+1)(2J+1) \\ &\times \begin{pmatrix} F & 1 & F' \\ m & \pm1 & -(m\pm1) \end{pmatrix}^2 \begin{Bmatrix} F & F' & 1 \\ J' & J & I \end{Bmatrix}^2\end{aligned} \tag{B.2}$$

From the spontaneous decay rate, we can write [100]

$$|\langle J||e\mathbf{r}||J'\rangle|^2 = \frac{3\pi\epsilon_0\hbar c^3}{\omega^3}\left(\frac{2J'+1}{2J+1}\right)\Gamma_{J'}. \tag{B.3}$$

Substituting this in Eq. B.1 and defining polarizability as

$$\alpha_F = 2\left(\frac{2J'+1}{2J+1}\right)\left(\sum_{F'}\frac{\bar{d}^2_{Fm,F'm\pm1}}{\Delta_{F'}}\right) \tag{B.4}$$

we can write

$$\begin{aligned} C^{\pm}(\Delta, m) &= -g\left(\frac{3\epsilon_0\hbar\lambda^3\Gamma_{J'}}{8\pi^2}\right)\alpha_F \\ &= -g\alpha_0\alpha_F \end{aligned} \tag{B.5}$$

where $(c/\omega = \lambda/2\pi)$ with $\alpha_0 = 3\epsilon_0\hbar\lambda^3\Gamma_{J'}/8\pi^2$.

The Clebsch-Gordon coefficients for the relevant transitions here can be calculated as

$$\begin{pmatrix} F & 1 & F+1 \\ m & \pm1 & -(m\pm1) \end{pmatrix} = (-1)^{F+m}\sqrt{\frac{(F\pm m+1)(F\pm m+2)}{(2F+1)(2F+2)(2F+3)}}, \tag{B.6}$$

$$\begin{pmatrix} F & 1 & F \\ m & \pm1 & -(m\pm1) \end{pmatrix} = (-1)^{F+m+1/2(1\pm1)}\sqrt{\frac{(F\mp m)(F\pm m+1)}{F(2F+1)(2F+2)}}, \tag{B.7}$$

$$\begin{pmatrix} F & 1 & F-1 \\ m & \pm1 & -(m\pm1) \end{pmatrix} = (-1)^{F+m}\sqrt{\frac{(F\mp m)(F\mp m-1)}{2F(2F-1)(2F+1)}}. \tag{B.8}$$

In the case of D1 line, there are only two excited states, since $F = I-1/2, I+1/2$ and $F' = I-1/2, I+1/2$.

- For $F = I - 1/2$ the possible excited transitions are $F' = F, F+1$. Therefore, from Equation B.4, the polarizability α_F is given by

$$\begin{aligned}\alpha_F =& 2(2J'+1)\left\{\frac{(2F+1)\chi^F_{F,J'}}{F(F+1)\Delta_F}[F(F+1) \mp m - m^2)]\right.\\ &\left. + \frac{\chi^{F+1}_{F,J'}}{(F+1)\Delta_{F+1}}[(F+1)(F+2) \pm (2F+3)m + m^2]\right\}\end{aligned} \tag{B.9}$$

such that

$$\alpha^{(0)}_F = (2J'+1)\left\{\frac{\chi^F_{F,J'}}{\Delta_F}(2F+1) + \frac{\chi^{F+1}_{F,J'}}{\Delta_{F+1}}(F+2)\right\}, \tag{B.10}$$

$$\alpha^{(\pm1)}_F = (2J'+1)\left\{\pm\frac{(2F+3)\chi^{F+1}_{F,J'}}{(F+1)\Delta_{F+1}} \mp \frac{(2F+1)\chi^F_{F,J'}}{F(F+1)\Delta_F}\right\}, \tag{B.11}$$

and

$$\alpha^{(2)}_F = (2J'+1)\left\{\frac{1}{F+1}\frac{\chi^{F+1}_{F,J'}}{\Delta_{F+1}} - \frac{(2F+1)\chi^F_{F,J'}}{F(F+1)\Delta_F}\right\}. \tag{B.12}$$

For these particular transitions, $\chi^1_{1,1/2} = 1/36$ and $\chi^2_{1,1/2} = 1/12$. Substituting these in Equations B.10-B.12, the values of the polarizability coefficients with different detunings can be calculated as those shown in the following table.

Tensor rank	Polarizability coefficient
$\alpha^{(0)}_1$	$\frac{1}{6\Delta}\left[1 + \frac{3}{1-\Delta_{12}/\Delta}\right]$
$\alpha^{(\pm1)}_1$	$\frac{1}{12\Delta}\left[\pm\frac{5}{1-\Delta_{12}/\Delta} \mp 1\right]$
$\alpha^{(2)}_1$	$\frac{1}{12\Delta}\left[\frac{1}{1-\Delta_{12}/\Delta} - 1\right]$

TABLE B.1: *Polarizability for F=1*

where $\Delta_1 = \Delta$, $\Delta_2 = \Delta - \Delta_{12}$

- For $F = I + 1/2$ the possible excited transitions are $F' = F - 1, F$. Therefore, from Equation B.4, the polarizability α_F is given by

$$\begin{aligned}\alpha_F =&(2J'+1)\left\{\frac{\chi^{F-1}_{F,J'}}{(F)\Delta_{F-1}}[F(F-1)\mp(2F-1)m+m^2]\right.\\ &\left.+\frac{(2F+1)\chi^{F}_{F,J'}}{F(F+1)\Delta_F}[F(F+1)\mp m-m^2)]\right\}\end{aligned} \tag{B.13}$$

such that

$$\alpha^{(0)}_F =(2J'+1)\left\{\frac{\chi^{F-1}_{F,J'}}{\Delta_{F-1}}(F-1)+\frac{\chi^{F}_{F,J'}}{\Delta_F}(2F+1)\right\}, \tag{B.14}$$

$$\alpha^{(\pm1)}_F = \mp\,(2J'+1)\left\{\frac{(2F-1)}{F}\frac{\chi^{F-1}_{F,J'}}{\Delta_{F-1}}+\frac{(2F+1)\chi^{F}_{F,J'}}{F(F+1)\Delta_F}\right\}, \tag{B.15}$$

and

$$\alpha^{(2)}_F =(2J'+1)\left\{\frac{1}{F}\frac{\chi^{F-1}_{F,J'}}{\Delta_{F-1}}-\frac{(2F+1)\chi^{F}_{F,J'}}{F(F+1)\Delta_F}\right\}. \tag{B.16}$$

For these particular transitions, $\chi^1_{2,1/2} = 1/12$ and $\chi^2_{2,1/2} = 1/20$. Substituting these in Equations B.14-B.16, the values of the polarizability coefficients with different detunings can be calculated as those shown in the following table.

Tensor rank	Polarizability coefficient
$\alpha^{(0)}_2$	$\frac{1}{6\Delta}\left[3+\frac{1}{1+\Delta_{12}/\Delta}\right]$
$\alpha^{(\pm1)}_2$	$\mp\frac{1}{4\Delta}\left[1+\frac{1}{1+\Delta_{12}/\Delta}\right]$
$\alpha^{(2)}_2$	$\frac{1}{12\Delta}\left[\frac{1}{1+\Delta_{12}/\Delta}-1\right]$

TABLE B.2: *Polarizability for F=2*

where $\Delta_2 = \Delta$ and $\Delta_1 = \Delta + \Delta_{12}$

B.2 Calculating $b(\Delta, m)$

The coupling terms are given by

$$g^{+}_{Fm-1,F'm} = \frac{E_0}{\hbar}(-1)^{J+I+m-1-F'-F}\sqrt{(2F+1)(2F'+1)(2J+1)} \times \begin{pmatrix} F & 1 & F' \\ m-1 & 1 & -m \end{pmatrix} \begin{Bmatrix} F & F' & 1 \\ J' & J & I \end{Bmatrix} \langle J\|e\mathbf{r}\|J'\rangle \tag{B.17}$$

and

$$g^{-}_{Fm+1,F'm} = \frac{E_0}{\hbar}(-1)^{J+I+m+1-F'-F}\sqrt{(2F+1)(2F'+1)(2J+1)} \times \begin{pmatrix} F & 1 & F' \\ m+1 & -1 & -m \end{pmatrix} \begin{Bmatrix} F & F' & 1 \\ J' & J & I \end{Bmatrix} \langle J\|e\mathbf{r}\|J'\rangle \tag{B.18}$$

Taking their product and using Equation B.3, we can write

$$(g^{+}_{Fm-1,F'm})(g^{-}_{Fm+1,F'm}) = \frac{1}{2\hbar}\left(\frac{\hbar c\lambda^2\Gamma_{J'}}{8\pi A}\right)(3\eta^{F'}_{F,m}) \tag{B.19}$$

where $E_0^2 = \hbar\omega/2\epsilon_0 A$ and

$$\eta^{F'}_{F,m} = 2(2F+1)(2F'+1)(2J'+1) \times \begin{pmatrix} F & 1 & F' \\ m-1 & 1 & -m \end{pmatrix} \begin{pmatrix} F & 1 & F' \\ m+1 & -1 & -m \end{pmatrix} \chi^{F'}_{F,J'} \tag{B.20}$$

From Equation B.19, we can express

$$b(\Delta, m) = -\left(\frac{\hbar c\lambda^2\Gamma_{J'}}{8\pi A}\right)(3\beta_{F,m}) \tag{B.21}$$

where we define $\beta_{F,m} = \sum_{F'} \frac{(\eta^{F'}_{F,m})}{\Delta_{F'}}$.

For the D1 line, there are only two excited states, since $F = I - 1/2, I + 1/2$ and $F' = I - 1/2, I + 1/2$.

For $F = I - 1/2$

- For $F' = F$

$$\eta^{F}_{F,m} = -\frac{(2J'+1)(2F+1)}{F(F+1)}\chi^{F}_{F,1/2}\sqrt{(F+m)(F+m+1)(F-m)(F-m+1)} \tag{B.22}$$

- For $F' = F+1$

$$\eta^{F+1}_{F,m} = \frac{(2J'+1)}{F+1}\chi^{F+1}_{F,1/2}\sqrt{(F+m)(F+m+1)(F-m)(F-m+1)} \tag{B.23}$$

For $F = I + 1/2$

- For $F' = F-1$ is

$$\eta^{F-1}_{F,m} = \frac{(2J'+1)}{F}\chi^{F-1}_{F,1/2}\sqrt{(F+m)(F+m+1)(F-m)(F-m+1)} \tag{B.24}$$

Substituting Equations B.23 and B.24 in Equation B.21 we obtain

$$\begin{aligned} b(\Delta,m) &= -\left(\frac{\hbar c\lambda^2\Gamma_{J'}}{8\pi A}\right)3\left\{2\left(\frac{1}{F}\frac{\chi^{F-1}_{F,1/2}}{\Delta_{F+1}} - \frac{(2F+1)\chi^{F}_{F,1/2}}{F(F+1)\Delta_F}\right)\right\} \\ &\quad \sqrt{(F+m)(F+m+1)(F-m)(F-m+1)} \\ &= -\left(\frac{\hbar c\lambda^2\Gamma_{J'}}{8\pi A}\right)\left(3\alpha^{(2)}_F\sqrt{(F+m)(F+m+1)(F-m)(F-m+1)}\right) \end{aligned} \tag{B.25}$$

Since $\alpha^{(2)}_F$ is the same for $F = 1$ and $F = 2$, according to tables B.1 and B.2, the $b(\Delta,m)$ coefficient is simply

$$b(\Delta,m) = -\left(\frac{\hbar c\lambda^2\Gamma_{1/2}}{8\pi A}\right)\left(3\alpha^{(2)}_F\sqrt{(F+m)(F+1+m)(F-m)(F+1-m)}\right) \tag{B.26}$$

with

$$\alpha^{(2)}_2 = \frac{1}{12\Delta}\left[\frac{1}{1-\Delta_{12}/\Delta} - 1\right] \tag{B.27}$$

Bibliography

[1] Jacob F. Sherson, Hanna Krauter, Rasmus K. Olsson, Brian Julsgaard, Klemens Hammerer, Ignacio Cirac, and Eugene S. Polzik. Quantum teleportation between light and matter. *Nature*, 443(7111):557–560, Oct 2006. ISSN 0028-0836. doi: 10.1038/nature05136. URL http://dx.doi.org/10.1038/nature05136.

[2] M. Bajcsy, S. Hofferberth, T. Peyronel, V. Balic, Q. Liang, A. S. Zibrov, V. Vuletic, and M. D. Lukin. Laser-cooled atoms inside a hollow-core photonic-crystal fiber. *Phys. Rev. A*, 83:063830, Jun 2011. doi: 10.1103/PhysRevA.83.063830. URL https://link.aps.org/doi/10.1103/PhysRevA.83.063830.

[3] Caleb A. Christensen, Sebastian Will, Michele Saba, Gyu-Boong Jo, Yong-Il Shin, Wolfgang Ketterle, and David Pritchard. Trapping of ultracold atoms in a hollow-core photonic crystal fiber. *Phys. Rev. A*, 78:033429, Sep 2008. doi: 10.1103/PhysRevA.78.033429. URL https://link.aps.org/doi/10.1103/PhysRevA.78.033429.

[4] Sprague M. R., Michelberger P. S., Champion T. F. M., England D. G., Nunn J., Jin X.-M., Kolthammer W. S., Abdolvand A., Russell P. St. J., and Walmsley I. A. Broadband single-photon-level memory in a hollow-core photonic crystal fibre. *Nat Photon*, 8(4):287–291, Apr 2014. ISSN 1749-4885. URL http://dx.doi.org/10.1038/nphoton.2014.45. Letter.

[5] William D. Phillips. Nobel lecture: Laser cooling and trapping of neutral atoms. *Rev. Mod. Phys.*, 70:721–741, Jul 1998. doi: 10.1103/RevModPhys.70.721. URL https://link.aps.org/doi/10.1103/RevModPhys.70.721.

[6] Claude N. Cohen-Tannoudji. Nobel lecture: Manipulating atoms with photons. *Rev. Mod. Phys.*, 70:707–719, Jul 1998. doi: 10.1103/RevModPhys.70.707. URL https://link.aps.org/doi/10.1103/RevModPhys.70.707.

[7] Steven Chu. Nobel lecture: The manipulation of neutral particles. *Rev. Mod. Phys.*, 70:685–706, Jul 1998. doi: 10.1103/RevModPhys.70.685. URL https://link.aps.org/doi/10.1103/RevModPhys.70.685.

[8] W. Neuhauser, M. Hohenstatt, P. Toschek, and H. Dehmelt. Optical-sideband cooling of visible atom cloud confined in parabolic well. *Phys. Rev. Lett.*, 41:233–236, Jul 1978. doi: 10.1103/PhysRevLett.41.233. URL https://link.aps.org/doi/10.1103/PhysRevLett.41.233.

[9] D. J. Wineland, R. E. Drullinger, and F. L. Walls. Radiation-pressure cooling of bound resonant absorbers. *Phys. Rev. Lett.*, 40:1639–1642, Jun 1978. doi: 10.1103/PhysRevLett.40.1639. URL https://link.aps.org/doi/10.1103/PhysRevLett.40.1639.

[10] Immanuel Bloch, Jean Dalibard, and Wilhelm Zwerger. Many-body physics with ultracold gases. *Rev. Mod. Phys.*, 80:885–964, Jul 2008. doi: 10.1103/RevModPhys.80.885. URL https://link.aps.org/doi/10.1103/RevModPhys.80.885.

[11] N. Poli, F.-Y. Wang, M. G. Tarallo, A. Alberti, M. Prevedelli, and G. M. Tino. Precision measurement of gravity with cold atoms in an optical lattice and comparison with a classical gravimeter. *Phys. Rev. Lett.*, 106:038501, Jan 2011. doi: 10.1103/PhysRevLett.106.038501. URL https://link.aps.org/doi/10.1103/PhysRevLett.106.038501.

[12] Stephan Falke, Nathan Lemke, Christian Grebing, Burghard Lipphardt, Stefan Weyers, Vladislav Gerginov, Nils Huntemann, Christian Hagemann, Ali Al-Masoudi, Sebastian Häfner, Stefan Vogt, Uwe Sterr, and Christian Lisdat. A strontium lattice clock with its inaccuracy and frequency. *New Journal of Physics*, 16 (7):073023, 2014. URL http://stacks.iop.org/1367-2630/16/i=7/a=073023.

[13] J J García-Ripoll, P Zoller, and J I Cirac. Quantum information processing with cold atoms and trapped ions. *Journal of Physics B: Atomic, Molecular and Optical Physics*, 38(9):S567, 2005. URL http://stacks.iop.org/0953-4075/38/i=9/a=008.

[14] J. I. Cirac, P. Zoller, H. J. Kimble, and H. Mabuchi. Quantum state transfer and entanglement distribution among distant nodes in a quantum network. *Phys. Rev. Lett.*, 78:3221–3224, Apr 1997. doi: 10.1103/PhysRevLett.78.3221. URL https://link.aps.org/doi/10.1103/PhysRevLett.78.3221.

[15] A. Kuzmich and E. S. Polzik. Atomic quantum state teleportation and swapping. *Phys. Rev. Lett.*, 85:5639–5642, Dec 2000. doi: 10.1103/PhysRevLett.85.5639. URL https://link.aps.org/doi/10.1103/PhysRevLett.85.5639.

[16] Xiao-Hui Bao, Andreas Reingruber, Peter Dietrich, Jun Rui, Alexander Duck, Thorsten Strassel, Li Li, Nai-Le Liu, Bo Zhao, and Jian-Wei Pan. Efficient and long-lived quantum memory with cold atoms inside a ring cavity. *Nat Phys*, 8 (7):517–521, Jul 2012. ISSN 1745-2473. doi: 10.1038/nphys2324. URL http://dx.doi.org/10.1038/nphys2324.

[17] Holger P. Specht, Christian Nolleke, Andreas Reiserer, Manuel Uphoff, Eden Figueroa, Stephan Ritter, and Gerhard Rempe. A single-atom quantum memory. *Nature*, 473(7346):190–193, May 2011. ISSN 0028-0836. doi: 10.1038/nature09997. URL http://dx.doi.org/10.1038/nature09997.

[18] Chin-Wen Chou, Julien Laurat, Hui Deng, Kyung Soo Choi, Hugues de Riedmatten, Daniel Felinto, and H. Jeff Kimble. Functional quantum nodes for entanglement distribution over scalable quantum networks. *Science*, 316(5829): 1316–1320, 2007. ISSN 0036-8075. doi: 10.1126/science.1140300. URL http://science.sciencemag.org/content/316/5829/1316.

[19] J. I. Cirac, A. K. Ekert, S. F. Huelga, and C. Macchiavello. Distributed quantum computation over noisy channels. *Phys. Rev. A*, 59:4249–4254, Jun 1999. doi: 10.1103/PhysRevA.59.4249. URL https://link.aps.org/doi/10.1103/PhysRevA.59.4249.

[20] Alessio Serafini, Stefano Mancini, and Sougato Bose. Distributed quantum computation via optical fibers. *Phys. Rev. Lett.*, 96:010503, Jan 2006. doi: 10.1103/PhysRevLett.96.010503. URL https://link.aps.org/doi/10.1103/PhysRevLett.96.010503.

[21] K. Hammerer, K. Mølmer, E. S. Polzik, and J. I. Cirac. Light-matter quantum interface. *Phys. Rev. A*, 70:044304, Oct 2004. doi: 10.1103/PhysRevA.70.044304. URL https://link.aps.org/doi/10.1103/PhysRevA.70.044304.

[22] Lu-Ming Duan, J. I. Cirac, P. Zoller, and E. S. Polzik. Quantum communication between atomic ensembles using coherent light. *Phys. Rev. Lett.*, 85:5643–5646, Dec 2000. doi: 10.1103/PhysRevLett.85.5643. URL https://link.aps.org/doi/10.1103/PhysRevLett.85.5643.

[23] T. Chaneliere, D. N. Matsukevich, S. D. Jenkins, S.-Y. Lan, T. A. B. Kennedy, and A. Kuzmich. Storage and retrieval of single photons transmitted between remote quantum memories. *Nature*, 438(7069):833–836, Dec 2005. ISSN 0028-0836. doi: 10.1038/nature04315. URL http://dx.doi.org/10.1038/nature04315.

[24] M. D. Eisaman, A. Andre, F. Massou, M. Fleischhauer, A. S. Zibrov, and M. D. Lukin. Electromagnetically induced transparency with tunable single-photon pulses. *Nature*, 438(7069):837–841, Dec 2005. ISSN 0028-0836. doi: 10.1038/nature04327. URL http://dx.doi.org/10.1038/nature04327.

[25] Erhan Saglamyurek, Neil Sinclair, Jeongwan Jin, Joshua A. Slater, Daniel Oblak, Felix Bussieres, Mathew George, Raimund Ricken, Wolfgang Sohler, and Wolfgang Tittel. Broadband waveguide quantum memory for entangled photons. *Nature*, 469(7331):512–515, Jan 2011. ISSN 0028-0836. doi: 10.1038/nature09719. URL http://dx.doi.org/10.1038/nature09719.

[26] Christoph Clausen, Imam Usmani, Felix Bussieres, Nicolas Sangouard, Mikael Afzelius, Hugues de Riedmatten, and Nicolas Gisin. Quantum storage of photonic entanglement in a crystal. *Nature*, 469(7331):508–511, Jan 2011. ISSN 0028-0836. doi: 10.1038/nature09662. URL http://dx.doi.org/10.1038/nature09662.

[27] K Jensen, W Wasilewski, H Krauter, T Fernholz, B M Nielsen, J M Petersen, J J Renema, M V Balabas, M Owari, M B Plenio, A Serafini, M M Wolf, C A Muschik, J I Cirac, J H Müller, and E S Polzik. Quantum memory, entanglement and sensing with room temperature atoms. *Journal of Physics: Conference Series*, 264(1): 012022, 2011. URL http://stacks.iop.org/1742-6596/264/i=1/a=012022.

[28] Matthew A. Norcia and James K. Thompson. Strong coupling on a forbidden transition in strontium and nondestructive atom counting. *Phys. Rev. A*, 93: 023804, Feb 2016. doi: 10.1103/PhysRevA.93.023804. URL https://link.aps.org/doi/10.1103/PhysRevA.93.023804.

[29] W. M. Itano, J. C. Bergquist, J. J. Bollinger, J. M. Gilligan, D. J. Heinzen, F. L. Moore, M. G. Raizen, and D. J. Wineland. Quantum projection noise: Population fluctuations in two-level systems. *Phys. Rev. A*, 47:3554–3570, May 1993. doi: 10.1103/PhysRevA.47.3554. URL https://link.aps.org/doi/10.1103/PhysRevA.47.3554.

[30] E Rocco, R N Palmer, T Valenzuela, V Boyer, A Freise, and K Bongs. Fluorescence detection at the atom shot noise limit for atom interferometry. *New Journal of Physics*, 16(9):093046, 2014. URL http://stacks.iop.org/1367-2630/16/i=9/a=093046.

[31] D Heine, W Rohringer, D Fischer, M Wilzbach, T Raub, S Loziczky, XiYuan Liu, S Groth, B Hessmo, and J Schmiedmayer. A single-atom detector integrated on an atom chip: fabrication, characterization and application. *New Journal of Physics*, 12(9):095005, 2010. URL http://stacks.iop.org/1367-2630/12/i=9/a=095005.

[32] G. W. Biedermann, X. Wu, L. Deslauriers, K. Takase, and M. A. Kasevich. Low-noise simultaneous fluorescence detection of two atomic states. *Opt. Lett.*, 34 (3):347–349, Feb 2009. doi: 10.1364/OL.34.000347. URL http://ol.osa.org/abstract.cfm?URI=ol-34-3-347.

[33] D. J. Wineland, J. J. Bollinger, W. M. Itano, and D. J. Heinzen. Squeezed atomic states and projection noise in spectroscopy. *Phys. Rev. A*, 50:67–88, Jul 1994. doi: 10.1103/PhysRevA.50.67. URL https://link.aps.org/doi/10.1103/PhysRevA.50.67.

[34] Masahiro Kitagawa and Masahito Ueda. Squeezed spin states. *Phys. Rev. A*, 47: 5138–5143, Jun 1993. doi: 10.1103/PhysRevA.47.5138. URL https://link.aps.org/doi/10.1103/PhysRevA.47.5138.

[35] K. Schneider, M. Lang, J. Mlynek, and S. Schiller. Generation of strongly squeezed continuous-wave light at 1064 nm. *Opt. Express*, 2(3):59–64, Feb 1998. doi: 10.1364/OE.2.000059. URL http://www.opticsexpress.org/abstract.cfm?URI=oe-2-3-59.

[36] Guang-Ri Jin, Yong-Chun Liu, and Wu-Ming Liu. Spin squeezing in a generalized one-axis twisting model. *New Journal of Physics*, 11(7):073049, 2009. URL http://stacks.iop.org/1367-2630/11/i=7/a=073049.

[37] Mingfeng Wang, Weizhi Qu, Pengxiong Li, Han Bao, Vladan Vuletić, and Yanhong Xiao. Two-axis-twisting spin squeezing by multipass quantum erasure. *Phys. Rev. A*, 96:013823, Jul 2017. doi: 10.1103/PhysRevA.96.013823. URL https://link.aps.org/doi/10.1103/PhysRevA.96.013823.

[38] J. Hald, J. L. Sørensen, C. Schori, and E. S. Polzik. Spin squeezed atoms: A macroscopic entangled ensemble created by light. *Phys. Rev. Lett.*, 83:1319–1322, Aug 1999. doi: 10.1103/PhysRevLett.83.1319. URL https://link.aps.org/doi/10.1103/PhysRevLett.83.1319.

[39] A. Kuzmich, L. Mandel, and N. P. Bigelow. Generation of spin squeezing via continuous quantum nondemolition measurement. *Phys. Rev. Lett.*, 85:1594–1597, Aug 2000. doi: 10.1103/PhysRevLett.85.1594. URL https://link.aps.org/doi/10.1103/PhysRevLett.85.1594.

[40] Anders S. Sørensen and Klaus Mølmer. Entanglement and extreme spin squeezing. *Phys. Rev. Lett.*, 86:4431–4434, May 2001. doi: 10.1103/PhysRevLett.86.4431. URL https://link.aps.org/doi/10.1103/PhysRevLett.86.4431.

[41] Géza Tóth, Christian Knapp, Otfried Gühne, and Hans J. Briegel. Spin squeezing and entanglement. *Phys. Rev. A*, 79:042334, Apr 2009. doi: 10.1103/PhysRevA.79.042334. URL https://link.aps.org/doi/10.1103/PhysRevA.79.042334.

[42] Kevin C. Cox, Graham P. Greve, Joshua M. Weiner, and James K. Thompson. Deterministic squeezed states with collective measurements and feedback. *Phys. Rev. Lett.*, 116:093602, Mar 2016. doi: 10.1103/PhysRevLett.116.093602. URL https://link.aps.org/doi/10.1103/PhysRevLett.116.093602.

[43] Onur Hosten, Nils J. Engelsen, Rajiv Krishnakumar, and Mark A. Kasevich. Measurement noise 100 times lower than the quantum-projection limit using entangled atoms. *Nature*, 529(7587):505–508, Jan 2016. ISSN 0028-0836. URL http://dx.doi.org/10.1038/nature16176. Letter.

[44] Alexander D. Cronin, Jörg Schmiedmayer, and David E. Pritchard. Optics and interferometry with atoms and molecules. *Rev. Mod. Phys.*, 81:1051–1129, Jul 2009. doi: 10.1103/RevModPhys.81.1051. URL https://link.aps.org/doi/10.1103/RevModPhys.81.1051.

[45] S. Altshuler, L. M. Frantz, and R. Braunstein. Reflection of atoms from standing light waves. *Phys. Rev. Lett.*, 17:231–232, Aug 1966. doi: 10.1103/PhysRevLett.17.231. URL https://link.aps.org/doi/10.1103/PhysRevLett.17.231.

[46] S. Altshuler and L. Frantz. Matter wave interferometric apparatus, September 25 1973. URL http://www.google.co.uk/patents/US3761721. US Patent 3,761,721.

[47] David W. Keith, Christopher R. Ekstrom, Quentin A. Turchette, and David E. Pritchard. An interferometer for atoms. *Phys. Rev. Lett.*, 66:2693–2696, May 1991. doi: 10.1103/PhysRevLett.66.2693. URL https://link.aps.org/doi/10.1103/PhysRevLett.66.2693.

[48] Mark Kasevich and Steven Chu. Atomic interferometry using stimulated raman transitions. *Phys. Rev. Lett.*, 67:181–184, Jul 1991. doi: 10.1103/PhysRevLett.67.181. URL https://link.aps.org/doi/10.1103/PhysRevLett.67.181.

[49] O. Carnal and J. Mlynek. Young's double-slit experiment with atoms: A simple atom interferometer. *Phys. Rev. Lett.*, 66:2689–2692, May 1991. doi: 10.1103/PhysRevLett.66.2689. URL https://link.aps.org/doi/10.1103/PhysRevLett.66.2689.

[50] F. Riehle, Th. Kisters, A. Witte, J. Helmcke, and Ch. J. Bordé. Optical ramsey spectroscopy in a rotating frame: Sagnac effect in a matter-wave interferometer. *Phys. Rev. Lett.*, 67:177–180, Jul 1991. doi: 10.1103/PhysRevLett.67.177. URL https://link.aps.org/doi/10.1103/PhysRevLett.67.177.

[51] John F. Clauser. Ultra-high sensitivity accelerometers and gyroscopes using neutral atom matter-wave interferometry. *Physica B*, 151:262–272, Jul 1988. doi: 10.1016/0378-4363(88)90176-3. URL https://doi.org/10.1016/0378-4363(88)90176-3.

[52] Peter J. Martin, Bruce G. Oldaker, Andrew H. Miklich, and David E. Pritchard. Bragg scattering of atoms from a standing light wave. *Phys. Rev. Lett.*, 60:515–518, Feb 1988. doi: 10.1103/PhysRevLett.60.515. URL https://link.aps.org/doi/10.1103/PhysRevLett.60.515.

[53] B. Canuel, F. Leduc, D. Holleville, A. Gauguet, J. Fils, A. Virdis, A. Clairon, N. Dimarcq, Ch. J. Bordé, A. Landragin, and P. Bouyer. Six-axis inertial sensor using cold-atom interferometry. *Phys. Rev. Lett.*, 97:010402, Jul 2006. doi: 10.1103/PhysRevLett.97.010402. URL https://link.aps.org/doi/10.1103/PhysRevLett.97.010402.

[54] J. E. Debs, P. A. Altin, T. H. Barter, D. Döring, G. R. Dennis, G. McDonald, R. P. Anderson, J. D. Close, and N. P. Robins. Cold-atom gravimetry with a bose-einstein condensate. *Phys. Rev. A*, 84:033610, Sep 2011. doi: 10.1103/PhysRevA.84.033610. URL https://link.aps.org/doi/10.1103/PhysRevA.84.033610.

[55] H. Müntinga, H. Ahlers, M. Krutzik, A. Wenzlawski, S. Arnold, D. Becker, K. Bongs, H. Dittus, H. Duncker, N. Gaaloul, C. Gherasim, E. Giese, C. Grzeschik, T. W. Hänsch, O. Hellmig, W. Herr, S. Herrmann, E. Kajari, S. Kleinert, C. Lämmerzahl, W. Lewoczko-Adamczyk, J. Malcolm, N. Meyer, R. Nolte, A. Peters, M. Popp, J. Reichel, A. Roura, J. Rudolph, M. Schiemangk, M. Schneider, S. T. Seidel, K. Sengstock, V. Tamma, T. Valenzuela, A. Vogel, R. Walser, T. Wendrich, P. Windpassinger, W. Zeller, T. van Zoest, W. Ertmer, W. P. Schleich, and E. M. Rasel. Interferometry with bose-einstein condensates in microgravity. *Phys. Rev. Lett.*, 110:093602, Feb 2013. doi: 10.1103/PhysRevLett.110.093602. URL https://link.aps.org/doi/10.1103/PhysRevLett.110.093602.

[56] R. Geiger, V. Ménoret, G. Stern, N. Zahzam, P. Cheinet, B. Battelier, A. Villing, F. Moron, M. Lours, Y. Bidel, A. Bresson, A. Landragin, and P. Bouyer. Detecting inertial effects with airborne matter-wave interferometry. 2:474 EP –, Sep 2011. URL http://dx.doi.org/10.1038/ncomms1479. Article.

[57] Susannah M. Dickerson, Jason M. Hogan, Alex Sugarbaker, David M. S. Johnson, and Mark A. Kasevich. Multiaxis inertial sensing with long-time point source atom interferometry. *Phys. Rev. Lett.*, 111:083001, Aug 2013. doi: 10.1103/PhysRevLett.111.083001. URL https://link.aps.org/doi/10.1103/PhysRevLett.111.083001.

[58] Ch J Bordé. Atomic clocks and inertial sensors. *Metrologia*, 39(5):435, 2002. URL http://stacks.iop.org/0026-1394/39/i=5/a=5.

[59] Steven Peil and Christopher R. Ekstrom. Analysis of atom-interferometer clocks. *Phys. Rev. A*, 89:014101, Jan 2014. doi: 10.1103/PhysRevA.89.014101. URL https://link.aps.org/doi/10.1103/PhysRevA.89.014101.

[60] T. L. Gustavson, P. Bouyer, and M. A. Kasevich. Precision rotation measurements with an atom interferometer gyroscope. *Phys. Rev. Lett.*, 78:2046–2049, Mar 1997. doi: 10.1103/PhysRevLett.78.2046. URL https://link.aps.org/doi/10.1103/PhysRevLett.78.2046.

[61] A. Wicht, J. M. Hensley, E. Sarajlic, and S. Chu. Precision measurement of the fine structure constant based on atom interferometry. *2003 European Quantum Electronics Conference. EQEC 2003 (IEEE Cat No.03TH8665)*, June 2003. doi: 10.1109/EQEC.2003.1314129.

[62] D. S. Weiss, B. C. Young, and S Chu. Precision measurement of h/mcs based on photon recoil using laser-cooled atoms and atomic interferometer. *Applied Physics B*, 59(3):217–256, Sep 1994. doi: 10.1007/BF01081393. URL https://doi.org/10.1007/BF01081393.

[63] μquans precision quantum sensors. URL https://www.muquans.com.

[64] Aosense - sensors for a quantum world. URL http://aosense.com.

[65] Alan L. Migdall, John V. Prodan, William D. Phillips, Thomas H. Bergeman, and Harold J. Metcalf. First observation of magnetically trapped neutral atoms. *Phys. Rev. Lett.*, 54:2596–2599, Jun 1985. doi: 10.1103/PhysRevLett.54.2596. URL https://link.aps.org/doi/10.1103/PhysRevLett.54.2596.

[66] Ron Folman, Peter Krüger, Donatella Cassettari, Björn Hessmo, Thomas Maier, and Jörg Schmiedmayer. Controlling cold atoms using nanofabricated surfaces: Atom chips. *Phys. Rev. Lett.*, 84:4749–4752, May 2000. doi: 10.1103/PhysRevLett.84.4749. URL https://link.aps.org/doi/10.1103/PhysRevLett.84.4749.

[67] J. Schmiedmayer. Quantum wires and quantum dots for neutral atoms. *The European Physical Journal D - Atomic, Molecular, Optical and Plasma Physics*, 4 (1):57–62, Oct 1998. ISSN 1434-6079. doi: 10.1007/s100530050184. URL https://doi.org/10.1007/s100530050184.

[68] P. Krüger, X. Luo, M. W. Klein, K. Brugger, A. Haase, S. Wildermuth, S. Groth, I. Bar-Joseph, R. Folman, and J. Schmiedmayer. Trapping and manipulating neutral atoms with electrostatic fields. *Phys. Rev. Lett.*, 91:233201, Dec 2003. doi: 10.1103/PhysRevLett.91.233201. URL https://link.aps.org/doi/10.1103/PhysRevLett.91.233201.

[69] R J Sewell, J Dingjan, F Baumgärtner, I Llorente-García, S Eriksson, E A Hinds, G Lewis, P Srinivasan, Z Moktadir, C O Gollasch, and M Kraft. Atom chip for bec interferometry. *Journal of Physics B: Atomic, Molecular and Optical Physics*, 43 (5):051003, 2010. URL http://stacks.iop.org/0953-4075/43/i=5/a=051003.

[70] S. J. Kim, H. Yu, S. T. Gang, and J. B. Kim. Matter-wave beam splitter on an atom chip for a portable atom interferometer. *Applied Physics B*, 123(5): 154, Apr 2017. ISSN 1432-0649. doi: 10.1007/s00340-017-6719-6. URL https://doi.org/10.1007/s00340-017-6719-6.

[71] Yves Colombe, Tilo Steinmetz, Guilhem Dubois, Felix Linke, David Hunger, and Jakob Reichel. Strong atom-field coupling for bose-einstein condensates in an optical cavity on a chip. *Nature*, 450(7167):272–276, Nov 2007. ISSN 0028-0836. doi: 10.1038/nature06331. URL http://dx.doi.org/10.1038/nature06331.

[72] Max F. Riedel, Pascal Böhi, Yun Li, Theodor W. Hänsch, Alice Sinatra, and Philipp Treutlein. Atom-chip-based generation of entanglement for quantum metrology. *Nature*, 464(7292):1170–1173, Apr 2010. ISSN 0028-0836. doi: 10.1038/nature08988. URL http://dx.doi.org/10.1038/nature08988.

[73] Barry M Garraway and Hélène Perrin. Recent developments in trapping and manipulation of atoms with adiabatic potentials. *Journal of Physics B: Atomic, Molecular and Optical Physics*, 49(17):172001, 2016. URL http://stacks.iop.org/0953-4075/49/i=17/a=172001.

[74] Michael Albiez, Rudolf Gati, Jonas Fölling, Stefan Hunsmann, Matteo Cristiani, and Markus K. Oberthaler. Direct observation of tunneling and nonlinear self-trapping in a single bosonic josephson junction. *Phys. Rev. Lett.*, 95:010402, Jun 2005. doi: 10.1103/PhysRevLett.95.010402. URL https://link.aps.org/doi/10.1103/PhysRevLett.95.010402.

[75] T. Schumm, S. Hofferberth, L. M. Andersson, S. Wildermuth, S. Groth, I. Bar-Joseph, J. Schmiedmayer, and P. Kruger. Matter-wave interferometry in a double well on an atom chip. *Nat Phys*, 1(1):57–62, Oct 2005. ISSN 1745-2473. doi: 10.1038/nphys125. URL http://dx.doi.org/10.1038/nphys125.

[76] S. Eckel, F. Jendrzejewski, A. Kumar, C. J. Lobb, and G. K. Campbell. Interferometric measurement of the current-phase relationship of a superfluid weak link. *Phys. Rev. X*, 4:031052, Sep 2014. doi: 10.1103/PhysRevX.4.031052. URL https://link.aps.org/doi/10.1103/PhysRevX.4.031052.

[77] Y. Colombe, E. Knyazchyan, O. Morizot, B. Mercier, V. Lorent, and H. Perrin. Ultracold atoms confined in rf-induced two-dimensional trapping potentials. *EPL (Europhysics Letters)*, 67(4):593, 2004. URL http://stacks.iop.org/0295-5075/67/i=4/a=593.

[78] R Kollengode Easwaran, L Longchambon, P-E Pottie, V Lorent, H Perrin, and B M Garraway. Rf spectroscopy in a resonant rf-dressed trap. *Journal of Physics B: Atomic, Molecular and Optical Physics*, 43(6):065302, 2010. URL http://stacks.iop.org/0953-4075/43/i=6/a=065302.

[79] Carlos L. Garrido Alzar, Hélène Perrin, Barry M. Garraway, and Vincent Lorent. Evaporative cooling in a radio-frequency trap. *Phys. Rev. A*, 74:053413, Nov 2006. doi: 10.1103/PhysRevA.74.053413. URL https://link.aps.org/doi/10.1103/PhysRevA.74.053413.

[80] S. Hofferberth, B. Fischer, T. Schumm, J. Schmiedmayer, and I. Lesanovsky. Ultracold atoms in radio-frequency dressed potentials beyond the rotating-wave approximation. *Phys. Rev. A*, 76:013401, Jul 2007. doi: 10.1103/PhysRevA.76.013401. URL https://link.aps.org/doi/10.1103/PhysRevA.76.013401.

[81] Olivier Morizot, Yves Colombe, Vincent Lorent, Hélène Perrin, and Barry M. Garraway. Ring trap for ultracold atoms. *Phys. Rev. A*, 74:023617, Aug 2006. doi: 10.1103/PhysRevA.74.023617. URL https://link.aps.org/doi/10.1103/PhysRevA.74.023617.

[82] Igor Lesanovsky and Wolf von Klitzing. Time-averaged adiabatic potentials: Versatile matter-wave guides and atom traps. *Phys. Rev. Lett.*, 99:083001, Aug 2007. doi: 10.1103/PhysRevLett.99.083001. URL https://link.aps.org/doi/10.1103/PhysRevLett.99.083001.

[83] B. E. Sherlock, M. Gildemeister, E. Owen, E. Nugent, and C. J. Foot. Time-averaged adiabatic ring potential for ultracold atoms. *Phys. Rev. A*, 83:043408, Apr 2011. doi: 10.1103/PhysRevA.83.043408. URL https://link.aps.org/doi/10.1103/PhysRevA.83.043408.

[84] S. J. Kim, H. Yu, S. T. Gang, D. Z. Anderson, and J. B. Kim. Controllable asymmetric double well and ring potential on an atom chip. *Phys. Rev. A*, 93: 033612, Mar 2016. doi: 10.1103/PhysRevA.93.033612. URL https://link.aps.org/doi/10.1103/PhysRevA.93.033612.

[85] W H Heathcote, E Nugent, B T Sheard, and C J Foot. A ring trap for ultracold atoms in an rf-dressed state. *New Journal of Physics*, 10(4):043012, 2008. URL http://stacks.iop.org/1367-2630/10/i=4/a=043012.

[86] P Navez, S Pandey, H Mas, K Poulios, T Fernholz, and W von Klitzing. Matter-wave interferometers using taap rings. *New Journal of Physics*, 18(7):075014, 2016. URL http://stacks.iop.org/1367-2630/18/i=7/a=075014.

[87] B. H. Bransden and C. J. Joachain. *Physics of Atoms and Molecules*. Pearson Education, 2003.

[88] T. Holstein and H. Primakoff. Field dependence of the intrinsic domain magnetization of a ferromagnet. *Phys. Rev.*, 58:1098–1113, Dec 1940. doi: 10.1103/PhysRev.58.1098. URL https://link.aps.org/doi/10.1103/PhysRev.58.1098.

[89] Brian Julsgaard. Phd thesis, entanglement and quantum interactions with macroscopic gas samples. *University of Aarhus*, October 2003.

[90] WILLIAM HAPPER. Optical pumping. *Rev. Mod. Phys.*, 44:169–249, Apr 1972. doi: 10.1103/RevModPhys.44.169. URL https://link.aps.org/doi/10.1103/RevModPhys.44.169.

[91] A. Kuzmich, N. P. Bigelow, and L. Mandel. Atomic quantum non-demolition measurements and squeezing. *EPL (Europhysics Letters)*, 42(5):481, 1998. URL http://stacks.iop.org/0295-5075/42/i=5/a=481.

[92] Y. Takahashi, K. Honda, N. Tanaka, K. Toyoda, K. Ishikawa, and T. Yabuzaki. Quantum nondemolition measurement of spin via the paramagnetic faraday rotation. *Phys. Rev. A*, 60:4974–4979, Dec 1999. doi: 10.1103/PhysRevA.60.4974. URL https://link.aps.org/doi/10.1103/PhysRevA.60.4974.

[93] A. Kuzmich, L. Mandel, J. Janis, Y. E. Young, R. Ejnisman, and N. P. Bigelow. Quantum nondemolition measurements of collective atomic spin. *Phys. Rev. A*, 60:2346–2350, Sep 1999. doi: 10.1103/PhysRevA.60.2346. URL https://link.aps.org/doi/10.1103/PhysRevA.60.2346.

[94] S. Jammi, T. Pyragius, H. M Florez, M. Bason, and T. Fernholz. Dispersive detection of radio-fequency dressed states. *arXiv*. doi: arXiv:1801.07016. URL https://arxiv.org/abs/1801.07016.

[95] Xiyuan Liu, Karl-Heinz Brenner, Marco Wilzbach, Michael Schwarz, Thomas Fernholz, and Jörg Schmiedmayer. Fabrication of alignment structures for a fiber resonator by use of deep-ultraviolet lithography. *Appl. Opt.*, 44(32):6857–6860, Nov 2005. doi: 10.1364/AO.44.006857. URL http://ao.osa.org/abstract.cfm?URI=ao-44-32-6857.

[96] J O'Brien, P J Hughes, M Brunet, B O'Neill, J Alderman, B Lane, A O'Riordan, and C O'Driscoll. Advanced photoresist technologies for microsystems. *Journal of Micromechanics and Microengineering*, 11(4):353, 2001. URL http://stacks.iop.org/0960-1317/11/i=4/a=312.

[97] Hwa Seng Khoo, Kuo-Kang Liu, and Fan-Gang Tseng. Mechanical strength and interfacial failure analysis of cantilevered su-8 microposts. *Journal of Micromechanics and Microengineering*, 13(6):822, 2003. URL http://stacks.iop.org/0960-1317/13/i=6/a=305.

[98] Eric R. I. Abraham and Eric A. Cornell. Teflon feedthrough for coupling optical fibers into ultrahigh vacuum systems. *Journal of Applied Optics*.

[99] B. Buchholz and V. Ebert. Compact, compression-free, displaceable, and resealable vacuum feedthrough with built-in strain relief for sensitive components such as optical fibers. *Review of Scientific Instruments*, 85(5):055109, 2014. doi: 10.1063/1.4872076. URL http://dx.doi.org/10.1063/1.4872076.

[100] D. A. Steck. *Rubidium 87 D Line Data, available online at http://steck.us/alkalidata*, revision 2.1.5, 13 January 2015.